Modal and Impedance Modeling of a Conical Bore for Control Applications

by

Kevin Farinholt

Thesis submitted to the Faculty of the
Virginia Polytechnic Institute and State University
in partial fulfillment of the requirements for the degree of

Master of Science

in

Mechanical Engineering

Donald J. Leo, Chair
Daniel J. Inman
Harry H. Robertshaw

October 2001
Blacksburg, Virginia

Keywords: ppf control, conic sections, noise reduction, payload fairing

Copyright by Kevin M. Farinholt, 2001

Modal and Impedance Modeling of a Conical Bore for Control Applications

Approved by
Advising Committee:

____

____

____

In memory of my mother,

Linda M. Farinholt

Abstract

The research presented in this thesis focuses on the use of feedback control for lowering acoustic levels within launch vehicle payload fairings. Due to the predominance of conical geometries within payload fairings, our work focused on the analytical modeling of conical shrouds using modal and impedance based models. Incorporating an actuating boundary condition within a sealed enclosure, resonant frequencies and mode shapes were developed as functions of geometric and mechanical parameters of the enclosure and the actuator. Using a set of modal approximations, a set of matrix equations have been developed describing the homogeneous form of the wave equation. Extending to impedance techniques, the resonant frequencies of the structure were again calculated, providing analytical validation of each model. Expanding this impedance model to first order form, the acoustic model has been coupled with actuator dynamics yielding a complete model of the system relating pressure to control voltage.

Using this coupled state-space model, control design using Linear Quadratic Regulator and Positive Position Feedback techniques has also been presented. Using the properties of LQR analysis, an analytical study into the degree of coupling between actuator and cavity as a function of actuator resonance has been conducted. Constructing an experimetnal test-bed for model validation and control implementation, a small sealed enclosure was built and outfitted with sensors. Placing a control speaker at the small end of the cone the large opening was sealed with a rigid termination. An internal acoustic source was used to excite the system and pressure measurements were captured using an array of microphones located throughout the conic section. Using the parameters of this experimental test-bed, comparisons were made between LQR and PPF control designs. Using an impulse disturbance to excite the system, LQR simulations predicted reductions of 53.2% below those of the PPF design, while the control voltages corresponding to these reductions were 43.8% higher for

LQR control.

Actual application of these control designs showed that the ability to manually set PPF gains made this design technique much more convenient for actual implementation. Yielding overall attenuation of 38% with control voltages below 200 mV, single-channel low authority control was seen to be an effective solution for low frequency noise reduction. Control was then expanded to a larger geometry representative of Minotaur fairings. Designing strictly from experimental results, overall reductions of 38.5% were observed. Requiring slightly larger control voltages than those of the conical cavity, peak voltages were still found to be less than 306 mV. Extrapolating to higher excitation levels of 140 dB, overall power requirements for 38.5% pressure reductions were estimated to be less than 16 W.

Acknowledgments

First I would like to extend my thanks to my advisor, Dr. Donald J. Leo for his encouragement and advice throughout my graduate studies. Special thanks also go to Dr. Daniel Inman for his insight into controllability and orthogonality issues investigated in this research. I would also like to thank Dr. Harry Robertshaw and Dr. William Saunders for their input and experience related to this research.

I would especially like to thank my parents for their continued support and love throughout my life and education, and it is to my mother that this work is dedicated. I would also like to thank my brother, sisters and all my friends for their understanding, humor and help over the last year.

This research has been supported by the Air Force Research Laboratory at Kirtland Air Force base in Albuquerque, NM and was administered by Syndetix, Inc. under purchase order 00-04-6838. I would also like to thank Dr. Steven Lane of AFRL who has overseen this research.

Contents

List of Tables

List of Figures

Nomenclature

r - spatial coordinate, defined as distance from cone apex

t - time

r_1 - distance from cone apex to the small opening of the conic section

r_2 - distance from cone apex to the large opening of the conic section

$\rho_{tot}(r,t)$ - total density of a fluid particle

ρ_o - ambient density of a fluid particle

$\rho(r,t$ - acoustic or instantaneous density of a fluid particle

$u(r,t)$ - particle velocity

$x(r,t)$ - particle displacement

$\dot{u}$ - particle acceleration

$p_{tot}(r,t)$ - total pressure

p_o - ambient pressure

$p(r,t)$ - acoustic pressure

c_o - speed of sound

$S(r)$ - cross-sectional area at location r

θ - angle of divergence of cone

$\phi(r,t)$ - acoustic potential function

$f(ct \mp r)$ - solution to the plane wave equation

$\varphi(r)$ - spatial component of acoustic potential

$\eta(t)$ - temporal component of acoustic potential

$\beta(t)$ - the integral of $\eta(t)$

ω - frequency $\left[\frac{rad}{s}\right]$

m_a - mass of actuator

k_a - mechanical stiffness of actuator

c_a - mechanical damping of actuator

$F(t)$ - external forcing function

$S(r_1)$ - cross sectional area at r_1, also the actuator area

j - $\sqrt{-1}$ - the imaginary varible

k - wave number

A, B - amplitude coefficients of acoustic potential

M - mass matrix

K - stiffness matrix

f_A - frequency of Ayers *et al.* model in [Hz]

f_{A_o} - fundamental frequency of Ayers *et al.* model

$v_{in}(t)$ - input voltage

$i(t)$ - current

$U(r,t)$ - volume velocity

$e(t)$ - electromotive voltage

z_e - electrical impedance

z_m - mechanical impedance

z_a - acoustic impedance

f - force induced by speaker coil

f_1 - mechanical force of speaker

f_2 - force generated by pressure at r_1

Bl - electromotive constant or flux

R - electrical resistance of actuator

L - electrical inductance of actuator

s - Laplace variable

$P(s)$ - pressure in s-domain

$U(s)$ - volume velocity in s-domain

ω_z - frequency locations of acoustic zeros $\left[\frac{rad}{s}\right]$

ω_p - frequency locations of acoustic poles $\left[\frac{rad}{s}\right]$

q_c - states of the acoustic cavity

q_a - states of the acutator

A_c, B_c, C_c - state space matrices of cavity

A_a, B_a^v, B_a^p, C_a - state space matrices of speaker

F, G, H, J - state space matrices of coupled system

$q(t)$ - state variables

$v(t)$ - input control voltage

Q_1 - state weighting matrix

Q_2 - control effort weighting matrix

$F_{cl}, G_{cl}, H_{cl}, J_{cl}$ - state space matrices of closed loop system

K_{lqr} - LQR feedback gain

L_{est} - estimator gain

$F_{comp}, G_{comp}, H_{comp}, J_{comp}$ - state space matrices of the LQR compensator

ξ - system variable for PPF derivation

η - compensator variable for PPF derivation

ζ_f - compensator damping ratio for PPF filter

ω_f - compensator frequency for PPF filter

g - PPF gain

f_l - Lower frequency limit for mean squared pressure calculations

f_h - High frequency limit for mean squared pressure calculations

Chapter 1

Introduction

1.1 Motivation

Throughout its operational lifetime, the most strenuous loads that a satellite system will be subjected to are experienced during just the first few minutes of launch, Glaese (1999) and Leo (1998). Airflow along the outer walls of payload fairings, coupled with vibrations transmitted from booster rockets induce acoustic resonances within the shroud which houses satellite components. Reaching levels of 120 to 150 dB, Green (2000), damage to instrumentation is a very real concern for designers of satellite systems. Current methods for addressing these concerns primarily consist of the over design of satellite components themselves. Building stronger satellites ensures that they will survive launch, however, at the expense of both functional efficiency as well as cost. With deployment costs estimated at $10,000 to $12,000 per pound according to the Federation of American Scientists FAS (1997), the necessity to over design satellite components carries with it a high monetary cost.

In conjunction with the desire to reduce payload mass, rocket designers have begun the construction of new, lighter weight launch vehicle payload fairings. Moving to stiffened composite materials, up to 61% reductions in fairing weight have been obtained according to the Space Vehicles Directorate of the Air Force Research Laboratory AFRL (1998). While such advancements have reduced launch costs, they have adversely affected the acoustic environment within the fairing. Reductions in weight lower excitation energies, thus increasing both structural vibrations and their coupled affect on acoustic resonances within the shroud. To combat these issues, installation of acoustic blankets have been used along the inner walls of fairings. Dissipating acoustic energy as heat, these methods have proven successful in targeting higher frequency resonances. However, the effectiveness of these materials is directly related to the ratio of material thickness to acoustic wavelength, requiring greater thicknesses for longer wavelengths. Thus, there is a limit at which the required thickness associated with lower frequencies infringes upon the available volume within the fairing. With the typical installation of blankets between 2 and 4 inches thick, passive attenuation is limited to frequencies above 300 to 400 Hz for these materials. While other passive techniques can address low frequency attenuation the volume requirements of both Helmholtz resonators and passive absorbers impede their application. However, the incorporation of active techniques for either tuning absorbers or actively canceling sound offer possible and practical means of reducing noise levels.

To properly implement active control on any system, an understanding of the dynamics within that system should be understood. Considering the various geometries of existing payload fairings, shown in Figure 1.1, one common attribute is the presence of conical and/or cylindrical cavities. Analytical solutions to wave propagation within cylindrical enclosures have been well studied. However, investigations into conical bores have been limited mostly to musical applications. Because of the limited research into these geometries, especially for control applications, the research presented in this thesis includes developments of both modal and impedance models for the purpose of control implementation.

1.2 History of Acoustics

People have theorized that sound propagates as waves for over 2500 years. With its birth in the philosophical community during the times of Pythagoras (550 B.C.) and Aristotle (384-322 B.C.), it was not until the seventeenth century that experimental findings related sound propagation to source vibration. In 1636, Marin Mersenne published his findings in *Harmonie universelle* relating the vibration of two strings, oscillating one octave apart, with the frequency of their respective tones. This combined with work by Galileo Galilei provided the first collection of experimental proof that sound and source frequencies must be the same.

Incidentally, at the same time as the work by Mersenne and Galilei, other researchers were proposing alternate explanations of sound propagation. Using ray theory, Gassendi

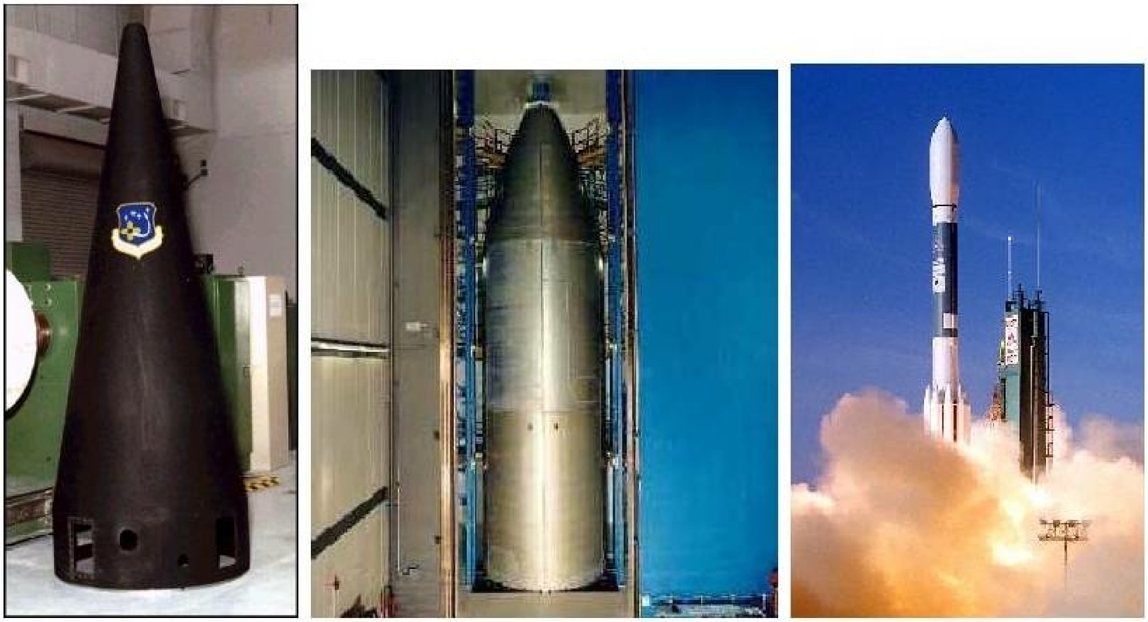

Figure 1.1: Various shroud geometries: a.) grid stiffened USAF launch vehicle payload fairing, b.) Titan IV payload fairing by Lockheed Martin and c.) Delta II payload fairing by Boeing during launch.

proposed that sound was due “to a stream of ‘atoms’ emitted by the sounding body; velocity of sound is speed of atoms; frequency is number emitted per unit time.” [Pierce (1991) p.4]. Arising at the same time as optical sciences, ray theory was later found to be a mathematical approximation of wave theory through work by Reynolds and Rayleigh in the nineteenth century.

However, these findings by Reynolds and Rayleigh were based upon the mathematical development of wave theory, which began in the late seventeenth century with Sir Isaac Newton. Theorizing that acoustics propagate in wave patterns, Figure 1.2 illustrates Newton’s conception of acoustic transmission through an orifice. Continuing with advancements by Euler, Lagrange and d’Alembert, a structured view of acoustic wave theory was developed over the century following Newton’s developments. With the wave equation’s conception for general vibrations and sound, the basis for today’s understanding of acoustics was laid. Building upon the principles of Newton, Euler, Lagrange and d’Alembert the field of acoustics was born, and it is these concepts which are applied in the modeling component of this thesis (Pierce, 1991).

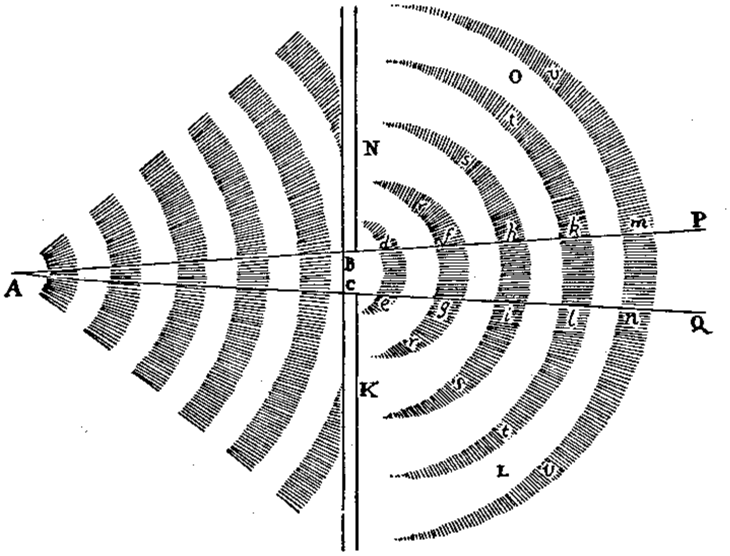

Figure 1.2: Drawing from *Principia* (1686) by Sir Isaac Newton. Illustrates sound propagating through an orifice, which was *"Adapted from Sir Isaac Newton's Principia, 4th ed., 1726, reprinted 1871, by MacLehose, Glasgow, p. 359"*, from Pierce (1991) p. 5

1.3 Literature Review

1.3.1 Studies Associated with Payload Fairings

The investigation into active noise reduction within payload fairings has been a topic of interest for many years, especially for agencies such as the Air Force Research Laboratory and the National Aeronautics and Space Administration (NASA). With external acoustic loads up to 150 dB (Glaese, 1999; Leo, 1998) much work has been conducted for active absorption or cancelation of sound. Himelblau (1992) of the Jet Propulsion Laboratory documents studies on the Titan IV payload fairing to establish the acoustic levels expected during the actual launch of the Cassini spacecraft. In this study, the Titan IV was outfitted with 3 inch thick acoustic blankets along with an array of microphones corresponding to Cassini's expected location during launch. Four separate fairings were launched in this study with a collection of acoustical and flight data for each launch. The outcome of this investigation was the statistical analysis of data describing the interior acoustic environment of the Titan IV during actual launch conditions.

Other studies by engineers at CSA Engineering, Inc. have looked into the vibroacoustic modeling of launch vehicles for acoustic control. Leo (1998) presents work into the structural and acoustic finite element modeling of a payload fairing for the purpose of implementing localized feedback control. In this study, the authors demonstrate that control can be applied using proof-mass and piezoceramic actuators, and that reductions in acoustic levels are possible. Glaese (1999) later presents the simulated and experimental results of a similar study on the STARS payload fairing built by McDonnell Douglas. Using piezo strain sensors and piezo actuators, these authors found that it is possible to increase structural damping within the fairing using a single controller consisting of eight actuators.

In addition to these studies, researchers at Duke University have investigated active control using spatially weighted arrays within acoustic enclosures, (Lane and Clark, 2000). Using a system of multiple collocated sensor-actuator pairs, measurements within the enclosure are taken, processed by the controller using H_2 control laws, and implemented using a spatially weighted array. Experimentally tested in an aluminum aircraft fuselage supplied by Lord Corporation, 6 dB reductions in the global acoustic levels were achieved for a single-mode controller. Expanding to a five-mode controller, the authors found that multiple mode attenuation was also obtainable within the test structure.

Along with the modeling and control of fairings, actuator design has proven to be a result of these studies. Developing a light weight actuator, Green (2000) achieved low frequency performance using piezoceramic actuation. Using cantilever configurations, significant improvements were obtained when comparing noise to weight ratios with those of conventional permanent magnet actuators. However, limitations in stroke and overall power output impede its application presently. Additionally, work done by Henderson *et al.* (2001) investigates decreases in actuator volume while maintaining low frequency performance. Using an partially evacuated enclosure, the authors demonstrate that the depressurization of the speaker enclosure reduces the resonance frequency of the speaker. Thus, the actual volume of this enclosure could be reduced without increasing the operating frequency, provided that a suitable level of evacuation can be applied and maintained within the speaker enclosure.

1.3.2 Previous Acoustic Models

While many of the previous studies related to payload fairing have dealt with understanding the acoustic levels and resonances within the shroud, most modeling approaches have relied strictly on Finite Element models. Providing accurate representations of the enclosed geometry one disadvantage of most Finite element packages is found in the size of the system matrices. In order to effectively apply control design and simulation based upon these models matrix reductions must be implemented, otherwise the analysis becomes computationally intensive. One way to avoid this complexity is the development of analytical models. Provided that the geometries are relatively simple with few discontinuities, analytical solutions can be obtained and implemented for the system. Previous work has been conducted with many basic geometries and it is upon this work that our research has been conducted.

Cylindrical geometries have been studied throughout much of the history of the field of acoustics. Lending themselves to plane wave analysis, analytical models of tubes having open and closed boundary conditions can be obtained with relative ease. As the basic model for many Acoustics courses, the infinite baffle has been used to describe one directional wave propagation in many textbooks, see Rayleigh (1877), Morse (1968), Bies (1996) or Kinsler (1997). Placing a rigid termination at one or both ends of the tube introduces two plane waves, one traveling in the positive direction with another traveling in the negative direction. Again, such solutions are common and relatively easy to reproduce. Introducing a resistive boundary condition complicates analysis slightly as the boundary dynamics must be coupled with the acoustic cavity Kinsler (1997).

Kinsler and Frey (1997) present a detailed approach to such a problem in which they apply a driver at one location with a rigid boundary condition serving as the other termination. Using the mechanical impedance of the driver along with the acoustic impedance of a sealed tube, the authors generate a relationship between the input force of the driver to the pressure at each end of the cylinder. Similarly, Nelson and Elliot (1995) present an open piston in their development of an one-dimensional wave. Expanding upon this model, Nelson and Elliot consider both the presence of a monopole and a dipole source as the actuator, addressing actuators which maintain either pressure or particle velocity on each side of the piston.

While each of these models couple actuator and acoustic dynamics, they address only cylindrical geometries. As a waveguide, cylinders provide a good basepoint for learning analysis techniques, explaining why they are widely used in texts. However, another waveguide which presents similar one-dimensional analysis techniques, but is not employed as readily in textbooks, is the conical bore. With fewer practical applications, conical waveguides have received less attention in their development, especially for control applications. One area which has focused some attention on conical bores is the field of musical instruments. As the basic shape for several woodwind instruments, most modeling is for the purpose of understanding musical tones (Olson, 1967; Rigden, 1977; Taylor, 1992), to properly mimic such instruments electronically.

Due to the geometry of a conical bore, assuming a spherical source at the apex of the cone, or one having a spherical contour associated with its radial distance from the apex, allows for spherically expanding waves to be used in the analysis. Ayers *et al.* (1985) develops the characteristic equation for conical bores having four separate configurations of simple boundary conditions. Solving for open-open, open-closed, closed-open and closed-closed boundaries, the transcendental equations describing resonance frequencies are obtained, along with a visual representation of the standing waves.

1.3.3 Conflicting Developments in Literature on Spherical Waves

One issue in the development of these models is the reliance on physical intuition in the interpretation of results. Such a reliance offers room for incorrect conjectures, leading to some confusion in the interpretation of results. Ayers *et al.* (1985) write their article for the purpose of clarifying issues associated with the unusual behavior of waves near the apex of a conical cavity. With their review of preexisting literature addressing this topic, they found that over two thirds of the references provide incomplete or inaccurate conclusions relative to the behavior of truncated cones at their small end.

Similarly, in a discussion of how sound waves behave in the presence of geometric discontinuities within conical bores, Gilbert (1989) critically disagrees with the findings of Agulló (1992) concerning growing reflections. With a narrowing of the cone, Figure 1.3, the propagating wave form is reflected back onto itself at the discontinuity. Applying conventional analysis techniques, such reflections should ultimately lead to an exponential growth in the sound, as stated by both Gilbert (1989) and Agulló (1992). The discrepancies of Agulló *et al.* are in their explanations of why this exponential growth doesn't occur physically.

While such arguments are present, the correlation of results in this thesis compare model results derived from geometries with terminations normal to wave propagation and experimental results from a geometry similar to the terminated cone of Figure 1.3. The

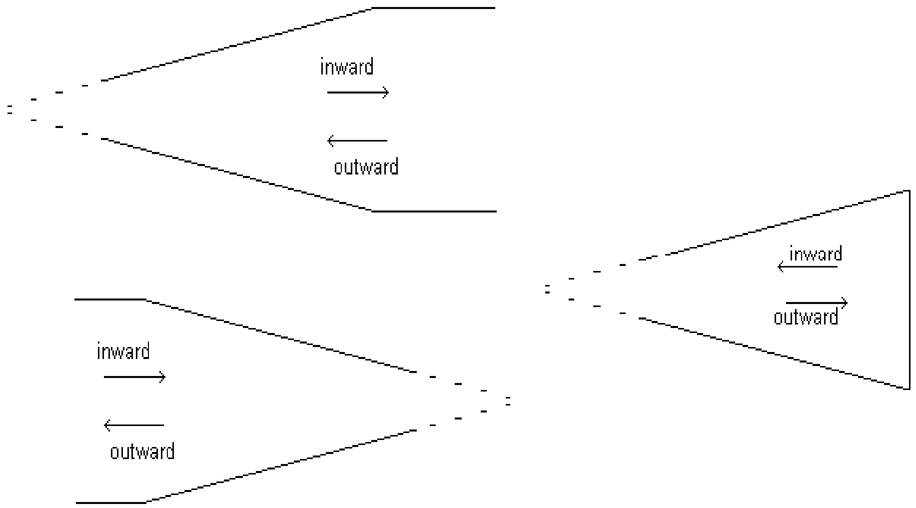

Figure 1.3: Discontinuities with narrowing or terminating geometries.

findings of this study indicate that the discrepancies debated in these articles are practically negligible in the physical system studied in this work.

1.3.4 Control for Active Noise Reduction

Most of today's approaches to active noise reduction rely upon feedforward control techniques. Feeding disturbance signals directly through the system compensator for acoustic control, one major assumption is that the disturbance is known and measurable. While this method of control design has benefits over conventional feedback techniques, Saunders (1993), its reliance on knowing the disturbance makes it impractical for systems in which this disturbance path cannot be modeled. For such systems, feedback control remains the most viable option. While this method must deal with issues concerning reduced robustness and stability relative to feedforward techniques, it possesses the ability to address the transient performance of a system (Green, 2000).

Providing direct information about the system performance, feedback methods use the present output of a dynamic system to alter and control the input signal through the use of a compensator. With a wide range of compensator designs ranging from frequency domain designs to pole placement methods, both classical and modern control techniques have been widely researched and implemented. One type of feedback control design which lends itself to active noise reduction along with other control applications is Linear Quadratic

Regulator design. As a standard control technique in state-space systems, the derivation and application can be found in many textbooks, Franklin (1998) and Friedland (1986). Allowing for the individual weighting of system response (Q) and control effort (R), LQR also gives the designer the opportunity to specify the importance of specific modes relative to one another. Also in such designs, an optimal ratio of $\frac{Q}{R}$ can be obtained through the development of a tradeoff curve between RMS values of the system response and control effort, each as functions of $\frac{Q}{R}$. Within such a curve, there will arise a bend or knee in the convexity of the trade off curve, indicating the optimal ratio of these parameters (Boyd (1997); Leo (1995)).

Alternately, the development of a controller using Positive Position Feedback can be used in active noise control. Providing the ability to target specific modes, this technique gives the designer the ability to increase damping at desired resonance locations. McEver (1999) found that the overestimation of these resonance frequencies, by a factor of $\sqrt{2}$, provides for optimal performance. Also, when targeting multiple modes, the gain specification for each individual PPF filter must be selectively chosen as discussed by DeGuilio (2000). Due to interactions between high frequency gains and low frequency dynamics, the gains must be chosen in a top-down approach. As such, the filter for the highest frequency mode must be designed first, working down through the modes until the lowest frequency filter is designed. Altering from this technique introduces a higher probability of developing an unstable compensator through issues presented by DeGuilio (2000). One important advantage of this technique is that it can be implemented almost directly from experimental data. While many control techniques such as LQR require plant models, all that is really needed for PPF design are the system resonances, where filter damping and gains can be determined iteratively in many applications.

1.4 Thesis Overview

1.4.1 Contribution

The purpose of the research presented in this thesis is the attenuation of noise levels within launch vehicle payload fairings through the use of feedback control. Focusing on geometries similar to those found on typical sounding rockets, we have developed analytical models which predict resonance and modal properties of the acoustic environment. Having developed two separate models using modal approximation and impedance based techniques, a full characterization of the longitudinal waves within a conical bore having actuating and rigid boundary conditions has been accomplished. Allowing full variation in the mass, damping and stiffness properties of a control actuator, first-order representation of the conical fairing have been generated. Analytical and experimental comparison was used to validate the model for multiple actuator parameters. Upon this model, investigations of Linear Quadratic Regulator and Positive Position Feedback techniques have been presented and discussed. Due to very small variations in open-loop and closed-loop pole locations for the LQR compensated system, PPF design was chosen and applied for simulation and experimental application. Implementing these controllers has shown that significant reductions in sound levels can be obtained using low authority control based on PPF design techniques. With RMS pressure reductions of 38.2% within the test-stand, power requirements were held to levels of 0.92 mW. Our study also worked to expand the control design to larger volumes with varying geometries. Selecting a fairing geometry of the Minotaur class, a half-scale model was constructed and PPF control was designed and applied. From this portion of our study the abilities of low authority control was again demonstrated as 38.5% reductions in RMS pressure were achieved. In this application power requirements were measured to be below 1.52 mW. Obtained for systems with disturbance levels of 100 dB (C-weight), the results of our study were extended to sound levels of 140 dB, correlating to those measured during actual launch conditions. Estimating power levels of 15.2 W for the half-scale model, the anticipated power requirements necessary to apply such control on a full scale fairing are on the order of 65 W, considering volumetric increases. In its entirety, the research that we have conducted has addressed the modeling and control of the fairings with conical geometries, finding that control using single actuator-sensor pairing is both possible and effective in lowering noise levels within a sealed environment.

1.4.2 Approach

Modal modeling of the conical bore is presented in Chapter 2 with a further discussion of the asymmetry properties continued in Appendix A. Chapter 3 discusses the impedance model development and its coupling with actuator dynamics. Development of the state-space model used for simulation is also presented in Chapter 3, with a discussion of the actual controller designs found in Chapter 4. Experimental results for accuracy of each model is presented in Chapter 5, along with the results from actual implementation of both LQR and PPF control on the conical fairing, and of PPF control on the full fairing shroud. Chapter 6 wraps up with the conclusions of this research along with recommendations for future work. Mathematical codes for model and compensator designs are found in the Appendices.

Chapter 2

Modal Model of a Conical Bore

In most noise control applications the conventional method for approaching a problem begins with an impedance model of the system. However, for this research the first model development uses a modal approximation of a sealed conical bore having one rigid and one actuating boundary condition. Using conservation laws for mass and momentum a modal approximation of the system can be developed and an equation of motion extracted directly. Without instituting the steady state assumption both velocity and pressure variables can be maintained, allowing for analysis of the transient performance of the system. Developed directly from basic acoustic equations, the matrix form of an equation of motion can be developed that couples the electrical dynamics of the actuator with the acoustic system providing a full model of the system

2.1 Conservation of Mass and Momentum

Beginning with the driver system illustrated in Figure 2.1 two conservation laws must be upheld across the control volume, conservation of mass and of momentum. Considering the elemental volume of Figure 2.1 any influx of mass into the volume must equal the accumulating mass within the system plus the outflux of mass from the control volume. Enforcing such a condition ensures that all of the mass is accounted for within the system, satisfying the conservation of mass assumption. Similarly, any net force applied to the fluid element within this volume must correspond to a resultant acceleration of fluid, such that momentum is conserved. Combining the resulting equations of these two conservation laws the one-dimensional wave equation can be developed.

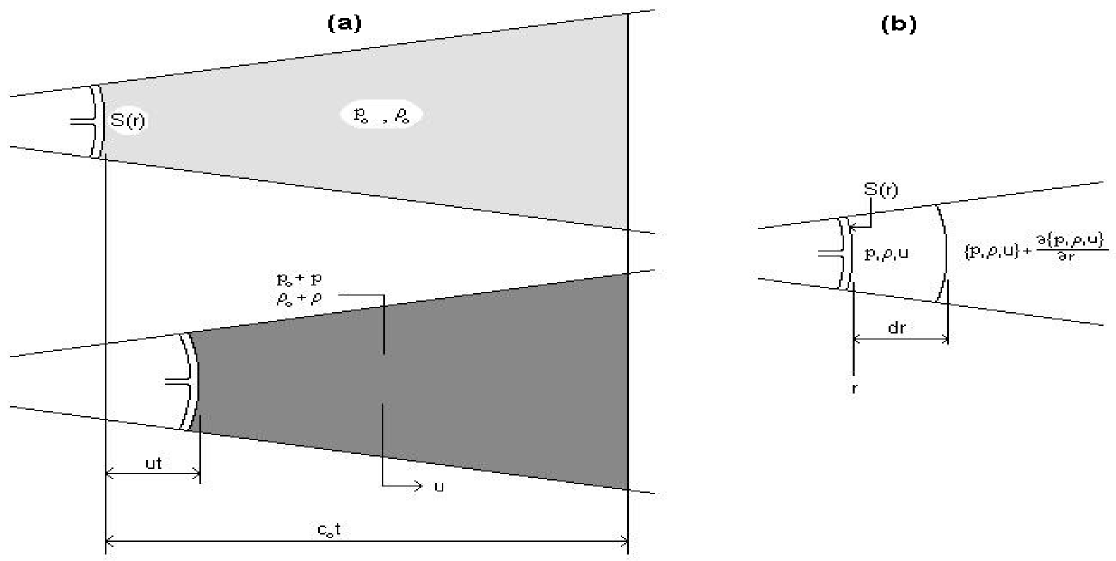

Figure 2.1: Compression of a fluid within a conical bore. a.) Compression from a driver operating with velocity u over time t. b.) Control volume of fluid, p, ρ, u **at a location,** r**, and** p, ρ, u **at displaced location** $r + dr$**.**

2.1.1 Conservation of Mass

In Figure 2.1b the inflow of mass can be represented as

$$\rho_{tot}(r,t)u(r,t)S(r) - \left[\rho_{tot}(r,t)u(r,t)S(r) + \frac{\partial\left[\rho_{tot}(r,t)u(r,t)S(r)\right]}{\partial r}dr\right] = -\frac{\partial\left[\rho_{tot}(r,t)u(r,t)S(r)\right]}{\partial r}dr, \tag{2.1}$$

In order to enforce conservation of mass, the total inflow must equal the accumulating mass within the system. Defining this accumulation as $\frac{\partial \rho_{tot}}{\partial t}S(r)dr$ conservation of mass becomes,

$$\frac{\partial\left[\rho_{tot}u(r,t)S(r)\right]}{\partial r} + \frac{\partial\left[\rho_{tot}(r,t)S(r)\right]}{\partial t} = 0. \tag{2.2}$$

Considering the two components of equation 2.2 the left most term can be further simplified by reducing $\rho_{tot}(r,t)$ to its individual components. Comparing the variations in fluid density associated with the acoustic wave with the density of ambient air it is seen that ρ is much smaller than ρ_o. Taking this into account, $\rho u(r,t)$ can be neglected in the spatial derivative of equation 2.2. Also considering that the ambient pressure is constant in both location and time, ρ_o can also be removed from the spatial derivative. Applying a similar expansion of the right most term in equation 2.2 can be used to further simplify this component of the expression. In this temporal derivative, $\rho_{tot}(r,t)$ can be separated into both ambient and acoustic terms as before. Again considering that ρ_o is constant both spatially and temporally and cross-sectional area is only a function of location, $\frac{\partial \rho_o S(r)}{\partial t}$ must go to zero. This reduces the linearized conservation of mass to,

$$\frac{\partial\left[\rho(r,t)S(r)\right]}{\partial t}+\rho_o\frac{\partial\left[u(r,t)S(r)\right]}{\partial r}=0. \tag{2.3}$$

2.1.2 Conservation of Momentum

Next, consider that momentum must be conserved within this system. Using the more common form of Newton's second law $\sum_{i=1}^{N}F_i=ma$, a force balance can be performed on the system, relating applied forces to the resultant acceleration of the fluid element. Defining $p_{tot}(r,t)$ as the sum of the ambient pressure p_o and the acoustic pressure p, the net force on the fluid in Figure 2.1b is,

$$p_{tot}(r,t)S(r)-\left[p_{tot}(r,t)+\frac{\partial p_{tot}(r,t)}{\partial r}dr\right]S(r)=-S(r)\frac{\partial p_{tot}(r,t)}{\partial r}dr. \tag{2.4}$$

Following Newton's second law, this net force must equal the mass of the fluid element times its acceleration. According to Nelson and Elliot (1995), this acceleration takes the form $\frac{\partial u}{\partial t}=u\frac{\partial u}{\partial r}+\frac{\partial u}{\partial t}$. According to the authors, this form accounts for the fact that velocity is a spatial function as well as a temporal function. However, they follow the argument of Kinsler (1997) that this spatial term $u\frac{\partial u}{\partial r}$ is much smaller than $\frac{\partial u}{\partial t}$, and is acceptably ignored. Thus, the mass times acceleration component of the force balance can be approximated as $\rho_o S(r)dr\frac{\partial u}{\partial t}$, resulting in a linearized conservation of momentum equation,

$$\rho_o S(r)\frac{\partial u(r,t)}{\partial t}+S(r)\frac{\partial p_{tot}(r,t)}{\partial r}=0. \tag{2.5}$$

As with the acoustic density, ambient pressure is constant, such that the spatial and temporal derivatives of p_o are zero, simplifying equation 2.5 to

$$\rho_o S(r)\frac{\partial u(r,t)}{\partial t}+S(r)\frac{\partial p(r,t)}{\partial r}=0. \tag{2.6}$$

2.1.3 The Wave Equation

Taking the time derivative of equation 2.3 and the spatial derivative of equation 2.6, it is possible to equate the two expressions, resulting in the following equation

$$\frac{\partial^2\left[\rho(r,t)S(r)\right]}{\partial t^2}+\rho_o\frac{\partial^2\left[u(r,t)S(r)\right]}{\partial r\partial t}=\rho_o\frac{\partial^2\left[u(r,t)S(r)\right]}{\partial r\partial t}+\frac{\partial}{\partial r}\left[S(r)\frac{\partial p(r,t)}{\partial r}\right]. \tag{2.7}$$

Assuming that this compression is an adiabatic process, pressure and density are linearly related by $p = c_o^2 \rho$. Making this substitution, and eliminating the repeated terms in equation 2.7, the wave equation simplifies to

$$\frac{\partial}{\partial r}\left[S(r)\frac{\partial p(r,t)}{\partial r}\right] - \frac{1}{c_o^2}S(r)\frac{\partial^2 p(r,t)}{\partial t^2} = 0. \tag{2.8}$$

Dividing through by $S(r)$, the wave equation for spherically expanding waves is obtained,

$$\frac{1}{S(r)}\frac{\partial}{\partial r}\left[S(r)\frac{\partial p(r,t)}{\partial r}\right] - \frac{1}{c_o^2}\frac{\partial^2 p(r,t)}{\partial t^2} = 0. \tag{2.9}$$

2.2 Defining the Wave Equation using Acoustic Potential

In this form, the wave equation is primarily a function of pressure. While this expression comes directly from the conservation laws of mass and momentum, many acoustics textbooks write this expression in terms of an acoustic potential instead of pressure (Morse, 1968; Bies, 1996). By defining a potential function, $\phi(r,t)$, as

$$p(r,t) = \rho\frac{\partial \phi(r,t)}{\partial t}, \tag{2.10}$$

the spatial component of both pressure and acoustic potential are the same. Rearranging the momentum conservation equation, 2.6, Euler's relationship develops, relating pressure to velocity as follows

$$\rho_o\frac{\partial u(r,t)}{\partial t} = -\frac{\partial p(r,t)}{\partial r}. \tag{2.11}$$

Substituting the pressure to potential relationship of equation 2.10 into Euler's equation, it is seen that acoustic potential is related to particle velocity as

$$u(r,t) = -\frac{\partial \phi(r,t)}{\partial r} = -\nabla\phi(r,t). \tag{2.12}$$

Defining an acoustic potential such that both equations 2.10 and 2.12 are satisfied, the wave equation can be rewritten in the following form,

$$\frac{1}{S(r)}\frac{\partial}{\partial r}\left[S(r)\frac{\partial \phi(r,t)}{\partial r}\right] = \left(\frac{1}{c_o^2}\right)\frac{\partial^2 \phi(r,t)}{\partial t^2}. \tag{2.13}$$

In terms of acoustic potential, it is desirable to find a set of solutions which satisfy the partial differential equation of equation 2.13. However, in its present form, a solution is not easily seen due to the presence of the spatially varying area $S(r)$. In order to simplify

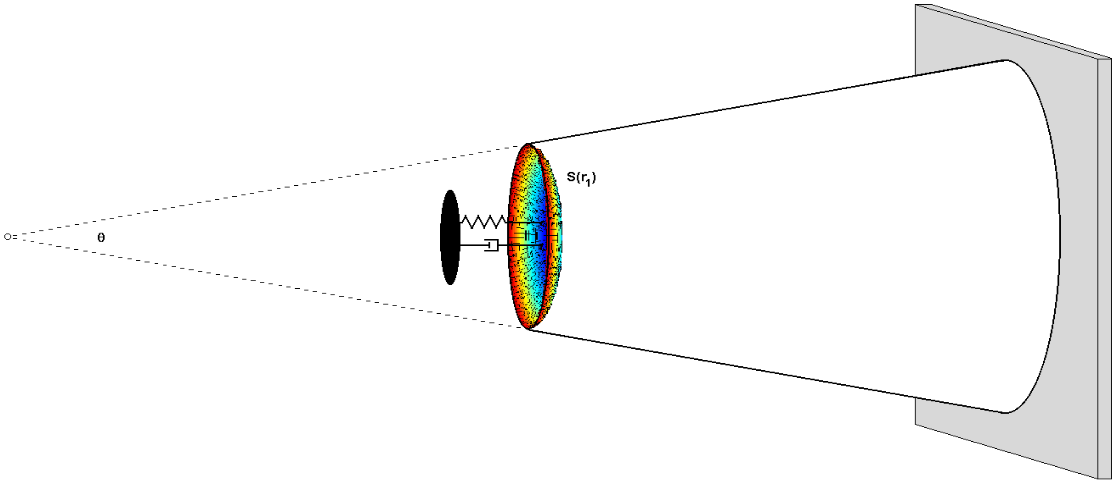

Figure 2.2: The spherical contour of the actuator face.

the wave equation, it is assumed that the wave propagates with a spherical contour related to its distance from the cone apex, as shown in Figure 2.2. As such, this area can be defined as

$$S(r) = (2\pi - 2\pi cos(\theta))\, r^2 \tag{2.14}$$

where θ is the angle of the cone. Substituting this expression into equation 2.13, the component $(2\pi - 2\pi cos(\theta))$ is constant with respect to r and can be extracted, canceling with the same component in the $\frac{1}{S(r)}$ term, simplifying the wave equation to

$$\frac{1}{r^2}\frac{\partial}{\partial r}\left[r^2\frac{\partial\phi}{\partial r}\right] = \frac{1}{c^2}\frac{\partial^2\phi}{\partial t^2}. \tag{2.15}$$

Rearranging the Laplacian operator through

$$\frac{1}{r^2}\frac{\partial}{\partial r}\left[r^2\frac{\partial\phi}{\partial r}\right] = \frac{2}{r}\frac{\partial\phi}{\partial r} + \frac{\partial^2\phi}{\partial r^2} = \frac{1}{r}\frac{\partial}{\partial r}\left[\phi + r\frac{\partial\phi}{\partial r}\right] = \frac{1}{r}\frac{\partial^2(r\phi)}{\partial r^2}, \tag{2.16}$$

the wave equation simplifies even further to

$$\frac{\partial^2(r\phi)}{\partial r^2} = \frac{1}{c^2}\frac{\partial^2(r\phi)}{\partial t^2}. \tag{2.17}$$

2.2.1 Solving for the Acoustic Potential

Comparing the form of the wave equation for a spherically expanding wave with that for a plane wave, the only difference lies in the differentiated variable, $r\phi$ for a spherical wave and ϕ for a plane wave. Therefore, if a variable substitution of $v = r\phi$ is applied to equation 2.17, the solution for a plane wave can be applied to v. Thus, the solution of $r\phi$ takes the form

$$r\phi = f(ct \mp r). \tag{2.18}$$

Dividing through by r, the acoustic potential can be shown to be

$$\phi = \frac{f(ct \mp r)}{r}. \tag{2.19}$$

Now with the acoustic potential solved for, substitution of equation 2.19 into equation 2.10 produces an expression for the acoustic pressure associated with a spherically expanding wave,

$$p = \frac{\rho c}{r}\left(\frac{\partial\left[f(ct \mp r)\right]}{\partial t}\right). \tag{2.20}$$

Performing a similar substitution into equation 2.12, the expression for particle velocity becomes slightly more complicated than its counterpart in plane wave analysis. Since the gradient is the spatial derivative of the acoustic potential, derivation by parts must be implemented, yielding two components for particle velocity.

$$u = \frac{f(ct \mp r)}{r^2} \pm \frac{1}{r}\left(\frac{\partial\left[f(ct \mp r)\right]}{\partial r}\right) \tag{2.21}$$

2.2.2 Extension to particle acceleration and displacement

In this form, it can be seen that the relationships between displacement, velocity and acceleration are relatively complicated. Taking the temporal derivative of equation 2.21, the following relationship for acceleration is developed,

$$\dot{u} = \frac{1}{r^2}\frac{\partial f(ct \mp r)}{\partial t} \pm \frac{1}{r}\left(\frac{\partial^2\left[f(ct \mp r)\right]}{\partial r \partial t}\right). \tag{2.22}$$

Considering the form of the displacement, the integral of equation 2.21 must be evaluated. Thus, the basic form of the particle displacement has the form,

$$x = \int \left[\frac{f(ct \mp r)}{r^2} \pm \frac{1}{r}\left(\frac{\partial\left[f(ct \mp r)\right]}{\partial r}\right)\right] dt. \tag{2.23}$$

2.2.3 Separation of variables

Following the assumptions of string vibrations, separation of variable is assumed to be valid for this acoustic analysis, such that the acoustic potential can be separated into two components,

$$\phi = \varphi(r)\eta(t). \tag{2.24}$$

Thus

$$f(ct \mp r) = r\varphi(r)\eta(t) \tag{2.25}$$

With the acoustic potential in this form it is possible to place particle velocity and acoustic pressure in terms of these variables. Beginning with particle velocity, equation 2.21 takes the form

$$\begin{aligned} u &= \frac{r\varphi(r)\eta(t)}{r^2} \pm \frac{1}{r}\left(\frac{\partial\left(r\varphi(r)\eta(t)\right)}{\partial r}\right) \\ &= \left(\frac{\varphi(r)}{r} \pm \frac{1}{r}\left[\frac{\partial\left(r\varphi(r)\right)}{\partial r}\right]\right)\eta(t). \end{aligned} \tag{2.26}$$

Making a similar substitution for equation 2.20, acoustic pressure can be represented as

$$p = \frac{\rho c}{r}\left(\frac{\partial\left(r\varphi(r)\eta(t)\right)}{\partial t}\right) = \rho c\varphi(r)\dot{\eta}(t). \tag{2.27}$$

With the velocity and pressure of a spherically expanding wave defined, particle displacement and acceleration can be defined from equations 2.23 and 2.22 as,

$$x = \left(\frac{\varphi(r)}{r} \pm \frac{1}{r}\left[\frac{\partial(r\varphi(r))}{\partial r}\right]\right)\int \eta(t)dt, \tag{2.28}$$

$$\dot{u} = \left(\frac{\varphi(r)}{r} \pm \frac{1}{r}\left[\frac{\partial(r\varphi(r))}{\partial r}\right]\right)\dot{\eta}(t). \tag{2.29}$$

It would now be advantageous to define a new variable, $\beta(t)$ such that $\beta(t) = \int \eta(t)dt$, which would redefine particle displacement, velocity, and acceleration as:

$$x = \left(\frac{\varphi(r)}{r} \pm \frac{1}{r}\left[\frac{\partial\left(r\varphi(r)\right)}{\partial r}\right]\right)\beta(t), \tag{2.30}$$

$$u = \left(\frac{\varphi(r)}{r} \pm \frac{1}{r}\left[\frac{\partial\left(r\varphi(r)\right)}{\partial r}\right]\right)\dot{\beta}(t), \tag{2.31}$$

$$\dot{u} = \left(\frac{\varphi(r)}{r} \pm \frac{1}{r}\left[\frac{\partial\left(r\varphi(r)\right)}{\partial r}\right]\right)\ddot{\beta}(t). \tag{2.32}$$

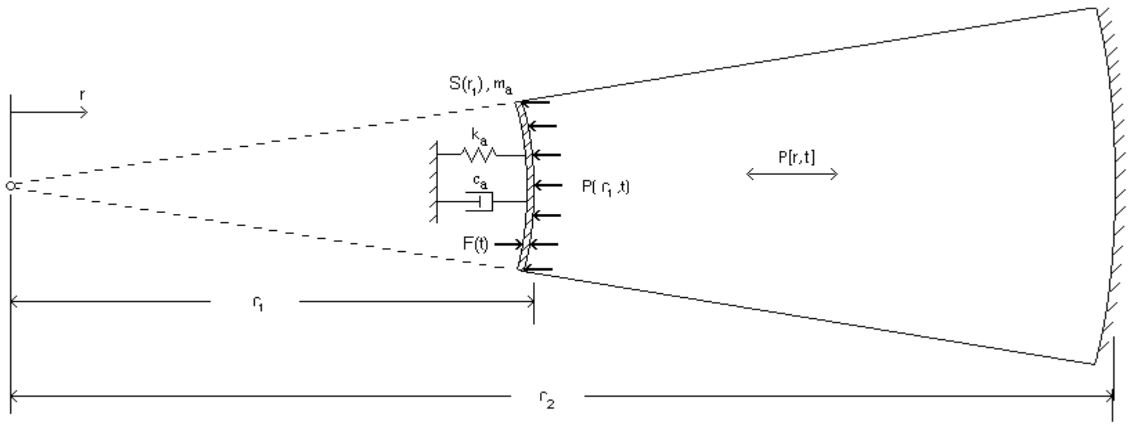

Figure 2.3: Parameters used to define a conical bore having reactive-rigid boundary conditions

Similarly, acoustic potential and pressure can be redefined in terms of this new $\beta(t)$ variable. As such, equations 2.24 and 2.27 take the following form,

$$\phi = \varphi(r)\dot{\beta}(t), \tag{2.33}$$

$$p = \rho c \varphi(r)\ddot{\beta}(t). \tag{2.34}$$

2.3 Boundary Value Problem in a Conical Bore

With the particle displacement, velocity, acceleration, acoustic potential and acoustic pressure defined, as in equations 2.30-2.34, it is now possible to consider solving the boundary condition problem associated with a conical bore having actuating-rigid boundary conditions.

2.3.1 Definition of boundary conditions

The simplest boundary condition to be considered for this system is comprised of a rigid termination at r_2, as in Figure 2.3. For this boundary condition, pressure is maximized, such that the derivative of pressure goes to zero at this location. Solving for the spatial derivative of pressure, the following relationship is developed,

$$\frac{\partial p}{\partial r} = \rho c \frac{\partial \varphi(r)}{\partial r}\ddot{\beta}(t). \tag{2.35}$$

Allowing this expression to go to zero, the boundary condition at r_2 takes the following form

$$BC_2 \longrightarrow \rho c \left[\frac{\partial \varphi(r)}{\partial r}\right]_{r \to r_2} = 0. \tag{2.36}$$

Now, considering the second boundary condition, that located at r_1, there exists a force balance which must be incorporated into the model. Considering a spring-mass-damper system, the force balance takes the form

$$m_a \dot{u}(r_1, t) = -k_a x(r_1, t) - c_a u(r_1, t) + F(t) - P(r_1, t) A_a. \tag{2.37}$$

Using the definitions of 2.30, 2.31, 2.32 and 2.34, the force balance can be rewritten in terms of the spatial and temporal components $\varphi(r)$ and $\beta(t)$,

$$\left(\frac{\varphi(r_1)}{r_1} \pm \frac{1}{r_1}\left[\frac{\partial\left(r\varphi(r)\right)}{\partial r}\right]_{r_1}\right)\left(m_a\ddot{\beta}(t) + c_a\dot{\beta}(t) + k_a\beta(t)\right) = F(t) - A_a\rho c\varphi(r_1)\ddot{\beta}(t). \tag{2.38}$$

Treating the boundary condition initially as a homogeneous system, the forcing function, $F(t)$ goes to zero, leaving the equation,

$$\left(\frac{\varphi(r_1)}{r_1} \pm \frac{1}{r_1}\left[\frac{\partial\left(r\varphi(r)\right)}{\partial r}\right]_{r_1}\right)\left(m_a\ddot{\beta}(t) + c_a\dot{\beta}(t) + k_a\beta(t)\right) + A_a\rho c\varphi(r_1)\ddot{\beta}(t) = 0. \tag{2.39}$$

As mode shapes develop in steady-state, it is assumed that the temporal component $\beta(t)$ takes the harmonic form $e^{j\omega t}$, which when applied to equation 2.39 reduces the force balance to

$$\left(\left(\frac{\varphi(r_1)}{r_1} \pm \frac{1}{r_1}\left[\frac{\partial\left(r\varphi(r)\right)}{\partial r}\right]_{r \to r_1}\right)\left(-\omega^2 m_a + j\omega c_a + k_a\right) - \omega^2 A_a\rho c\varphi(r_1)\right)\beta(t) = 0. \tag{2.40}$$

In this form, the temporal component can be divided out leaving only the spatial component of equation 2.40 as the boundary condition. Grouping terms the spatial term can be separated into factors, $\varphi(r)$ and $\frac{\partial(r\varphi(r)}{\partial r}$ such that the boundary condition at r_1 becomes

$$BC_1 \longrightarrow \left[\frac{\partial\left(r\varphi(r)\right)}{\partial r}\right]_{r \to r_1} = \mp\frac{\left[k_a - \omega^2(r_1 A_a\rho c + m_a)\right] + j\omega c_a}{\left[k_a - \omega^2 m_a\right] + j\omega c_a}\varphi(r_1). \tag{2.41}$$

With the boundary conditions now defined it is possible to solve for the resonance frequencies and mode shapes of the acoustic cavity.

2.3.2 Implementation of boundary conditions

Before applying the boundary conditions to this problem, the first step is to assume a form for the potential function $\phi(r,t)$. The standard assumption for the form of this function is the following (Bies, 1996),

$$\phi(r,t) = \left(\frac{A}{r}e^{jkr} + \frac{B}{r}e^{-jkr}\right)e^{j\omega t}. \tag{2.42}$$

However for further first order analysis of this function the temporal component shall be considered in a more general form as $\dot{\beta}(t)$, resulting in,

$$\phi(r,t) = \left(\frac{A}{r}e^{jkr} + \frac{B}{r}e^{-jkr}\right)\dot{\beta}(t). \tag{2.43}$$

Comparing this equation with equation 2.33, the spatial component, $\varphi(r)$, of the acoustic potential is seen to be

$$\varphi(r) = \left(\frac{A}{r}e^{jkr} + \frac{B}{r}e^{-jkr}\right). \tag{2.44}$$

Now, we have an assumed form of the spatial component of acoustic potential which can be used in conjunction with the boundary conditions to define the modal characteristics of the system. Beginning with the boundary condition at r_2, it is possible to solve for one of the coefficients. Setting the spatial derivative of equation 2.44 to zero and evaluating at r_2, the following equation develops

$$jkr_2\frac{A}{r_2}e^{jkr_2} + jkr_2\frac{B}{r_2}e^{-jkr_2} = 0. \tag{2.45}$$

Rearranging this equation and solving for A,

$$A = \frac{Be^{-2jkr_2}(kr_2 - j)}{kr_2 + j}. \tag{2.46}$$

Substituting this expression into equation 2.44, the boundary condition at r_1 can be applied, resulting in a function of wave number k and the unknown coefficient B. It is assumed that all other parameters, i.e. m_a, k_a, c_a, etc., are known. Substitution of equation 2.46 into equation 2.44 yields a spatial component of,

$$\varphi(r) = \frac{Be^{-jkr}}{r} + \frac{Be^{jkr}e^{-2jkr_2}(kr_2 - j)}{r(kr_2 + j)}. \tag{2.47}$$

This expression is in terms of the wave number k, but can be expressed as a function of ω by substituting $\omega = kc$, where c is the speed of sound. Thus, $\varphi(r)$ becomes

$$\varphi(r) = \frac{Be^{\frac{-j\omega r}{c}}}{r} + \frac{Be^{\frac{j\omega r}{c}} e^{\frac{-2j\omega r}{c}} (\frac{\omega}{c} r_2 - j)}{r(\frac{\omega}{c} r_2 + j)}. \tag{2.48}$$

Substituting this expression back into the first boundary condition, equation 2.41 becomes

$$\begin{aligned} &2\frac{(\sin \frac{\omega r_2}{c} + j \cos \frac{\omega r_2}{c})}{c_o r_1^2 (c_o - j r_2 \omega)} \left(\left[c_o \omega ((k_a - m_a \omega^2)(r_1 - r_2) + \rho S(r_1) r_1 r_2 \omega^2) \right] cos \left(\frac{(r_1 - r_2)\omega}{c_o} \right) \right. \\ &+ \left[(\omega^2 m_a - k_a)(c_o^2 + r_1 r_2 \omega^2) + c_o^2 \omega^2 \rho S(r_1) r_1 \right] sin \left(\frac{(r_1 - r_2)\omega}{c_o} \right) \\ &\left. + j \left[\left[c_o \omega^2 c_a (r_1 - r_2) \right] cos \left(\frac{(r_1 - r_2)\omega}{c_o} \right) - \left[\omega c_a (c_o^2 + r_1 r_2 \omega^2) \right] sin \left(\frac{(r_1 - r_2)\omega}{c_o} \right) \right] \right) = 0. \end{aligned} \tag{2.49}$$

Looking at this equation, the only variable present is frequency, ω. The remaining parameters are physical constants defined by the system under analysis. Considering this, the natural frequencies of the system correspond to those values of ω which satisfy equation 2.49. Closer examination of equation 2.49 reveals that the first term, $\sin \frac{\omega r_2}{c} + j \cos \frac{\omega r_2}{c}$, will never go to zero. Therefore, the natural frequencies can be determined as the solutions of equation 2.50,

$$\begin{aligned} &\left(\frac{\left[c_o \omega ((k_a - m_a \omega^2)(r_1 - r_2) + \rho S(r_1) r_1 r_2 \omega^2) \right] + j \left[c_o \omega^2 c_a (r_1 - r_2) \right]}{c_o r_1^2 (c_o - j r_2 \omega)} \right) cos \left(\frac{(r_1 - r_2)\omega}{c_o} \right) \\ &+ \left(\frac{\left[(\omega^2 m_a - k_a)(c_o^2 + r_1 r_2 \omega^2) + c_o^2 \omega^2 \rho S(r_1) r_1 \right] - j \left[\omega c_a (c_o^2 + r_1 r_2 \omega^2) \right]}{c_o r_1^2 (c_o - j r_2 \omega)} \right) sin \left(\frac{(r_1 - r_2)\omega}{c_o} \right) \end{aligned} \tag{2.50}$$

as illustrated in Figure 2.4.

In Figure 2.50 both real and imaginary components are plotted as functions of frequency. From this figure it can be seen that both real and imaginary components go to zero simultaneously. Therefore, to determine the solutions of this expression we only have to consider the either the real or the imaginary coefficients. Considering only the real component of this figure there still exist the transcendental relationships which impede the development of an exact solution for the lower resonance frequencies. Using a minimization package the magnitude of the real component was used to identify each of the system's resonant frequencies. Therefore, having attained the natural frequencies of the system a corresponding set of mode shapes can be developed.

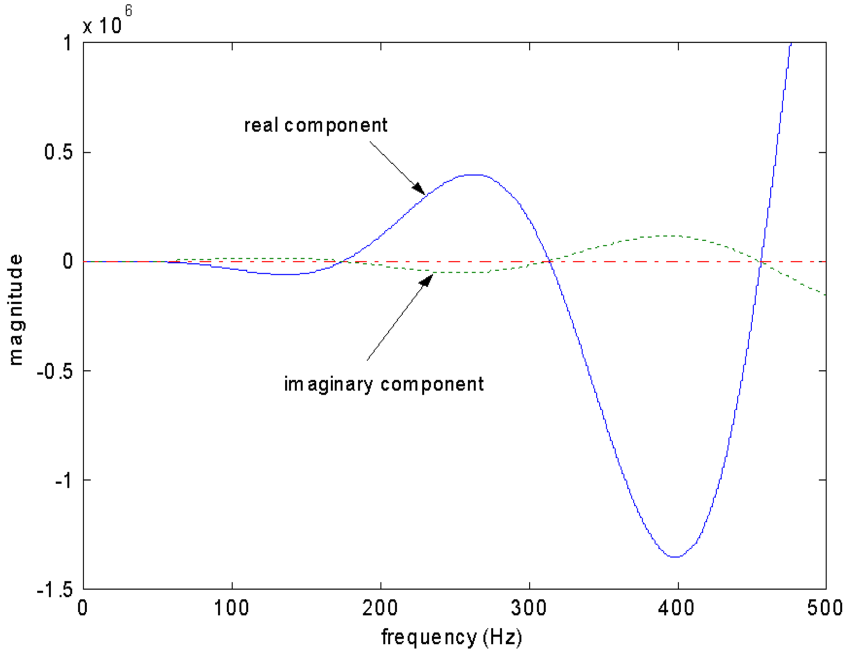

Figure 2.4: Transcendental relationship for natural frequencies of an actuating-closed conical bore

2.3.3 Acoustic mode shapes

Beginning with the general form of $\varphi(r)$ from equation 2.47 the only term that remains unknown is the coefficient B. Choosing to normalize this set of eigenfunctions, we follow the techniques summarized by Inman (2001). Defining the eigenfunction as $X_n(r)$ we consider the set to be normal if

$$\int_{r_1}^{r_2} X_n(r)X_n(r)dr = 1, \tag{2.51}$$

for each value of n. Substituting $r\varphi_n(r)$ in for $X_n(r)$ will yield a set of normalized coefficients for B. One issue with this normalization technique is that upon solving for B, Galerkin approximation methods will be used to develop a set of mass and stiffness matrices. Using the normalization approach of equation 2.51, the diagonal terms of the mass matrix are not guaranteed to be unity. Therefore we chose to mass normalize the system by applying

$$\frac{1}{c^2}\int_{r_1}^{r_2} \left[r\varphi_n(r)\right]\left[r\varphi_n(r)\right] dr = 1. \tag{2.52}$$

Solving this equation for B yields a set of coefficients that mass normalize the system,

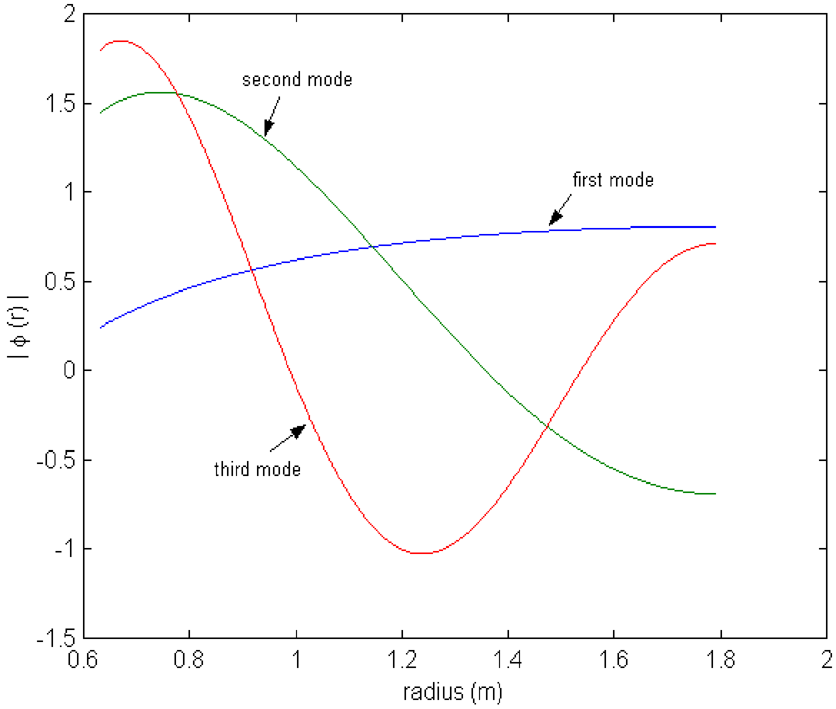

Figure 2.5: First three acoustic modes for actuating-closed conical bore.

defined as

$$B = \frac{1}{\sqrt{\frac{1}{c^2}\int_{r_1}^{r_2}\left[r\varphi(r)\right]^2 dr}}. \tag{2.53}$$

With the coefficient B known the mode shapes for acoustic potential and pressure are known and take the form,

$$\varphi(r) = \frac{1}{\sqrt{\frac{1}{c^2}\int_{r_1}^{r_2}\left[r\varphi(r)\right]^2 dr}}\left[\frac{e^{-jkr}}{r} + \frac{e^{jkr}e^{-2jkr_2}(kr_2 - j)}{r(kr_2 + j)}\right]. \tag{2.54}$$

Figure 2.5 illustrates the first three mode shapes of a conic section having the mechanical properties defined in Table 2.1. In this figure the presence of an actuating boundary condition is evident by nonzero pressure and nonzero slope at r_1. As the mass and stiffness quantities increase, the mode shapes will approach those of a conical bore having closed-closed boundary conditions, where the pressure at r_1 is maximized and $\frac{\partial p}{\partial r}$ at this location goes to zero. Conversely, as the mass and stiffness approach zero, the mode shapes will approach those of an open-closed conical bore in which the pressure at r_1 is equal to zero.

Table 2.1: Geometric, electrical and mechanical parameters of the experimental set-up. These values are used for analytical models.

Geometric parameters		Electrical parameters		Mechanical parameters	
Variable	Values	Variable	Values	Variable	Values
r_1	0.63 m	R	6.60 Ω	m_a	18.38 g
r_2	1.79 m	L	930.00 mH	k_a	851.79 $\frac{\mathrm{N}}{\mathrm{m}}$
		Bl	6.77 Tesla	θ	0.217 radians
				$S(r_1)$	0.0214 m^2

From equations 2.30-2.32, it is seen that the mode shapes corresponding to particle displacement, velocity and acceleration are defined as the spatial derivative of $\varphi(r)$. Differentiation of equation 2.54 yields a set of mode shapes of the following form,

$$\frac{\partial\varphi(r)}{\partial r} = \frac{1}{\sqrt{\frac{1}{c^2}\int_{r_1}^{r_2}\left[r\varphi(r)\right]^2 dr}}\left[\frac{e^{-jkr}\left(1+jkr\right)}{r^2} + \frac{e^{jkr}e^{-2jkr_2}(kr_2 - j)\left(1-jkr\right)}{r^2(kr_2+j)}\right], \quad (2.55)$$

where k is defined as the set of wave numbers associated with the resonance frequencies of the cavity.

2.4 Equation of Motion for Unforced System

With the natural frequencies and mode shapes of the system defined, the dynamics of the system can be defined through a set of matrix equations,

$$M\frac{\partial^2\ddot{\beta}(t)}{\partial t^2} + K\ddot{\beta}(t) = 0 \quad (2.56)$$

Following modal approximations common in most vibrations textbooks Inman (2001); Meirovitch (1997), a Galerkin approximation is used to develop the mass M and stiffness K matrices as,

$$M_{i,j} = \int_{r_1}^{r_2} [r\varphi_i(r)]\,[r\varphi_j(r)]\,dr \tag{2.57}$$

$$K_{i,j} = -c_o^2 \int_{r_1}^{r_2} [r\varphi_i(r)]\,\frac{\partial^2\,[r\varphi_j(r)]}{\partial r^2} dr \tag{2.58}$$

One interesting note concerning the development of these matrices is the form of the stiffness matrix. Due to the nature of the mode shapes associated with the actuating-rigid boundary conditions is that they do not generate an orthogonal set. This leads to the conclusion that the system is not self-adjoint and as such, leads to an asymmetric stiffness matrix. The proof of this asymmetry is presented in Appendix A, along with a discussion as to its effects on analysis of system controllability.

2.5 Analytical Validation of the Modal Model

Despite the asymmetries of the system, the eigenvalues and eigenfunctions of the system can be determined, yielding the natural frequencies and mode shapes of the system. Due to the nature of the boundary condition at r_1, variations in the mass m_a, damping c_a and stiffness k_a variables can approximate any resistive boundary from free to rigid. By setting the mass, damping and stiffness to zero, BC_1 of equation 2.41 represents a free or open boundary condition. Alternately, if mass and stiffness are driven to ∞ and damping is maintained at 0, BC_1 models a rigid or closed boundary. Due to this ability to model the extreme conditions, analytical validation of the system can be achieved by comparison with the results of a study by Ayers *et al.* (1985). In their research, these authors investigated the resonance frequencies and standing waves of conical bores having four different arrangements of boundary conditions. Considering the open-open, open-closed, closed-open and closed-closed boundary conditions, transcendental equations were developed from which the natural frequencies could be determined. For comparative purposes, the transcendental equations developed by these authors for open-closed (Eq. 2.59) and closed-closed (Eq. 2.60) systems are as follows (Ayers 531-532).

$$\tan[\pi f_A/f_{A_o}] = \frac{1}{1-B}\pi f_A/f_{A_o} \tag{2.59}$$

$$\tan[\pi f_A/f_{A_o}] = \frac{1}{1+\frac{B}{(1-B)^2}(\pi f_A/f_{A_o})^2}\pi f_A/f_{A_o} \tag{2.60}$$

Table 2.2: Comparison of actuation model with models developed by Ayers *et al.* (all values in Hz).

	Closed-Closed		Open-Closed	
Freq	Author's model	Ayers *et al.*'s model	Author's model	Ayers *et al.*'s model
f_1	1.15	0.00	46.62	46.62
f_2	161.90	161.90	214.76	214.76
f_3	303.51	303.51	365.05	365.05
f_4	448.52	448.52	513.76	513.76
f_5	594.72	594.72	661.97	661.97
f_6	741.45	741.45	809.95	809.95
f_7	888.45	888.45	957.80	957.80
f_8	1035.62	1035.62	1105.59	1105.59
f_9	1182.89	1182.89	1253.32	1253.32

where

$$\begin{aligned} B &= \frac{r_1}{r_2} \\ f_{A_o} &= \frac{c}{2(r_2 - r_1)} \end{aligned}$$

With these equations, it is possible to determine the accuracy of our model at its extreme conditions. Evaluating both equations and determining the first nine resonances, the results are presented in Table (3.1). Comparing the predicted values of both ours and Ayers' models, all of the frequencies match exactly with the only exception being f_1 of the closed-closed geometry. This inaccuracy in the first resonance is due to our inability to actually apply an infinite mass and stiffness for BC_1. Instead, using very large values ($*10^6$) a rigid boundary condition was approximated. While it is seen that the higher order modes are predicted accurately with such values of mass and stiffness, it was seen that f_1

approaches zero as the m_a and k_a are continually increased. Thus indicating that our model will yield the same results as Ayers *et al.* by taking the limit of equation 2.50 as m_a and k_a go to ∞.

While these results indicate that the actuating-closed model accurately predicts the resonance frequencies of its extreme conditions, experimental results are necessary to validate the intermediate range in which an actuator having a finite mass and stiffness is applied at r_1. These comparisons are presented in Chapter 5.

2.6 Chapter Summary

In this chapter the development of a dynamic model for the homogeneous system has been presented using modal approximation techniques. Beginning with the basic acoustic equations, boundary conditions were applied at each of the end conditions. Developing a set of transcendental equations that define the system's natural frequencies, these values were determined iteratively using the real component of the characteristic equations. Solving for the natural frequencies of the system a set of mode shapes were developed such that each was mass normalized. Using Galerkin approximation methods to develop a system of mass and stiffness matrices, a matrix representation of the homogeneous wave equation has also been derived. Using previously developed models for rigid-rigid and open-rigid configurations of the conic section, the predicted values of our model have been verified at the extreme conditions at which mass and stiffness either disappear or become infinite. In the next chapter a different modeling approach is used to characterize the actuating-rigid conical bore. Using impedance methods, the next approach is found to model the system dynamics accurately as well and provide another comparison for the modal approximation method.

Chapter 3

Impedance Model of a Conical Bore

While the modal characterization developed in Chapter 2 accurately predicts the resonance frequencies and illustrates the mode shapes of the passive system, an impedance model is more effective for control purposes. Modeling the acoustic impedance of the cavity of Figure 2.3, a transducer model of the system can be developed which illustrates how the acoustic system can be coupled with the speaker's mechanical and electrical dynamics. Using this electromechanical model, a first order form representation of the full system can be developed, relating input voltage to output pressure within the cavity. In this form feedback control techniques can be directly applied for control simulation and implementation. The remainder of this chapter presents the development of the transducer model along with its transformation into a state-space representation of the coupled system.

3.1 Electrical equivalent to acoustic system

Again considering the enclosure of Figure 2.3 it can be seen that the system is composed of three separate dynamic subsystems. The spring-mass-damper system represents the mechanical dynamics of the actuator, while the cavity represents the acoustic dynamics of the conical bore. The third subsystem is slightly less obvious and is represented by the forcing term $F(t)$. Expanding this term further it can be seen that the applied force is related directly to the electrical dynamics of the actuator, along with the back electromotive force induced by pressures on the actuator face. By dividing the overall system of Figure

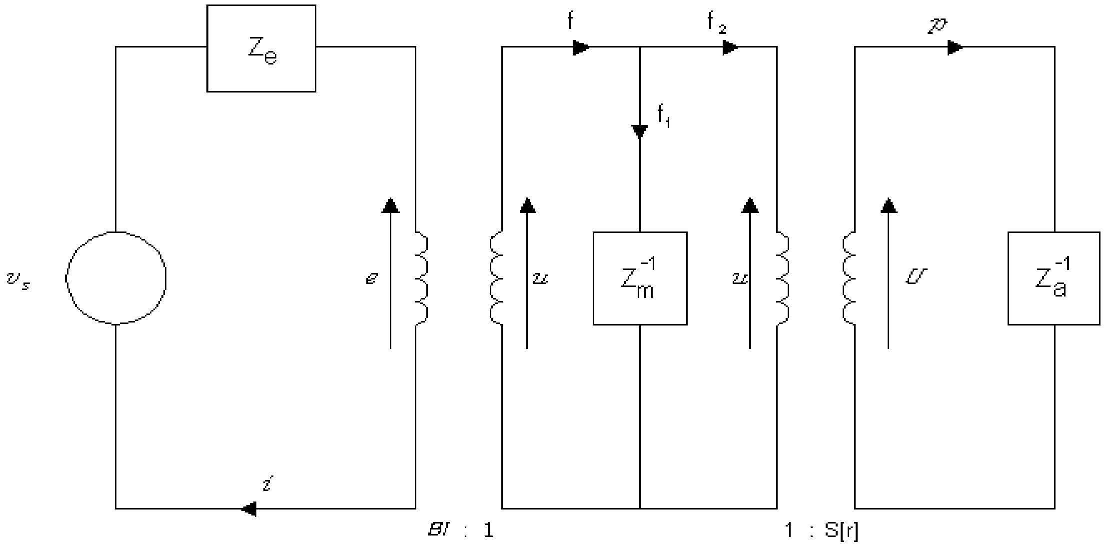

Figure 3.1: Transducer model of speaker and cavity system.

2.3 into subsystems, it is possible to develop a transducer model of the full system, as shown in Figure 3.1. Similar to the transducer model used by Leo (2000) three impedances exist, each corresponding to the electrical, mechanical and acoustic impedances. Each of these frequency dependent impedances are represented by a block within the transducer diagram, labeled as z_e, z_m and z_a. Individual loops correspond to each subsystem with transformer relationships between each loop. Establishing a set of governing equations for the system, the following expressions exist for each loop.

$$v_{in} + z_e i - e = 0 \tag{3.1}$$

$$u + z_m^{-1} f_1 = 0 \tag{3.2}$$

$$U + z_a^{-1} p = 0 \tag{3.3}$$

Each of these loops are also related by coupling terms, such that a set of relationships between e,u,U,i,f,f_2 and p also exist. These relationships are

$$\begin{aligned} e &= Blu \qquad & U &= S(r)u \\ f &= Bli \qquad & f_2 &= S(r)p \end{aligned} \tag{3.4}$$

Applying each of these relationships to equations 3.1-3.3, transfer functions between any two variables can be developed. If we consider the system as a whole, the most applicable transfer function relates the pressure within the cavity to the applied voltage to the actuator. In order to develop this relationship we first begin with the transfer function relating voltage to current. Starting with the second loop in the transducer diagram, we consider the node at which f, f_1 and f_2 meet. Summing the forces at this node, we find that $f = f_1 + f_2$. Substituting the relationships from equation 3.4 a more general expression in terms of current, velocity and pressure can be developed.

$$Bli = -z_m u + S(r)p \tag{3.5}$$

Again considering the relationships of equation 3.4, pressure can be redefined as a function of volume velocity, which in turn can be defined as a function of velocity. Applying these substitutions, equation 3.5 becomes

$$\begin{aligned} Bli &= -z_m u + S(r)[-z_a S(r)u] \\ &= (z_m + z_a S(r))u \end{aligned} \tag{3.6}$$

Solving this expression for velocity,

$$u = \frac{-Bl}{z_m + z_a S(r)} i \tag{3.7}$$

Next consider the electrical loop of the transducer model of Figure 3.1. Loop closure of this component of the transducer model results in a function of input voltage, current and back electromotive voltage. But, as seen in the relationships of equation 3.4 this back electromotive voltage can be represented as a function of velocity, which we have just solved for in terms of current. Applying the result of equation 3.7 to the relationship $e = Blu$ and substituting into equation 3.1 we develop a single equation which is only a function of input voltage and current.

$$v_{in} + z_e i - Bl \frac{-Bl}{z_m + z_a S(r)} i = 0 \tag{3.8}$$

Rearranging terms and solving for the ration of voltage to current, the following relationship develops,

$$\frac{v_{in}}{i} = \frac{-Bl^2 + z_e z_m + z_a z_e S(r)^2}{z_m + z_a S(r)^2} \tag{3.9}$$

The second transfer function of interest is the ratio of pressure to current. Beginning with the same equation used to develop the voltage to current relationship, we solve equation 3.5 for pressure instead of current.

$$S(r)p = Bli - z_m u \tag{3.10}$$

With the results of equation 3.7 we can make a substitution for velocity which reduces equation 3.10 to a function of pressure and current.

$$S(r)p = Bli - z_m \frac{Bl}{z_m + z_a S(r)} i \tag{3.11}$$

Simplifying this expression and dividing through by i, the transfer function of pressure to current can be developed.

$$\frac{p}{i} = \frac{Blz_a S(r)}{z_m + z_a S(r)^2}. \tag{3.12}$$

Once the two relationships of voltage to current and pressure to current have been developed, the transfer function between pressure and voltage is obtained by multiplying equation 3.12 by the inverse of equation 3.9, resulting in

$$\frac{p}{v_{in}} = \frac{-Blz_a S(r)}{Bl^2 + z_e z_m + z_a z_e S(r)^2}. \tag{3.13}$$

Thus, if the forms for the impedances z_e, z_m and z_a are implemented, the frequency domain transfer function related to equation 3.13 can be developed.

3.2 Model development

With the pressure to voltage relationship of equation 3.13, classical control techniques could be implemented to apply PID or lead-lag controllers. However, in order to implement more modern control techniques, a state form of the input-output relationship is necessary. A state representation could be obtained directly from equation 3.13, but the physical interpretation of the individual states would not be guaranteed. Thus, in our development of the state-space system two separate models, one of the actuator and one of the cavity, are developed and then coupled through the particle and piston velocities.

3.2.1 Speaker Equations

Beginning with the governing equations for the electrical components of the acoustic actuator, the electrical impedance can be derived when considering the diagram of Figure 3.2. As a function of current, z_e takes the form

$$z_e = R + j\omega L \tag{3.14}$$

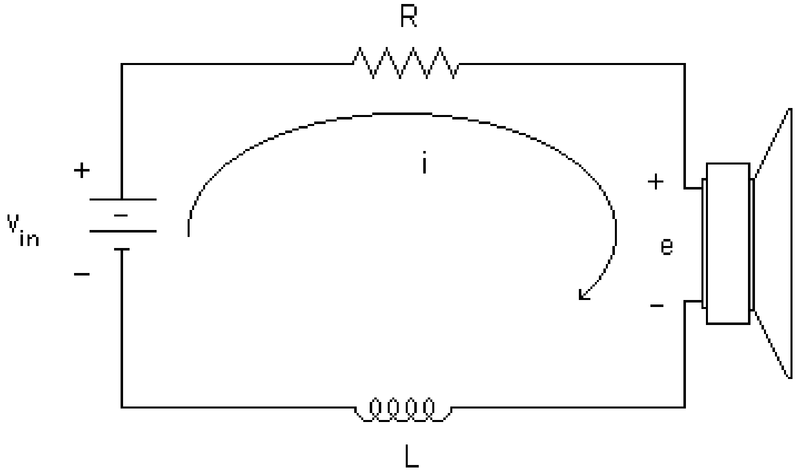

Figure 3.2: Electric circuit of a permanent magnet speaker

Implementing this relationship into equation 3.1, the equation of motion for the electrical system becomes

$$v_{in} - (R + j\omega L)i - e = 0. \tag{3.15}$$

Similarly, the mechanical impedance of the spring-mass-damper system z_m is related to the displacement x of the system. Considering this, the mechanical impedance takes the form

$$z_m = -\omega^2 m_a + j\omega c_a + k_a. \tag{3.16}$$

Substituting this into equation 3.2, the equation of motion for the mechanical dynamics of the actuator becomes

$$(-\omega^2 m_a + j\omega c_a + k_a)x = f_1. \tag{3.17}$$

Relating the mechanical block of Figure 3.1 with the schematic of Figure 3.3, the applied force f_1 is seen to take the form $Bli - S(r_1)p$. Applying this substitution to equation 3.17 expands the mechanical equation of motion to

$$(-\omega^2 m_a + j\omega c_a + k_a)x = Bli - S(r_1)p. \tag{3.18}$$

In the formulation of these impedances one primary assumption is that the system has achieved steady state. Oscillating harmonically, the conventional form of the temporal

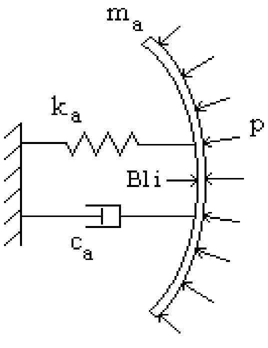

Figure 3.3: Spring-mass-damper system subjected to an applied force *Bli* and applied pressure *p*.

component can be given as $e^{i\omega t}$ (Kinsler, 1997; Bies, 1996). Applying this harmonic function it can be seen that the n^{th} derivative of the function $e^{i\omega t}$ takes the form $(i\omega)^n e^{i\omega t}$. This facilitates the development of frequency domain transfer functions from equations 3.15 and 3.18. However, as stated above the desired form of this system is a state-space representation coupling speaker dynamics with the acoustic equations. When considering the state-space form of the speaker equations, the full equations of motions for equations 3.15 and 3.18 are desired. Retracting the steady-state assumption, the electrical equation of motion takes the more general form

$$v_{in} - Ri - L\frac{di}{dt} - e = 0. \tag{3.19}$$

Similarly, the mechanical equation of motion can be represented as

$$m_a\dot{u} + c_a u + k_a x = Bli - S(r_1)p. \tag{3.20}$$

To generate the full state-space representation a suitable set of states must be defined. Defining these speaker states as x, u, and i, the state equations associated with the speaker are,

$$\begin{aligned}
\left\{\begin{array}{c} \dot{x} \\ \dot{u} \\ \frac{di}{dt} \end{array}\right\} &= \left[\begin{array}{ccc} 0 & 1 & 0 \\ -\frac{k_a}{m_a} & 0 & \frac{Bl}{m_a} \\ 0 & -\frac{Bl}{L} & -\frac{R}{L} \end{array}\right] \left\{\begin{array}{c} x \\ u \\ i \end{array}\right\} + \left[\begin{array}{c} 0 \\ -\frac{S(r_1)}{m_a} \\ 0 \end{array}\right] p + \left[\begin{array}{c} 0 \\ 0 \\ \frac{1}{L} \end{array}\right] v_{in} \\
y &= \left[\begin{array}{ccc} 0 & 1 & 0 \end{array}\right] \left\{\begin{array}{c} x \\ u \\ i \end{array}\right\}. \qquad (3.21)
\end{aligned}$$

In this form, there are two input-output relationships, that between voltage and velocity and that between pressure and velocity. It is this second input-output equation which enables this system to be coupled with the acoustic model developed in the next section.

3.2.2 Cavity Equations

As with the speaker equations, the acoustic model begins with its corresponding governing equation from the transducer model, equation 3.3. However, unlike the speaker equations the form of this acoustic impedance is not as straightforward as the electrical and mechanical impedances. In order to properly determine the acoustic impedance of this system we must first begin with the assumed form of acoustic potential,

$$\phi(r,t) = \left(\frac{A}{r}e^{jkr} + \frac{B}{r}e^{-jkr}\right)e^{j\omega t}. \qquad (3.22)$$

Remembering that the acoustic pressure is related to $\phi(r,t)$ as $p(r,t) = \rho\frac{\partial\phi(r,t)}{\partial t}$, it can be seen that volume velocity is also related to $\phi(r,t)$ as $U(r,t) = -S(r)\frac{\partial\phi(r,t)}{\partial r}$. Defining the desired acoustic impedance as the ratio of p to U, we divide the equivalent form of pressure,

$$p(r,t) = j\omega\left(\frac{A}{r}e^{jkr} + \frac{B}{r}e^{-jkr}\right)e^{j\omega t}. \qquad (3.23)$$

by the equivalent form of volume velocity.

$$U(r,t) = -S(r)\left(jk\frac{A}{r}e^{jkr} - jk\frac{B}{r}e^{-jkr} - \frac{A}{r^2}e^{jkr} - \frac{B}{r^2}e^{-jkr}\right)e^{j\omega t}. \qquad (3.24)$$

Applying these relationships and dividing through, the acoustic impedance becomes

$$z_a = \frac{(B + Ae^{2jkr})r\rho\omega}{S(r)\left[B(kr - j) - Ae^{2jkr}(kr + j)\right]}. \tag{3.25}$$

In this equation one of the constants A or B can be solved for considering the rigid boundary condition at r_2. At this rigid termination, the pressure will be maximized such that $\frac{\partial p}{\partial r} = 0$. Applying this boundary condition, the constant A is found to be

$$A = \frac{(kr_2 - j)Be^{-2jkr_2}}{kr_2 + j}. \tag{3.26}$$

Substituting this back into equation 3.25 and simplifying, the acoustic impedance at r_1 becomes

$$z_a = \frac{\left(e^{2jkr_1}(kr_2 - j) + e^{2jkr_2}(kr_2 + j)\right) r_1\rho\omega}{\left(-e^{2jkr_1}(kr_2 - j)(kr_1 + j) + e^{2jkr_2}(kr_1 - j)(kr_2 + j)\right) S(r_1)} \tag{3.27}$$

For control purposes, it is desired that this relationship be represented in either s-plane or state-space form. Extracting the resonance and antiresonance frequencies from the frequency response of the acoustic impedance, an s-plane representation of the system can be developed.

$$\frac{P(s)}{U(s)} = \frac{(s^2 + w_{z1}^2)(s^2 + w_{z2}^2)...(s^2 + w_{zm}^2)}{s(s^2 + w_{p1}^2)(s^2 + w_{p2}^2)...(s^2 + w_{pn}^2)}. \tag{3.28}$$

From this transfer function, a state-space representation can be obtained through a canonical transformation, yielding a system in modal form.

$$\begin{aligned}
\dot{q_c} &= \begin{bmatrix} 0 & 0 & ... & 0 \\ 0 & \begin{bmatrix} -\zeta\omega_{p_1} & \omega_{d_1} \\ -\omega_{d_1} & -\zeta\omega_{p_1} \end{bmatrix} & ... & 0 \\ \vdots & \vdots & \ddots & \vdots \\ 0 & 0 & ... & \begin{bmatrix} -\zeta\omega_{p_n} & \omega_{d_n} \\ -\omega_{d_n} & -\zeta\omega_{p_n} \end{bmatrix} \end{bmatrix} q_c + \begin{bmatrix} b_1 \\ b_2 \\ b_3 \\ \vdots \\ b_{2n} \\ b_{2n+1} \end{bmatrix} U \\
P &= \begin{bmatrix} c_1 & c_2 & c_3 & ... & c_{2n} & c_{2n+1} \end{bmatrix} q_c
\end{aligned} \tag{3.29}$$

where ω_{d_n} is defined as $\omega_{p_n}\sqrt{1 - \zeta^2}$.

The corresponding input-output relationship of volume velocity to pressure is defined in first order form by the set of matrices A_c, B_c and C_c. In this form, the state matrix A_c is block diagonal with one feed-through term corresponding to the first row of zeros while the input matrix B_c defines the individual modal weightings for the input.

3.3 Coupled State-Space Model

From equations 3.21 and 3.29 a representation of the coupled system can be developed, relating acoustic pressure to input voltage. Denoting the state, input and output matrices of the speaker equations as A_a, B_a^v, B_a^p and C_a and the states as q_a, the full state-space representation takes the form,

$$\begin{aligned}\left\{\begin{array}{c}\dot{q}_a\\ \dot{q}_c\end{array}\right\} &= \left[\begin{array}{cc}A_a & B_a^p C_c\\ S(r_1)B_c C_a & A_c\end{array}\right]\left\{\begin{array}{c}q_a\\ q_c\end{array}\right\}+\left[\begin{array}{c}B_a^v\\ 0\end{array}\right]v_{in}\\ P &= \left[\begin{array}{cc}0 & C_c\end{array}\right]\left\{\begin{array}{c}q_a\\ q_c\end{array}\right\}\end{aligned} \tag{3.30}$$

Coupled through the off-diagonal terms $B_a^p C_c$ and $S(r_1)B_c C_a$, the speaker and acoustic states are related such that the overall input-output relationship exists between voltage and pressure. Formed from the collocated impedance the output matrix yields the total sound pressure level at the speaker face. For control applications feedback control can be applied by feeding this pressure back through a compensator that regulates the input voltage necessary to attenuate sound levels within the cavity.

While the development of this models follows theoretical arguments, actual application to a sample geometry is necessary to validate the model and its predicted results. In the next section the results of this impedance model are compared with the results of the modal model of Chapter 2, providing a base point for the experimental comparisons later discussed in Chapter 5.

3.4 Application to a Sample Geometry

As with the modal model the geometric, electrical and mechanical parameters of a sample system are applied to the impedance based model. Choosing these parameters to model the our experimental set-up, the values are tabulated in Table 2.1. Applying these values to the transducer model discussed in this section, comparisons are made between the frequency domain, s-plane and state-space models used to represent the impedance based model of the acoustic cavity. Following this the resonances of the coupled system are compared to those predicted by the modal model of Chapter 2. Establishing an analytical comparison

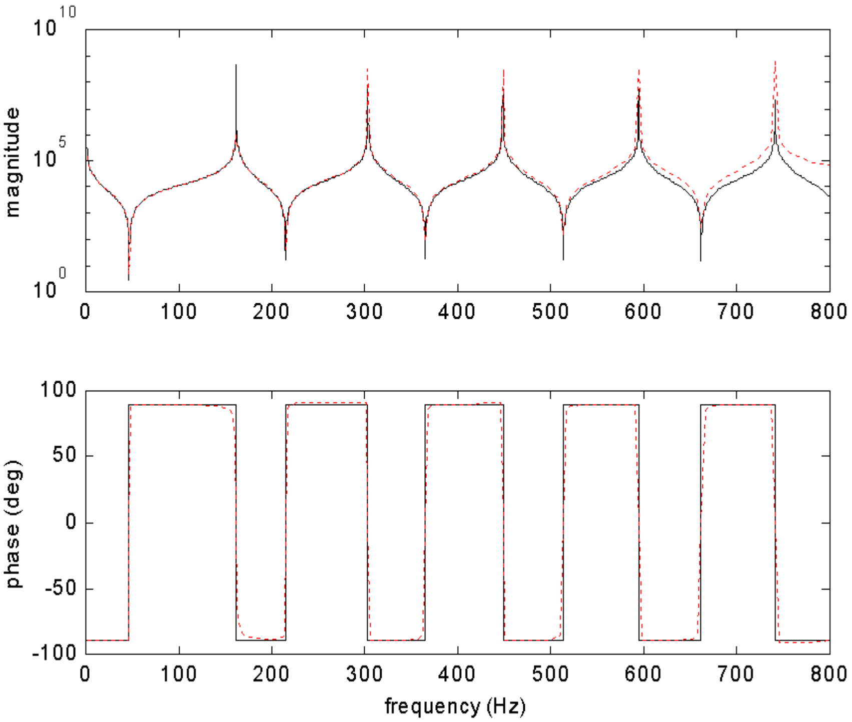

Figure 3.4: Comparison of impedance (solid), s-plane (dashed) and state-space (dotted) models.

between two independent models, the relative accuracy between these models is examined, providing baseline for comparison with experimental results to be discussed in Chapter 5.

3.4.1 Comparison of cavity models: frequency-domain, s-plane and state-space representations

Figure 3.4 presents the frequency response of each of these systems for a frequency range containing five acoustic modes. The magnitude and phase characteristics of both the s-plane and state-space models match almost exactly, and provide good models of the system impedance for lower frequency modes. However, at higher resonance frequencies the corresponding damping is overestimated producing wider resonances peaks. Increasing the order of the model will improve the fit of the lower resonance peaks, but for our application the first three modes are of greatest importance. Therefore a five mode approximation is seen to be sufficient.

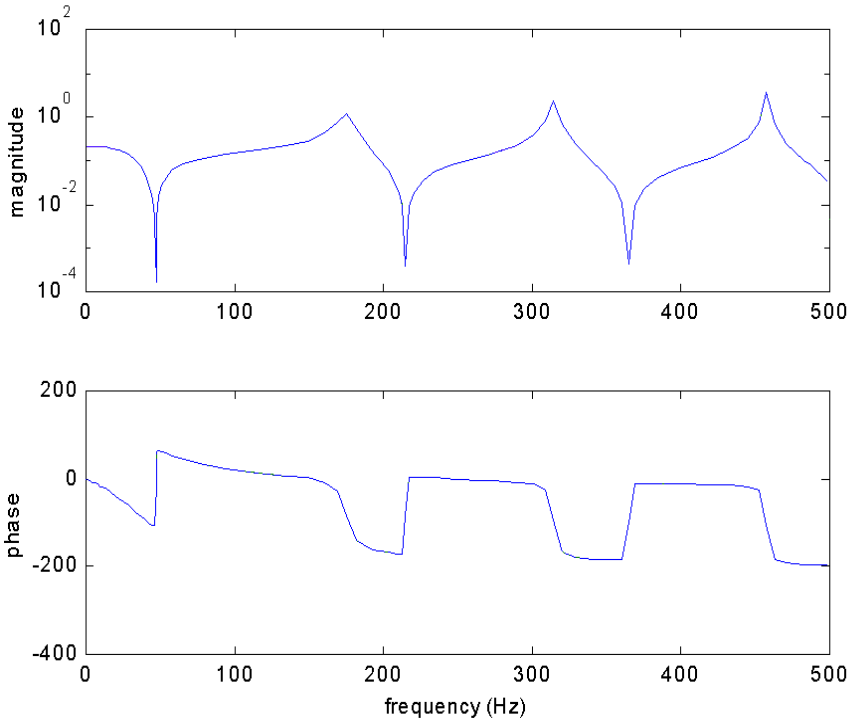

Figure 3.5: Open-loop frequency response of the fully coupled system.

3.4.2 Comparison of Modal and Impedance Predictions

Coupling the state-space model, represented as the dotted curve of Figure 3.4 with the actuator model of equation 3.21, the frequency response of the full system is shown in Figure 3.5. From this system, defined by equation 3.30, the natural frequencies are determined. Tabulating these values in Table 3.1 it is seen that each model predicts nearly the same resonances for the system. With discrepancies limited to 0.83%, the precision between the modal and impedance based models is very good. One important note concerning this comparison is that the models are taken for a current to pressure relationship. This input-output relationship was chosen for comparison because that was the final form of the modal model developed in Chapter 2. Incorporating the electrical dynamics of equation 3.15 results in a 2.73% increase in the first resonance. While the effects of the electrical equation are primarily limited to f_1, they must be noted, especially for the later experimental comparisons.

The correlation between these two models provides confidence in the development of this model as each were derived independent of one another. With the ability to relate

Table 3.1: Comparison of resonance frequencies from modal and impedance based models(all values in Hz).

Freq	Modal based	Impedance based	Error
f_1	38.41	38.43	0.052%
f_2	175.16	175.34	0.10%
f_3	313.28	313.64	0.11%
f_4	455.81	456.43	0.083%
f_5	600.44	601.35	0.015%
f_6	746.13	747.04	0.12%
f_7	892.40	894.31	0.21%
f_8	1039.03	1042.26	0.31%
f_9	1185.89	1195.74	0.83%

pressure to voltage through the state-space representation of equation 3.30, a good platform for control design has been developed. The accuracy of this model is further demonstrated in Chapter 5 which focuses on the experimental validation of both the modal and impedance models. However, we next investigate the control design used to implement feedback control on the system. Chapter 4 presents this development and the overall form of the compensator designed and implemented on the experimental testbed.

3.5 Chapter Summary

In this chapter the development of an impedance based model has been presented. Using a transducer model to provide insight into the coupling between mechanical, electrical and acoustic components of the overall system, transfer functions between acoustic pressure and applied voltage were determined. The overall acoustic impedance of a conical cavity was also derived as a function of the geometric parameters of the enclosure. Expanding this impedance model to a s-plane representation, a transformation into first order form was conducted using modal canonical methods. With a block diagonal state matrix and a modal weighting of the input, this state-space model of the acoustic cavity was then coupled with the state-space model of a permanent magnet speaker. The predicted resonance values of this model were then compared to those obtained using modal approximation methods illustrating a high degree of correlation between the two modeling techniques. Due to the relative size and speed of computation associated with the impedance model, this method was chosen to generate the plant model used in control design and simulation. The next chapter presents the development of controllers using Linear Quadratic Regulator and Positive Position Feedback techniques with a discussion of the simulated responses and a comparison of each design method.

Chapter 4

Control Design

With the state-space representation developed in the previous chapter, a suitable model exists upon which feedback control can be designed and simulated. Through our design process two separate design techniques were used to develop control algorithms, Linear Quadratic Regulator (LQR) and Positive Position Feedback (PPF). LQR was chosen as the first design technique due to its inherent ability to generate the optimal full-state feedback controller for specific weightings of the input and output responses of the system. While this technique predicts high attenuation, the low gains associated with the resulting compensators were ineffective when implemented on the experimental system.

Due to the difficulty with implementing LQR experimentally, our focus shifted to PPF design techniques since gain selection is performed manually in this method. Also providing a less complicated form of the compensator, PPF techniques facilitate control design from experimental results. While initial PPF designs relied on the analytical model of the previous chapter, this ability to adapt to experimental results offers the ability to extend the compensator design to geometries which vary from the conical enclosure of our model. The remainder of this chapter presents the theory behind each compensator design and their application to the conical bore model of equation 3.30. Some discussion is also presented concerning the expansion of PPF design to larger geometries which are not modeled completely as conical sections.

4.1 Design of a Linear Quadratic Regulator

The first compensator design investigated and implemented on the conical bore was developed using Linear Quadratic Regulator (LQR) techniques. Providing the ability to minimize system response and control voltages relative to specific weighting matrices, this method provides the optimal controller relative to these weighting matrices. This section outlines the theory behind LQR design and its application to the conical bore.

4.1.1 LQR controller design

As a standard technique in modern control design, Linear Quadratic Regulator techniques can be used to determine the optimal set of full-state feedback gains relative to specific weightings of the state response and control effort. Operating to minimize the cost function

$$\mathcal{J} = \int_0^\infty \mathrm{q(t)^T Q_1 q(t) + v(t)^T Q_2 v(t) dt}, \tag{4.1}$$

LQR uses the weighting matrices Q_1 and Q_2 to determine the relative importance of the state response and control effort respectively. Minimizing the mean square state response and the mean square control voltage, Q_1 and Q_2 are formed to specify which states are of most importance and how important the state response is relative to the required amount of control effort. The solution to this optimization problem has been thoroughly investigated and is found in most textbooks which address modern control (Friedland, 1986; Franklin, 1998). Using a Riccati solution to determine the optimal feedback gains K_{lqr}, most of the calculation has been automated into standard analysis programs such as Matlab. However, the designer is still required to select the form of the weighting matrices Q_1 and Q_2. For our application the state weighting matrix is chosen as the mean square pressure of the first five acoustic modes. Thus, Q_1 takes the form $H^T H$, where H is the output matrix of equation 3.30. As such, the cost function takes the form

$$\mathcal{J} = \int_0^\infty \mathrm{q(t)^T H_1^T H_1 q(t) + Q_2 v(t)^2 dt}, \tag{4.2}$$

where Q_2 is now the design parameter.

Choosing the form of Q_2, the full-state feedback gains K_{lqr} can be determined. For our design, the solution to the LQR analysis was combined with an estimator of the system to form the full compensator. Using pole placement techniques the estimator poles were chosen to be five times faster than the closed-loop poles of $F - GK_{lqr}$, where F and G are the state and input matrices of equation 3.30. Using a pole placement algorithm to place the estimator poles a vector of estimator gains L_{est} was determined.

Defining the final component of the compensator design with the estimator gains, the only part of our design that remains undetermined is the form of the external disturbance. Selecting a disturbance path that allows equal excitation of each pressure mode, an impulse function is used to apply uniform excitation of the modal states. Combining this external disturbance with the open-loop state equation 3.30 and the LQR based controller, the set of closed-loop state equations can be represented by the following matrices

$$F_{cl} = \begin{bmatrix} F & -GK_{lqr} \\ L_{est}H & F - GK_{lqr} - L_{est}H \end{bmatrix} \quad G_{cl} = \begin{bmatrix} G_d \\ 0 \end{bmatrix}$$

$$. \qquad (4.3)$$

$$H_{cl} = \begin{bmatrix} H & 0 \\ 0 & -K_{lqr} \end{bmatrix} \qquad J_{cl} = 0$$

Where H_{cl} is chosen to yield both the state response $Hq(t)$ and the control effort $K_{lqr}q_{est}(t)$.

4.1.2 Optimization and Simulation of LQR

Providing the optimal full-state feedback gains for a specific system, LQR limits its optimization to one set of weighting matrices. The design process can be further refined by considering the state and control responses as these weighting matrices are changed. Having chosen the state weighting matrix Q_1 to be of the form H^TH, the control weighting matrix can be varied for further optimization of the compensator. Using an impulse function to represent broadband acoustic excitation, the average mean square pressure and average mean square voltage are calculated at the speaker face for a range of Q_2.

Creating a Matlab program (Appendix E) to increment through a wide range of Q_2 values, the impulse response corresponding to each solution was generated, given a peak excitation of 5 kPa. Calculating the root mean square pressure and root mean square control voltage of these impulse responses over a time scale of 0 to 2 seconds, Q_2 values were varied between 10^{-2} and 10^6. Collecting the resultant RMS values for pressure and voltage, a plot of P_{rms} versus CV_{rms} yields the LQR curve of Figure 4.1. This curve illustrates the trends observed by Boyd (1997) and Leo (1995) where improved performance in system response

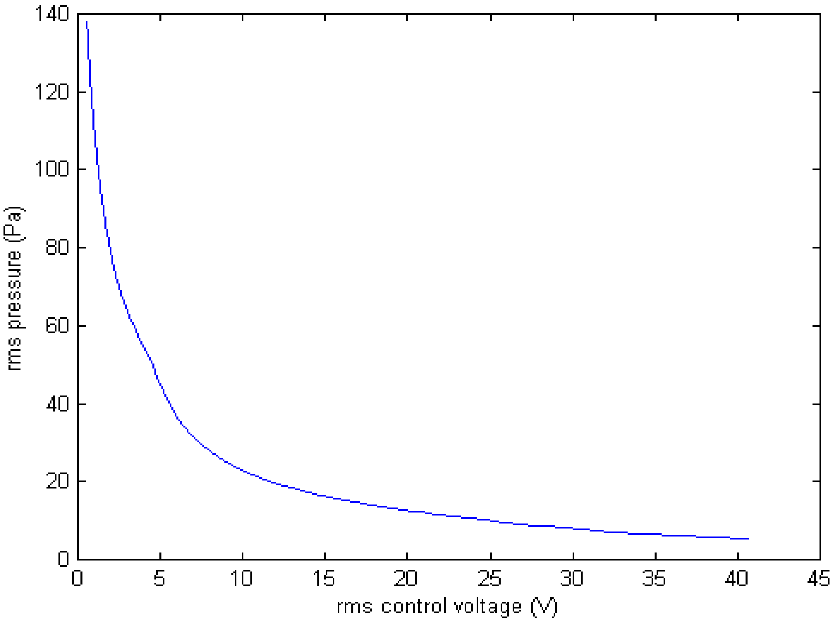

Figure 4.1: Trade-off curve from Linear Quadratic Regulator design.

corresponds to increased levels of control voltage. As observed by both Boyd and Leo, there arises a 'knee' within the plot which corresponds to the optimal ratio of input and state weighting matrices. Beyond this 'knee' in Figure 4.1 increased levels of pressure reduction rely on steadily increasing levels of control voltages. Thus the trade off between pressure and control voltage becomes less and less effective, indicating that the 'knee' is an optimal operating point.

While the curve in Figure 4.1 provides a visualization of the pressure to voltage relationship as the magnitude of the input weighting matrix increases, variation in actuator parameters would allow for a set of these curves to be generated. From this collection of curves it would be possible to tune the actuator resonance in order to improve the coupling between the actuator and the acoustic cavity. Each LQR curve within Figure 4.2 corresponds to a different actuator having a resonance frequency between 35 Hz and 235 Hz. Spanning both the first and second acoustic resonance, we chose this frequency band to test our theory concerning the controllability of acoustic modes as a function of actuator frequency. Inclusion of an actuating boundary within our system establishes a coupling effect between the piston resonance and one of the acoustic modes. As these two frequencies coalesce the effectiveness of the actuator increases dramatically. In terms of the

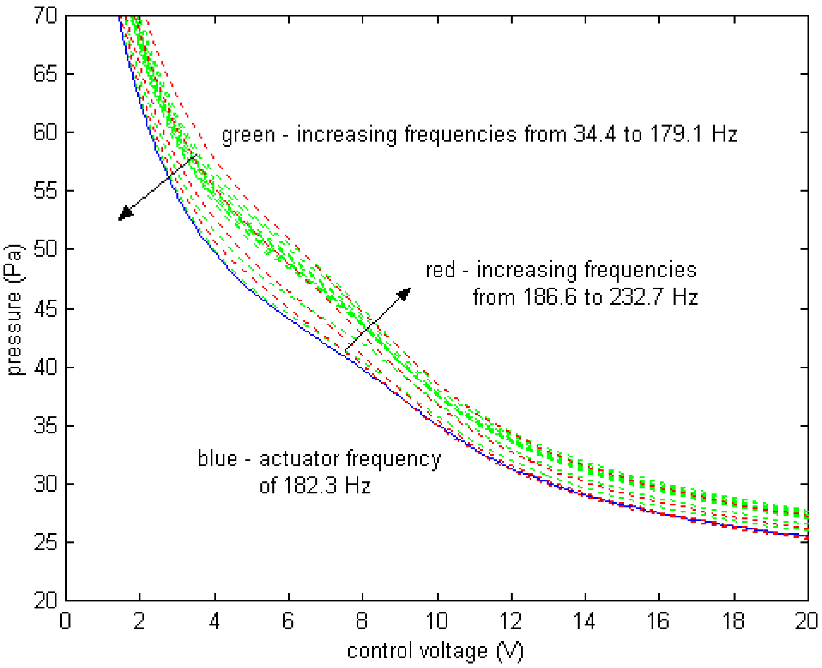

Figure 4.2: RMS pressure versus RMS control voltage for multiple actuator resonances, each as a function of Q_2.

LQR curve, the same control voltage would result in greater reductions in pressure for the actuator with greater coupling. In order to test this theory, we therefore chose a frequency band which spans at least two acoustic resonances so that this trend could be captured.

Holding the piston mass to 18.38 g, this range in frequencies was obtained by varying the mechanical stiffness from 851.8 $\frac{\mathrm{N}}{\mathrm{m}}$ to 39251.8 $\frac{\mathrm{N}}{\mathrm{m}}$. One other advantage of the LQR study is that it provides a means of comparing the degree to which the actuator couples with the cavity. As indicated in Figure 4.2, the LQR curve shifts towards the origin for increasing frequencies from 34.4 to 182.2 Hz. Beyond 182.2 Hz these curves reverse and begin shifting further away from the origin. As the axes correspond to RMS pressure within the cavity and RMS control voltage, the desire is to minimize each response for optimal performance. Therefore, by shifting the LQR curve toward the origin it can be surmised that coupling between actuator and cavity is steadily increasing. We would expect that this increased coupling would be good up to a certain actuator resonance, beyond which the coupling would diminish. Figure 4.2 illustrates this concept as the actuator resonance of 182.2 Hz corresponds to the LQR curve closest to the origin. One factor associated with this study is that while one actuator resonance may minimize the overall area under the corresponding

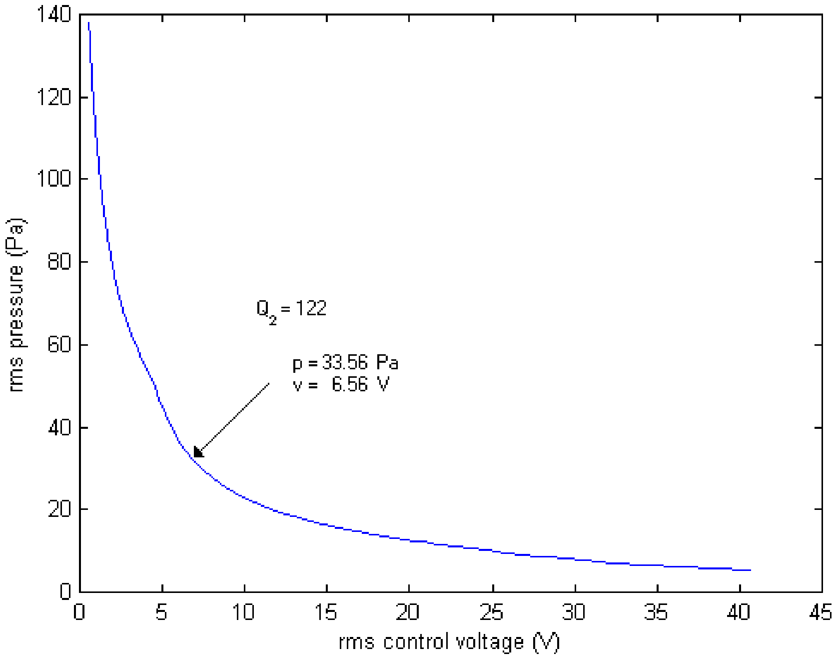

Figure 4.3: RMS pressure versus RMS control voltage, each as a function of Q_2.

LQR curve, at certain control voltages it might not provide the best performance. This can be seen in Figure 4.2 for control voltages of 9.2 V_{rms} and higher. For control voltages greater than 9.2 V_{rms} an actuator having a mechanical resonance of 186.6 Hz would actually be optimal. Thus, if restrictions are placed on the amount of available power a set of LQR curves would be necessary to determine the optimal actuator for a specific range of control voltages.

For simulation purposes, actuator parameters were chosen to correspond with the speaker used for experimentation, one having a resonance frequency of 34.4 Hz. Therefore, the trade off curve of Figure 4.3 was used for controller design. Within this curve the ‘knee’ is seen to exist at the designated point, corresponding to a weighting factor of $Q_2 = 122$. At this location pressure reductions of 75.6 % were predicted, requiring RMS control voltages of 6.56 V. Using the results of this LQR study, simulation of both open and closed-loop performance of the system were conducted. Considering the observer system used to develop the closed-loop system representation of equation 4.3, the compensator takes the form,

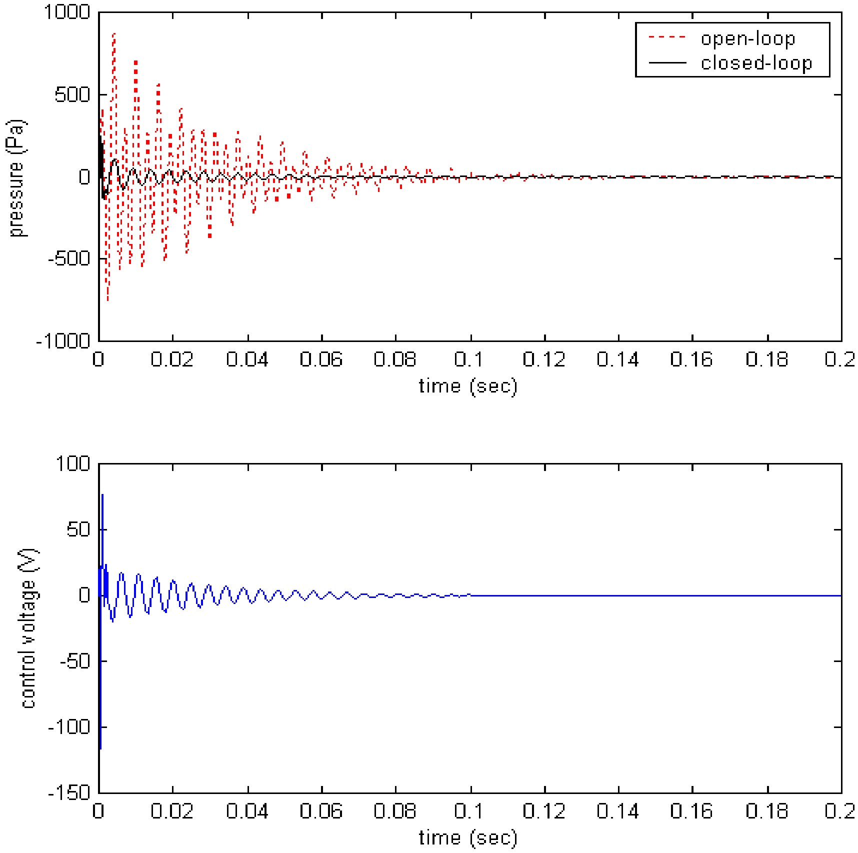

Figure 4.4: Impulse response (Q_2 = 122). a.) Open versus closed-loop pressure response b.) Control voltage

$$\begin{array}{ll} F_{comp} = F - GK_{lqr} - L_{est}H & G_{comp} = L_{est} \\ H_{comp} = -K_{lqr} & J_{comp} = 0 \end{array} . \tag{4.4}$$

Using the control weighting factor of 122, as shown in Figure 4.3, the corresponding LQR and estimator gains were calculated and the continuous form of the compensator was developed according to equation 4.4. Using a Tustin transformation, the discrete form of this compensator was then developed and applied to the coupled system model of equation 3.30. Simulating the impulse response of both the open and the closed-loop the system response is presented in Figure 4.4. Settling time reductions of 30%, from 0.20 seconds to 0.14 seconds were predicted, with maximum control voltages reaching levels of 116 volts. Figure 4.4b presents the required control effort for closed-loop performance.

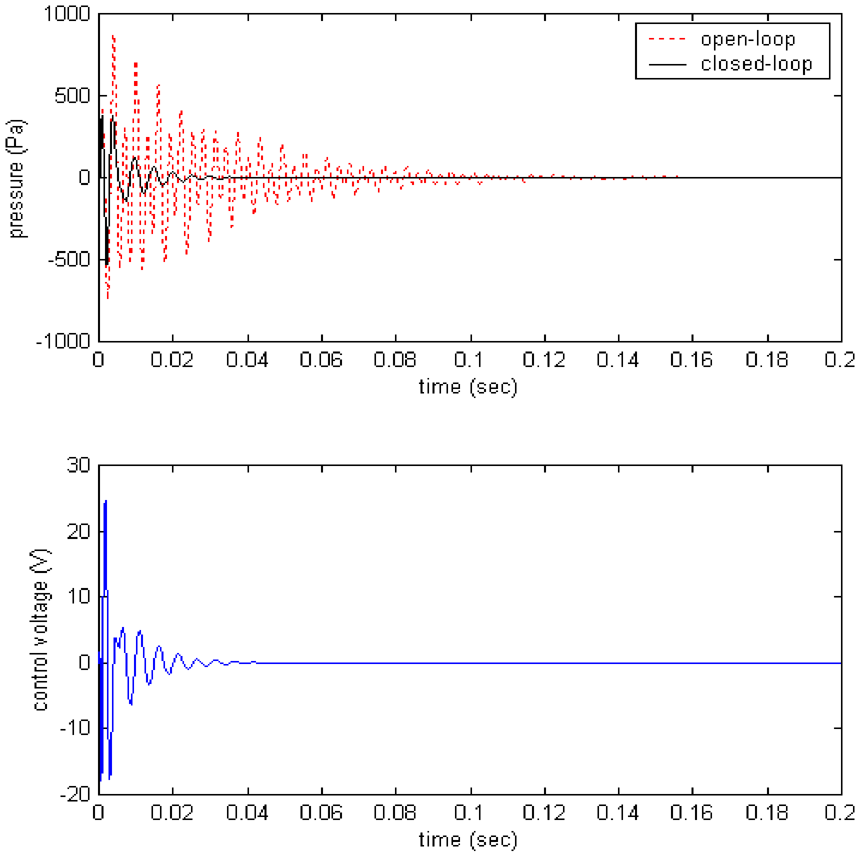

Figure 4.5: Impulse response ($Q_2 = 3500$). a.) Open versus closed-loop pressure response b.) Control voltage

Considering the physical limitations of the actuators at our disposal, such voltage levels are unattainable, requiring that we choose an operating point where lower control voltages are necessary. Selecting a control weight of $Q_2 = 3500$ reduces the maximum control voltage to 25.4 V with RMS pressure reductions of 48.5%. Figure 4.5 presents these pressure and voltage responses of this system to an impulse excitation.

While each of these compensator designs predicts large attenuation in the pressure level, one deficiency is in the DC gain associated with the open loop system. Figure 4.6 presents the frequency response of the open-loop system corresponding to the second compensator design. With a DC gain of -50 dB, implementation of this compensator barely clears the noise level of the measurement equipment. Examining the open and closed loop pole locations of this system, it is seen that the LQR compensator offers very little move-

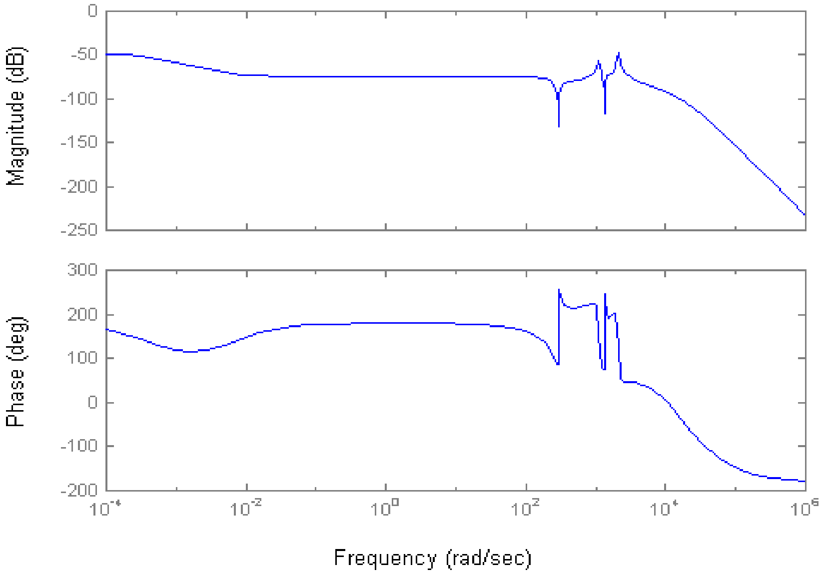

Figure 4.6: Frequency response of the open-loop system having an LQR based compensator ($Q_2 = 3500$).

ment in the closed-loop poles. Looking at the full-state feedback gains from the LQR compensated system shows that the maximum gain in the gain vector K_{lqr} was on the order of 393.7. Therefore, other compensator design techniques were investigated, allowing for greater control over gain selection thus motivating our investigation of Positive Position Feedback techniques.

4.2 Design using Positive Position Feedback

Designed to target individual modes, Positive Position Feedback typically uses displacement measurements to accomplish feedback control. With a fairly straightforward design approach, PPF techniques offer stable compensator designs which can be implemented almost directly from experimental results. Due to the nature of our system, pressure is positively measured by the compensator and is positively fed back to the system, essentially absorbing the acoustic energy within the cavity.

4.2.1 PPF controller design

Relying on two equations, one describing the cavity and the other describing the compensator,

$$\begin{aligned} \textit{cavity} &: \quad \ddot{\xi} + 2\zeta\omega\dot{\xi} + \omega^2\xi = g\omega^2\eta && (4.5) \\ \textit{compensator} &: \quad \ddot{\eta} + 2\zeta_f\omega_f\dot{\eta} + \omega_f^2\eta = \omega_f^2\xi, && (4.6) \end{aligned}$$

the output displacement or pressure feeds directly and positively into the other. Maintaining that the gain factor g must be positive we ensure that the modal coordinate ξ remains positive as it is fed into the compensator equation. In this arrangement the designer has three design parameters, ω_f, ζ_f and g. However, some limitations are placed on the filter's natural frequency. In order to perform properly ω_f must be chosen near the corresponding resonance of the cavity. Studies have been conducted to determine the optimal placement of this filter resonance. McEver (1999) proposed a method for determining the optimal placement as a function of pole/zero spacing and compensator gain. Following the method proposed by McEver a filter frequency of $\omega_f = \sqrt{2}\omega$ was chosen and used throughout our compensator design.

Due to limitations in our measurement equipment, the first resonance falls below the operating range of our experimental setup. Therefore our design procedure focused primarily on the second through the forth resonance of the cavity, located at 175 Hz, 313 Hz and 456 Hz. The remaining parameters ζ_f and g were determined iteratively. Beginning with relatively moderate damping ratios of 5% to 10% our analysis found that values on the order of 20% worked well within the conical bore for each of the three targeted modes. Similarly, gain selection was determined through an iterative process. As multiple filters were involved in the compensator design, high frequency gains can have an adverse effect on the stability of low frequency dynamics. DeGuilio (2000) encountered similar stability issues and therefore adopted a top-down gain selection approach.

Considering the block diagram of Figure 4.7, this top-down approach begins with the highest frequency filter design. Setting the gain coefficients g_{175} and g_{313} to zero, we determined the gain factor g_{456} through simulation. After setting this value, g_{313} was allowed to vary and was also set through simulation. Then, as with g_{456} and g_{313} the gain factor g_{175} was tuned iteratively to generate a stable PPF compensator. Placing the block diagram in state-space form, the compensator becomes

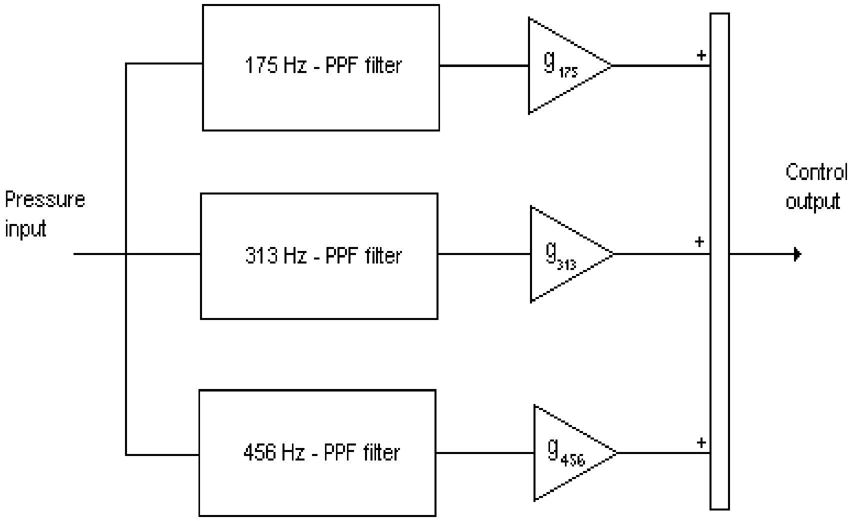

Figure 4.7: Three mode PPF controller.

$$
\begin{aligned}
\begin{Bmatrix} \dot{\eta}_1 \\ \ddot{\eta}_1 \\ \vdots \\ \dot{\eta}_n \\ \ddot{\eta}_n \end{Bmatrix} &= \begin{bmatrix} \begin{bmatrix} 0 & 1 \\ -\omega_{f_1} & -2\zeta_{f_1}\omega_{f_1} \end{bmatrix} & ... & 0 \\ \vdots & \ddots & \vdots \\ 0 & ... & \begin{bmatrix} 0 & 1 \\ -\omega_{f_n} & -2\zeta_{f_n}\omega_{f_n} \end{bmatrix} \end{bmatrix} \begin{Bmatrix} \eta_1 \\ \dot{\eta}_1 \\ \vdots \\ \eta_n \\ \dot{\eta}_n \end{Bmatrix} + \begin{bmatrix} 0 \\ \omega_{f_1} \\ \vdots \\ 0 \\ \omega_{f_n} \end{bmatrix} \xi \\
y &= \begin{bmatrix} g_1 & 0 & ... & g_n & 0 \end{bmatrix} \begin{Bmatrix} \eta_2 \\ \dot{\eta}_2 \\ \vdots \\ \eta_4 \\ \dot{\eta}_4 \end{Bmatrix}
\end{aligned}
\tag{4.7}
$$

4.2.2 Simulation of PPF

As stated in the previous section, gain selection for the PPF controller was determined iteratively through simulation. Initial gain selection was used to develop stable compensators that could yield appreciable reductions in closed-loop. Upon determining a suitable set of gains found in Table 4.1, minor adjustments were made to the damping ratios to

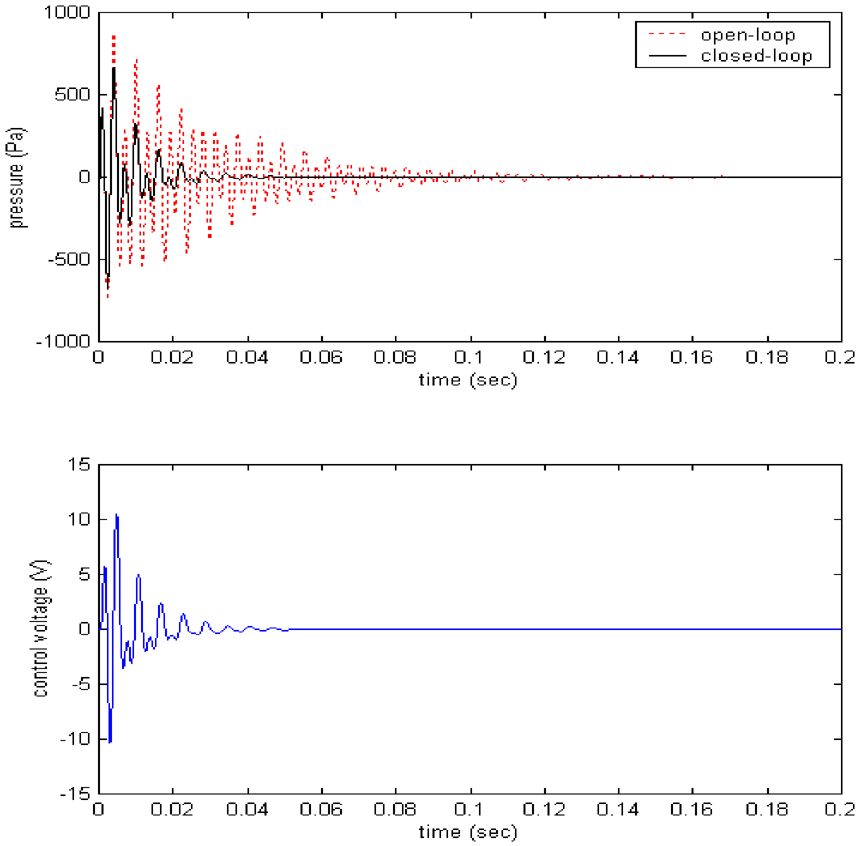

Figure 4.8: Impulse response with PPF filter. a.) Open versus closed-loop pressure response b.) Control voltage

further improve the system response. Figure 4.8 presents the pressure response and control effort associated with an impulse excitation of the pressure within the cone. It is seen that settling time improves dramatically with PPF control, with peak control efforts below 10.5 V. Producing high levels of attenuation with reasonable control voltages, the overall performance has not been fully optimized, as can be seen through comparison with the LQR compensator.

4.3 Comparison of LQR and PPF Simulations

Comparing closed-loop performance using PPF filters versus that of LQR based controllers, it can be seen that overall performance is slightly better with LQR control. Figure 4.9 presents the closed-loop system response of each system along with their corresponding

Table 4.1: Design parameters of the PPF compensator

Freq	ω_{plant} (Hz)	ζ_{plant} (%)	ω_{filter} (Hz)	ζ_{filter} (%)	gain factor
f_1	39.4	0.05	N/A	N/A	N/A
f_2	175.1	0.05	247.6	20.0	1000
f_3	314.4	0.05	444.6	20.0	20000
f_4	457.8	0.05	647.4	20.0	60000

control voltages. Comparing the system response using PPF and LQR control, it can be seen that the chosen PPF compensator does not accomplish the same levels of attenuation in pressure as does LQR control. This conclusion would be anticipated as LQR techniques are supposed to yield the ‘optimal’ controller given a set of state and control weighting matrices.

However, upon comparison of the control voltages required to achieve their respective levels of acoustic attenuation, the PPF compensator is seen to require less voltage than does the LQR controller. Comparing the mean squared pressure and the mean squared control voltage, the system with PPF compensation operated with 53.2 % higher mean squared pressures in the closed-loop response. Conversely, the required mean squared control voltage was 43.8 % less for the PPF compensator than for the LQR compensator. Comparison of the operating points on the LQR trade-off curve of Figure 4.10 shows that the PPF results lie above those predicted by the LQR curve. Increasing PPF gains would drive this operating point closer to the LQR curve, unfortunately instabilities arise in the discrete form of these compensators as these gains are increased too much. Actual implementation of the PPF controller does allow for some increase in the applied gain prior to instability. This allowable increase is the result of damping that was unaccounted for in the modeling process, making the system more robust to gain variations. The experimental results of this compensator along with those of the slightly augmented PPF designs are presented in the following chapter.

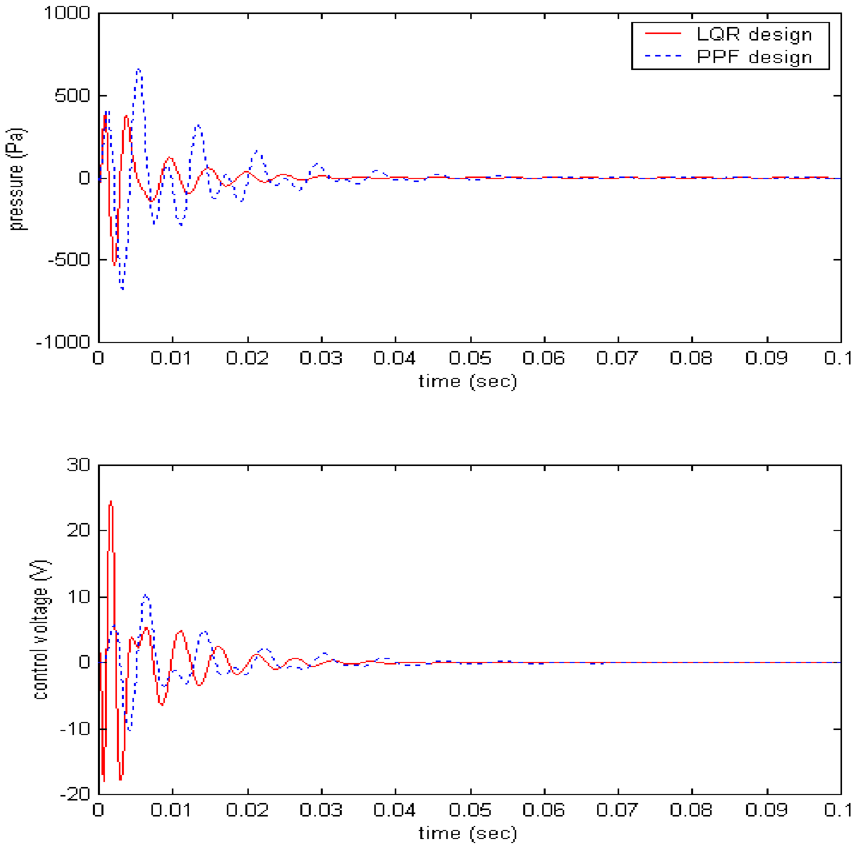

Figure 4.9: Comparison of closed-loop performance between LQR and PPF compensators given an impulse excitation. a.) Pressure response b.) Control voltage

4.4 Chapter Summary

In this chapter the design process used to develop and simulate feedback control has been presented. Starting with an investigation into LQR control, variations in the ratio of state and input weighting matrices were used to develop a trade-off curve relating root mean square pressure with root mean square control voltage. Also allowing actuator resonance to vary a set of these trade-off curves were developed which illustrate the coupling between actuator and acoustic resonance. This study showed that the coupling between actuator and cavity which can be used to optimize the actuator selection for a given geometry of the enclosure. Simulations with this technique indicate suitable performance, however an investigation into pole locations indicates that the full-state feedback gains move the

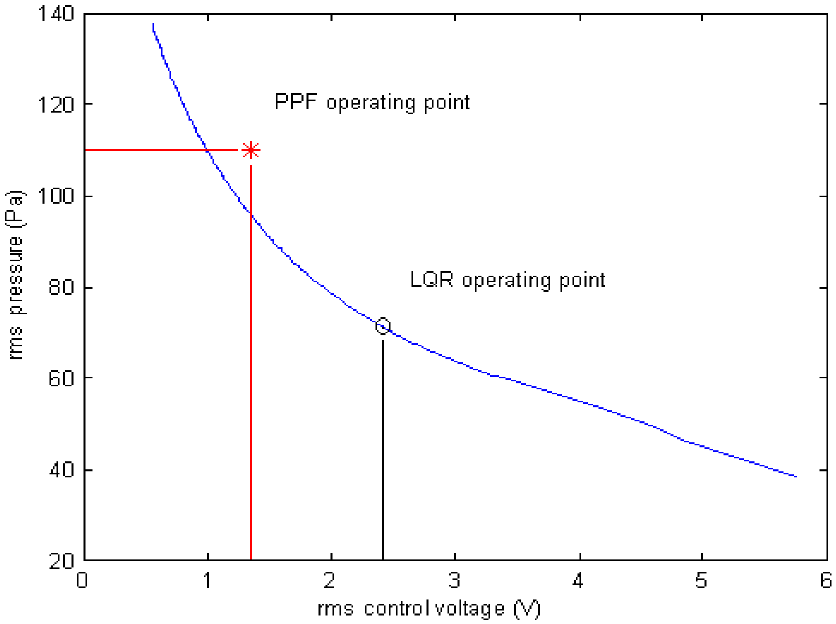

Figure 4.10: Comparison of operating points of LQR and PPF simulations.

system poles minimally. With feedback gains of 393.7 the DC gain of the open loop system is extremely low. Due to this, an investigation of PPF control was conducted. With simulated performance near to that of the LQR compensator, PPF allows for gain selection which is beneficial in the actual implementation of this controller in experimentation. The advantages of this controller are shown in the following chapter where experimental results from the physical application of these controllers is presented.

Chapter 5

Experimental Verification

Model results following each stage of the design process were compared to experimentally obtained data. Basing all of the numerical simulations on the geometric, mechanical and electrical parameters of an experimental test-bed, comparisons of both modal and impedance based models were conducted. Open-loop simulations were performed on the coupled state-space model to ensure that the electrical dynamics were properly coupled with the cavity model. This chapter begins with an overview of the experimental setup and the equipment used for data collection and control implementation. Section 5.2 presents a comparison between the experimentally obtained transfer functions of the physical system with those of both the modal and impedance based models. With relatively high levels of accuracy between each of these models and the corresponding experimental data, PPF control was implemented, the results of which can be found in section 5.3. With the favorable results of applying PPF techniques to a conical bore, along with the simplicity of the controller design itself, application to a sub-scale model of a Minotaur class fairing was conducted. These results are presented in section 5.4.

5.1 Experimental Setup

Experimental validation and implementation of the modal and impedance models of Chapters 2 and 3 were applied to the test-bed shown in Figure 5.1. In this figure it can be seen that two separate configurations were investigated. Figure 5.1a represents an enclosure having rigid terminations at both r_1 and r_2. Used primarily to validate the modal and impedance models with actuator mass and stiffnesses approaching ∞, the boundary

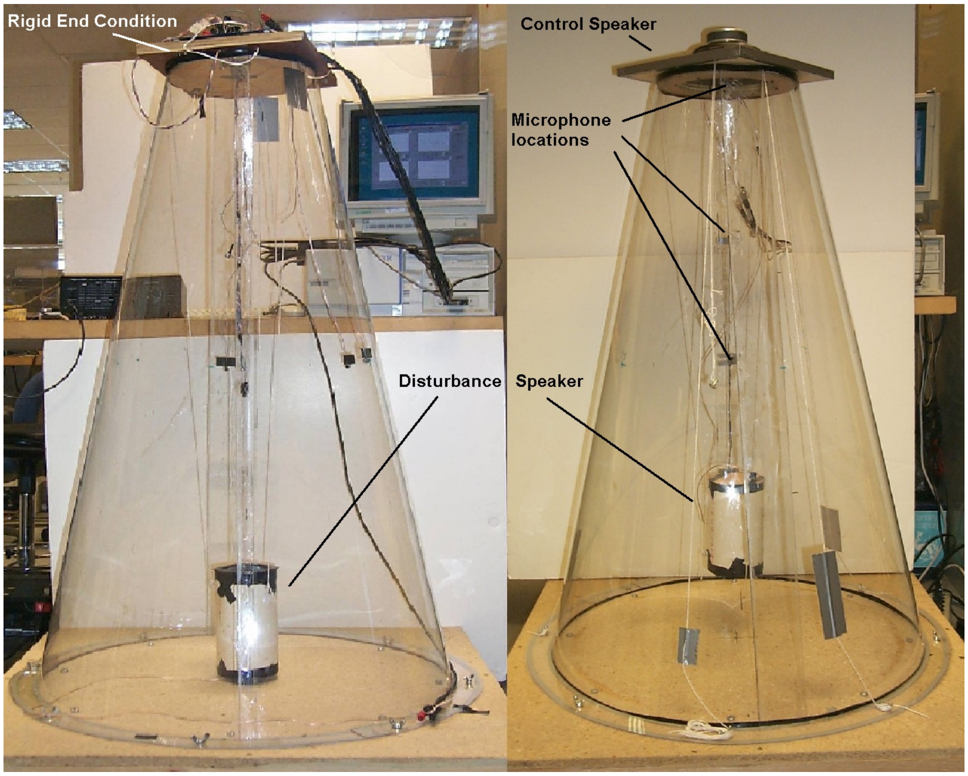

Figure 5.1: Experimental setup for conical bore validation and control. a.) rigid-rigid boundary conditions, b.) actuating-rigid boundary conditions

conditions were modeled using thick wooden terminations. Figure 5.1b shows the conical bore with an actuating boundary condition at r_1.

The conic section itself was fabricated from 1.5875 mm Lexan sheeting, having dimensions $r_1 = 0.63$ m and $r_2 = 1.79$ m. The rigid boundary condition at r_2 was constructed from a wooden platform that was bolted and sealed to the Lexan cone. The actuating boundary condition was constructed from an 8" polypropylene woofer (Radio shack 40-1024A) that was sealed to the cone at r_1. Stiffness, mass and area parameters used for simulation were based on technical specifications supplied with the speaker, as presented in Table 2.1. Pressure measurements were taken using an array of microphones (Radio Shack 270-090C) suspended along the inner wall of the cone at locations r_1, $\frac{(r_2-r_1)}{4}$, $\frac{(r_2-r_1)}{2}$,$\frac{3(r_2-r_1)}{4}$ and r_2. Conditioned through an RC circuit provided with the microphones, the output signals were captured and averaged for 40 samples using a Medallion Mobile FFT Analyzer manufactured by Zonic Corporation. Disturbance signals were generated using a 4" full range speaker (Radio Shack 40-1197) suspended within the cone. Positioned toward the rigid boundary at r_2, disturbance levels were measured and C-weighted through a sound pres-

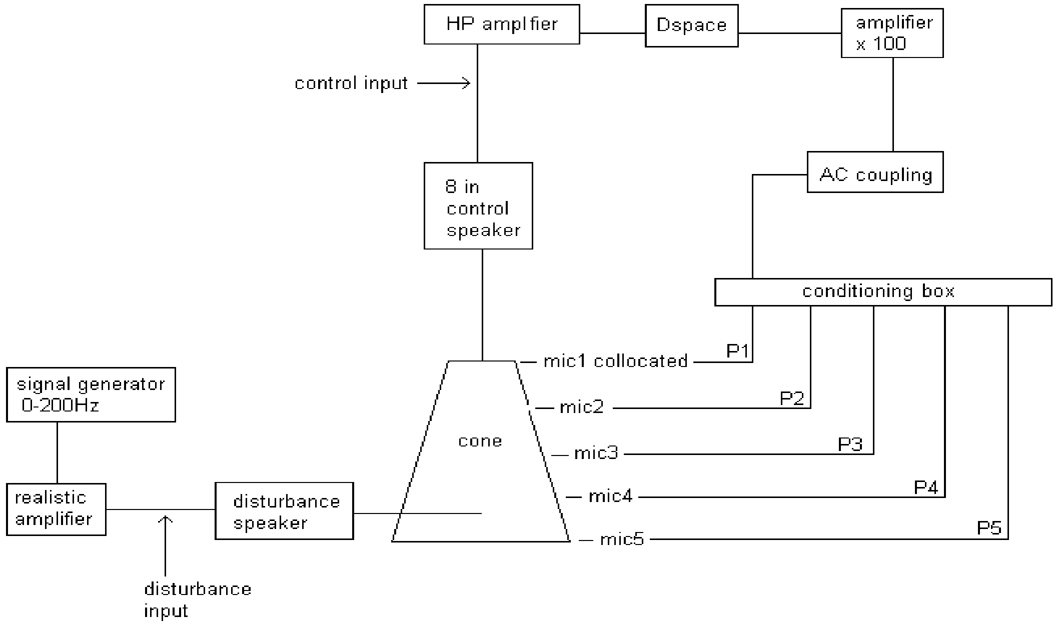

Figure 5.2: **Block diagram illustrating the experimental set-up.**

sure level meter (Radio Shack 33-2055). These levels were maintained at 100 dB throughout the testing procedure.

Control was applied using a DSP1102 board manufactured by dSPACE. Figure 5.2 presents a schematic of the equipment layout used in our control studies. Broadband disturbance signals were generated using the 4" full range speaker, with pressure measurements obtained using a microphone collocated with the control actuator at r_1. This signal was conditioned through the RC circuit provided by Radio Shack, with the DC component removed using an Ithaco filter (model 4302). The AC component of the microphone signal was then amplified by a factor of 100 (PCB model 482A16) before being fed into the dSPACE control board. Taking this amplification into account, the digital PPF compensator was then applied based on this input signal. Feeding the control voltage through an HP amplifier (model 6826A Bipolar Power Supply/Amplifier) with a gain factor of 1, the control signal was applied to the 8" polypropylene woofer mounted at r_1. For this study the pressure output of each microphone was also monitored using the Medallion Mobile FFT Analyzer to ensure global attenuation within the conical bore.

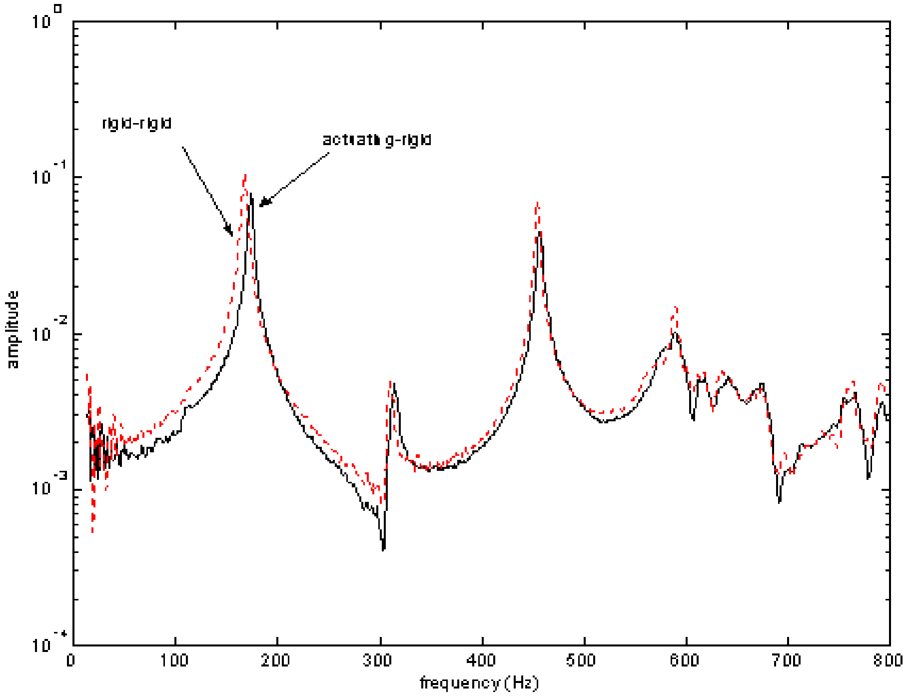

Figure 5.3: Experimentally obtained resonances for rigid-rigid and actuating-rigid boundary conditions.

5.2 Validation of Modal and Impedance-Based Models

As shown in Figure 5.1, two separate configurations were used to validate the modal and impedance models. Both internal and external disturbances were investigated to excite the system. Considering that the only resonances of interest in our study were the longitudinal acoustic modes, internal excitation was selected for capturing FRF data as this method does not excite structural modes to levels of excitation that are induced by an external source. Introducing a signal of random noise, the frequency response for both rigid-rigid and actuating-rigid configurations were captured.

5.2.1 Modal model

Figure 5.3 presents this frequency response data. It can be seen from this figure that natural frequencies of the system increase as the mass and stiffness of the actuating boundary decrease. From this plot, four of the first five natural frequencies are easily identifiable and their values, along with those predicted by our modal model are compiled in Table 5.1. Due

Table 5.1: Comparison of the resonance frequencies of our modal model with those of an experimental test stand for rigid-rigid and actuating-rigid boundary conditions (all frequencies in Hz).

	Rigid - Rigid			Actuating - Rigid		
Freq	Experiment	Modal model	Error	Experiment	Modal model	Error
f_1	-	1.1	-	-	38.4	-
f_2	168.0	161.9	3.63%	174.0	175.2	0.69%
f_3	310.0	303.5	2.10%	314.0	313.3	0.22%
f_4	454.0	448.5	1.21%	457.0	455.8	0.26%
f_5	589.0	594.7	0.97%	589.0	600.4	1.94%

to the operating range of the microphones (40 Hz to 4000 Hz), the first acoustic resonance of the test stand f_1 lies below the lower frequency limit of the sensors. Therefore, this resonance was indiscernible from the sensor noise for both rigid-rigid and actuating-rigid configurations. Comparing the second through the fifth natural frequencies of the cavity, correlation between predicted and experimental results was favorable. Considering rigid-rigid boundary conditions, the maximum error corresponds to a 3.63% discrepancy in the second acoustic resonance. The actuating-rigid boundary condition provides slightly lower levels of error, resulting in predictions within 1.94% of the experimental results.

While these errors indicate some slight discrepancies in the model, considering that our model has been validated against the pre-existing closed-closed model of Ayers *et al.*, it must be considered that other, unaccounted for phenomena are present in the experimental results. The development of our model assumes spherically shaped end conditions, such that any reflections radiate in and out along radial lines. Due to the size of the available test stand, construction of such end conditions was not practical, and were therefore approximated with wooden, plane terminations. In addition to introducing distortion in the angle of reflection, these end conditions also introduce a small degree of absorption. The presence of each of these sources of error would correspond to shifts in the acoustic resonance, accounting for most of the minor discrepancies between our predictions and the

Table 5.2: Comparison of the resonance frequencies of our impedance-based model with those of an experimental test stand for rigid-rigid and actuating-rigid boundary conditions (all frequencies in Hz).

	Rigid - Rigid			Actuating - Rigid		
Freq	Experiment	Impedance model	Error	Experiment	Impedance model	Error
f_1	-	0.15	-	-	38.4	-
f_2	168.0	162.0	3.57%	174.0	175.3	0.75%
f_3	310.0	303.6	2.06%	314.0	313.6	0.13%
f_4	454.0	448.6	1.19%	457.0	456.4	0.13%
f_5	589.0	594.8	0.98%	589.0	601.4	2.10%

experimental results.

5.2.2 Impedance-based model

Comparison between the experimental and impedance based model begins by analyzing the frequency response used to validate the modal model. Table 5.2 presents the resonance values predicted by the impedance model for both rigid-rigid and actuating-rigid configurations of the conical bore. As expected from the comparison between modal and impedance models of Chapter 3, similar discrepancies exist when relating the predictions of the impedance model with those of the experiment. And, as with the modal model, these discrepancies can be attributed to the physical end conditions applied in the experiment.

However, further analysis of this system can be conducted by considering the open-loop transfer function of the coupled system used to relate pressure output to voltage input. This coupled relationship from equation 3.30 includes not only the mechanical and acoustic dynamics, but also those associated with the electrical components of the speaker. Figure 5.4 gives a visual comparison of the actual and the predicted transfer functions of the system, relating pressure to disturbance voltages. Capturing the first four resonances, the dashed curve represents the experimentally obtained frequency response. Using the

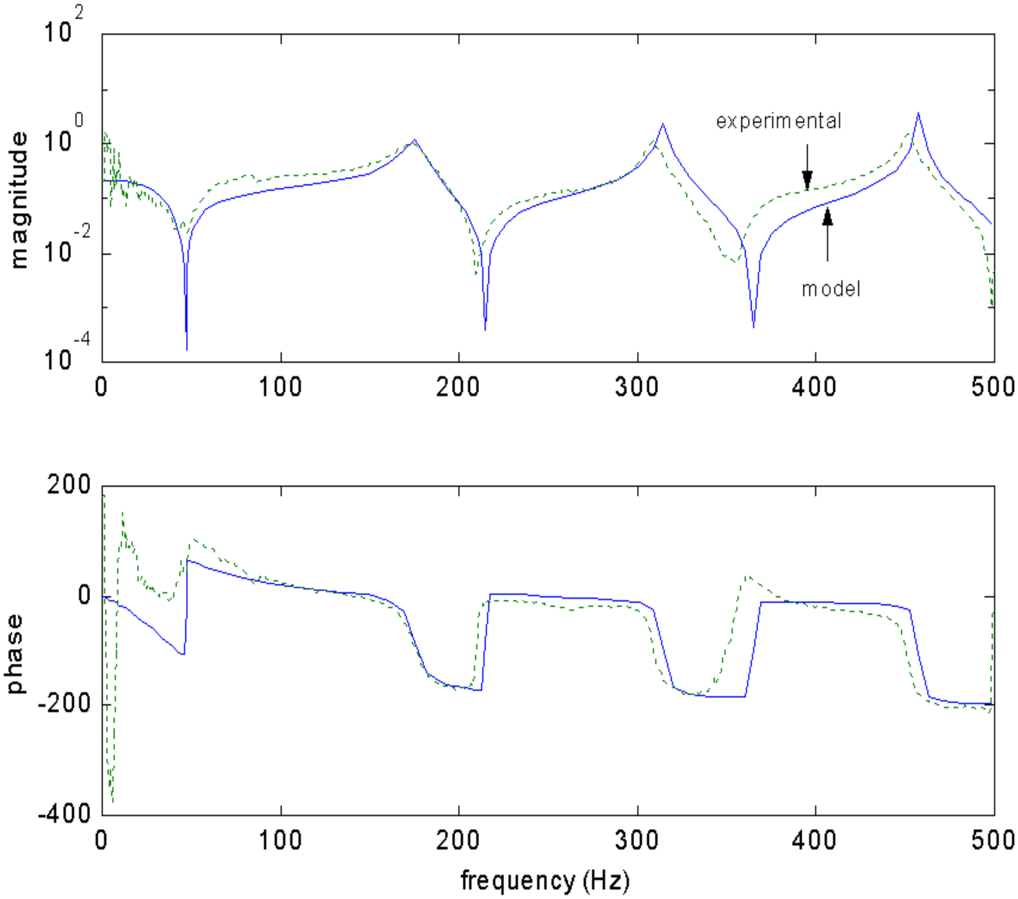

Figure 5.4: Open-loop comparison of experimentally obtained frequency response with that predicted by the impedance based model.

coupled state-space model of equation 3.30, the solid curve presents the predicted response of the system given 0.0005% damping in the acoustic poles and 0.05% damping in the acoustic zeros. Table 5.3 presents the experimentally determined and predicted resonance frequencies, as well as the error associated with the model. The first natural frequency is not included in this table because it falls below the operating range of the microphones used for data collection. However, comparison of the second through the fourth natural frequencies indicate good correlation between the model and the actual system.

Looking at the form of both magnitude and phase for both model and data, it is seen that the model predicts the overall trends of the system relatively well. The major discrepancies in this system are in the antiresonance of the system. This inaccuracy results from the fact that all of our modeling procedures assume a form of the disturbance path.

Table 5.3: Comparison of experimental and state-space model results (all values in Hz).

Freq	Experiment	Impedance model	Error
f_1	-	39.4	-
f_2	173.0	175.1	1.21%
f_3	309.0	314.4	1.75%
f_4	452.0	457.8	1.28%

In actual application of the fairing, acoustic resonances are generated by tremendous levels of structural vibration resulting from the firing of the booster rockets. These vibrations constitute the source of most of the disturbance levels introduced to the cavity as the deployment vehicle sits on the launch pad. Then as the rocket progresses through its launch, airflow along the outer walls contributes more and more to panel vibrations and the resulting acoustic resonances. Due to these variations in the disturbance source, replicating the disturbance using our test-stand would be difficult, if not impossible, with the equipment at hand. Therefore, the emphasis on modeling the disturbance source and path was kept as general as possible throughout the model development and application.

However, considering just the system poles, all of the predicted eigenvalues fall within 1.75% of the eigenvalues of the physical system. As these eigenvalues define the dynamics of the system it can be seen that the model effectively represents the coupled system. Because of this, the overall results of our control simulations were expected to be relevant to the experimentally implemented controllers.

5.3 Control of the Conical Bore

The first design approach applied to the conical bore used LQR techniques. Developing the optimal set of feedback gains as discussed in Chapter 4, a state observer was used in the development of a suitable compensator. Designing in the continuous domain the compensator of equation 4.4 was developed. Using a Tustin transformation to obtain the

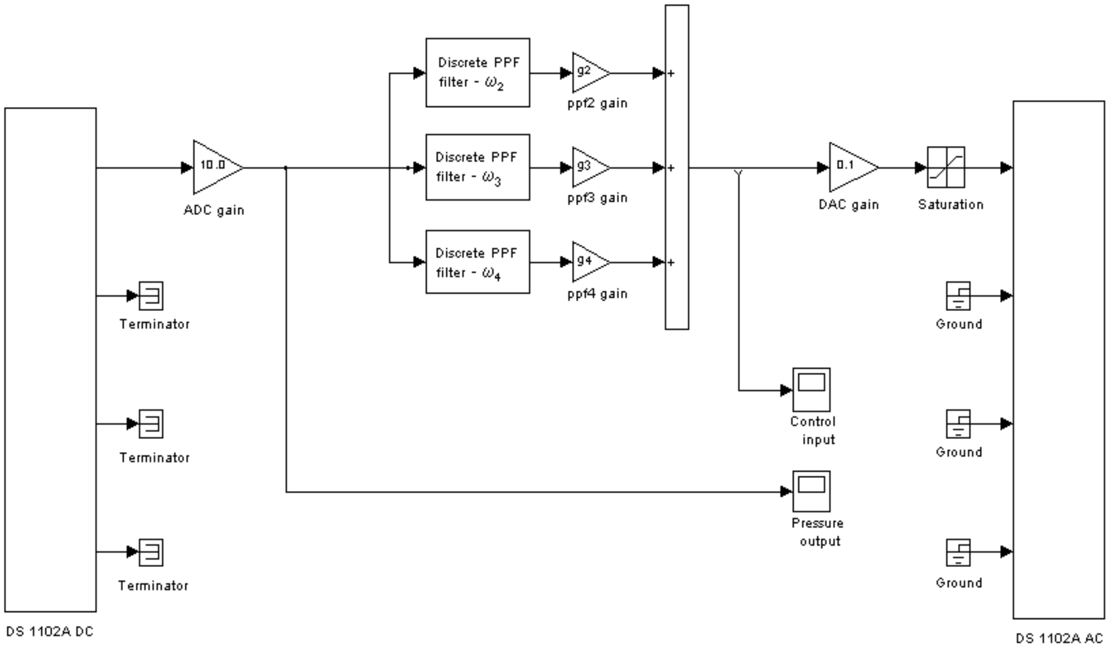

Figure 5.5: SIMULINK diagram of PPF compensator used by dSPACE to implement feedback control on the experimental test stand.

discrete form of the compensator, implementation of the controller was accomplished using a dSPACE system. Unfortunately no noticeable attenuation was observed in the noise levels of the system. Examining the location of open and closed loop poles of the system, it was seen that the ‘optimal’ placement assigned by the LQR algorithm did not move the system poles appreciably. With full-state feedback gains of only 393.7 or less, the compensated system varies only slightly from the initial plant. Due to the nature of these LQR design techniques, limited control over pole placement and gain selection led us to investigate the more classical type methods of PPF design.

Using the design methodology of the PPF section of Chapter 4, a multi-mode compensator was developed. Due to limitations in our sensing equipment, control could not be applied or monitored with any degree of accuracy for the first acoustic resonance. Falling below the operating range of our sensing microphones (Radio Shack 270-090C), our attentions focused instead upon the second through the forth resonance. Using an overestimation of the system’s natural frequencies in an effort to limit interaction between the poles of each mode, a damping ratio of 20% was applied to the compensator. Selecting gains using a top-down approach (DeGuilio, 2000), the compensator was formed using the parameters shown in table 4.1. Designed through simulation, implementation of the compensator was

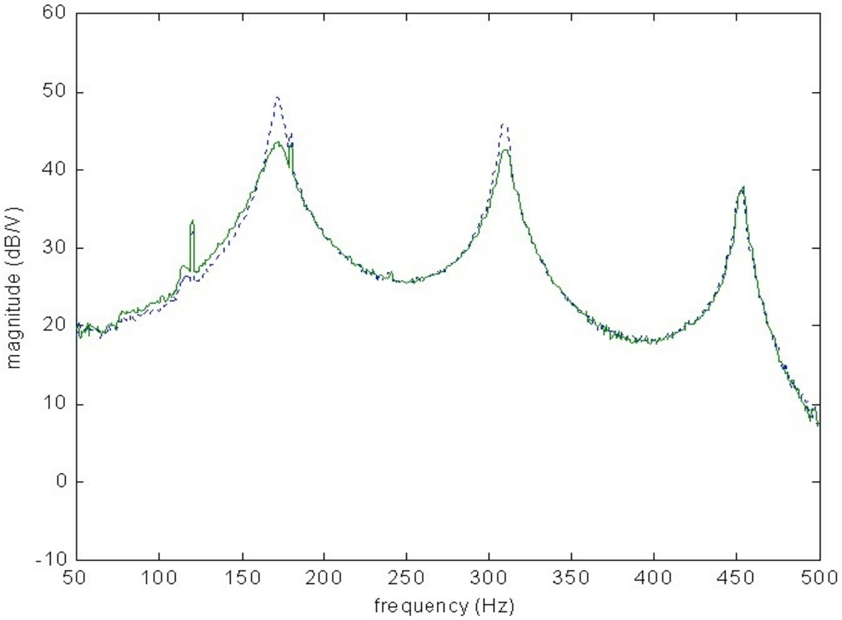

Figure 5.6: Open (dashed) versus closed (solid) performance for collocated sensor-actuator pair with PPF parameters of Table 4.1. This frequency response relates output pressure to disturbance signal.

accomplished through the discrete form of this controller. Using a Tustin transformation for each PPF filter, the total compensator of Figure 5.5 was constructed in SIMULINK.

Using ControlDesk software (version 1.1) to build the controller onto the DSP board, variable gains were applied to g_2, g_3 and g_4. Through the experimental procedure we found that the gains which were predicted to drive the simulation unstable actually underestimated those which drove the physical system unstable. Providing the ability to tune these gains during an experimental run allowed real-time optimization of the compensator. Running multiple iterations on this compensator, all of the parameters were varied to verify the design process used in our simulations. Testing the system for a variety of damping ratios, we found that ratios above 20% showed no appreciable improvement in system performance. Similarly, variations in the resonance frequency were also conducted. Setting ω_f equal to the plant natural frequency provides high levels of attenuation, but limits the gain magnitudes that can be applied to the compensator. Overestimations of the ω by factors of 1.2 to 1.414 were also implemented with only slightly higher levels of performance obtained using higher factors. Increasing beyond 1.414, compensator performance was seen to drop off rapidly. For each of the compensators discussed in the remainder of this section, the assigned values

Table 5.4: Design parameters of the PPF compensator

Freq	ω_{plant} (Hz)	ζ_{plant} (%)	ω_{filter} (Hz)	ζ_{filter} (%)	gain factor
f_1	39.4	0.05	N/A	N/A	N/A
f_2	175.1	0.05	247.6	20.0	5000
f_3	314.4	0.05	444.6	20.0	50000
f_4	457.8	0.05	647.4	20.0	200000

of ω_f and ζ_f were $\omega_f = \sqrt{2}\omega$ and $\zeta_f = 0.20$.

Applying the PPF parameters of Table 4.1 the open and closed loop responses of Figure 5.6 were obtained. Amplitude reductions of the second and third mode are evident in this figure. Providing increases in damping by factors of 2.09 and 1.47 in the second and third modes respectively, the forth mode appears to be unaffected by this compensation. This trend in reduction is also seen to be a global phenomena as shown in Figure 5.7. Monitoring the pressure levels at four separate, noncollocated positions throughout the cone, similar reductions in the second and third resonance were observed throughout the enclosure.

As stated before, the experimental system allowed for more gain variation prior to system instability than did the simulation. Taking this into consideration, the dSPACE model of the system was equipped such that the compensator gains could be varied real-time. Approaching the experiment with the same top-down approach used in design, gain variations were conducted while monitoring system performance to avoid instabilities. Arriving at the compensator parameters of Table 5.4, the open and closed loop performance of the system was captured. Figure 5.8 presents the frequency response for the collocated sensor-actuator set.

As with the first compensator, attenuations in the second and third resonances were evident. Increases of 3.51 and 2.53 times the open loop damping were found for the second and third modes, again with no appreciable reduction in the third mode. Control voltages associated with this compensator were also monitored. Shown in Figure 5.9, maximum control voltage never exceeded 200 mV throughout the testing period. Examining the

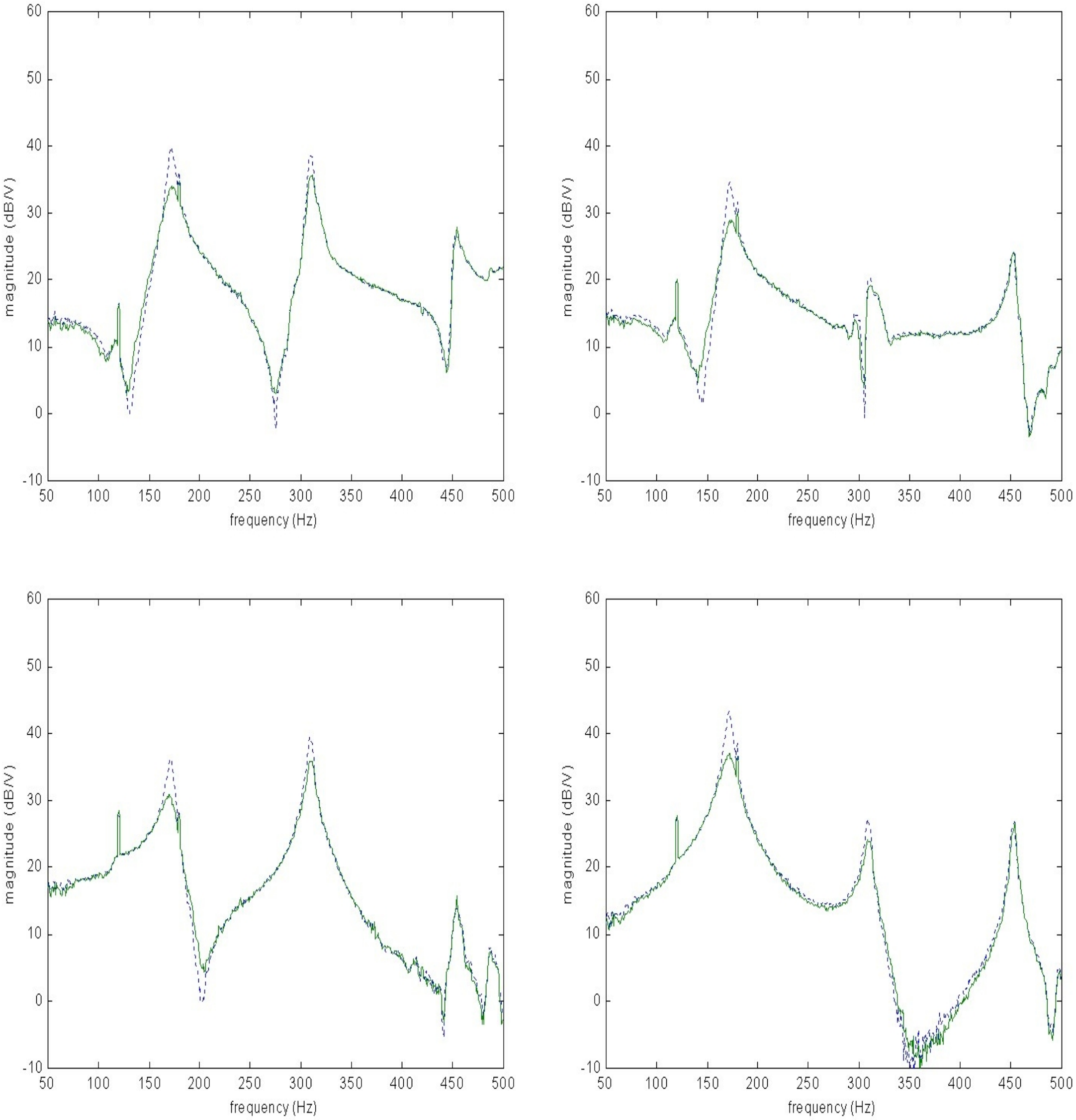

Figure 5.7: Global comparison of open-loop (dashed) and closed-loop (solid) performance with gain PPF parameters of Table 4.1. Frequency response throughout the conical bore relating output pressure to the disturbance signal: microphone at $\frac{(r_2-r_1)}{4}$ (top-left), microphone at $\frac{(r_2-r_1)}{2}$ (top-right), microphone at $\frac{3(r_2-r_1)}{4}$ (bottom-left) and microphone at r_2 (bottom-right).

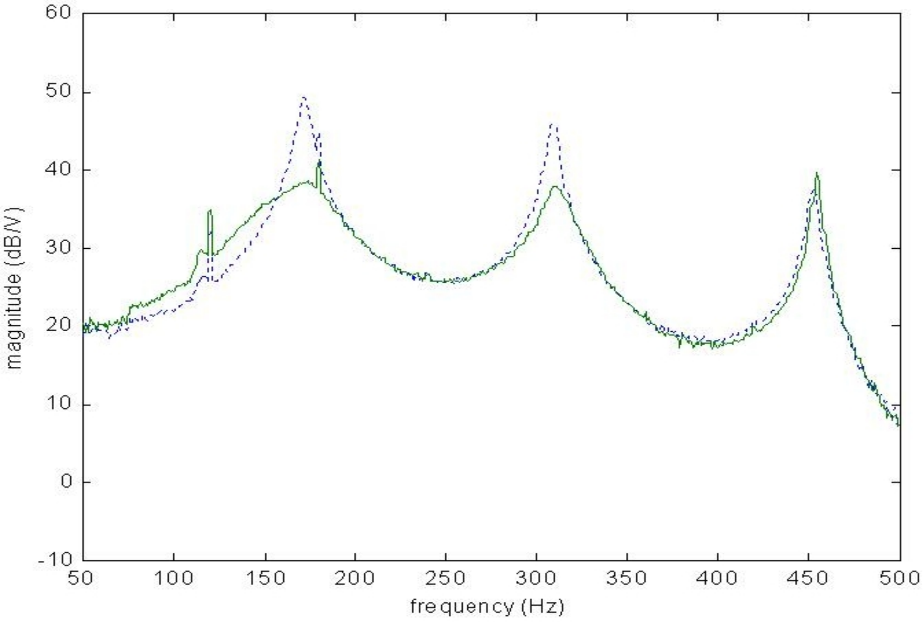

Figure 5.8: Open-loop (dashed) versus closed-loop (solid) performance for collocated sensor-actuator pair with PPF parameters of Table 5.4. This frequency response relates output pressure to disturbance signal.

global trend of this compensator it can be seen that attenuation was observed throughout the entire conical bore, as shown in Figure 5.10.

Quantifying the attenuation within the cone, Table 5.5 presents the pressure reduction at each microphone location. Focusing on a region of the frequency response which spans a 50 Hz to 400 Hz range, the root mean squared pressure was calculated

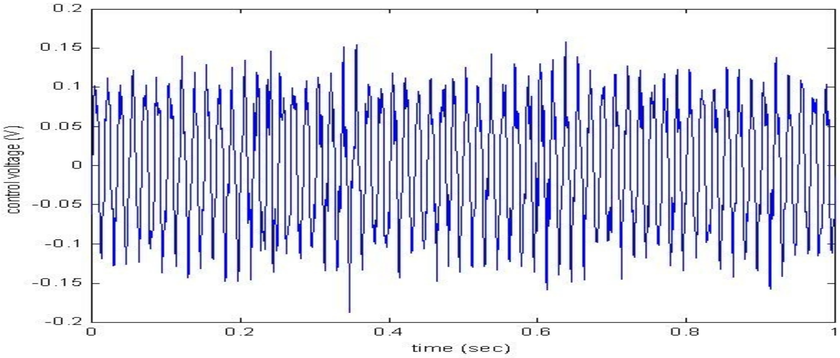

Figure 5.9: Required control voltage for PPF compensator of Table 5.4.

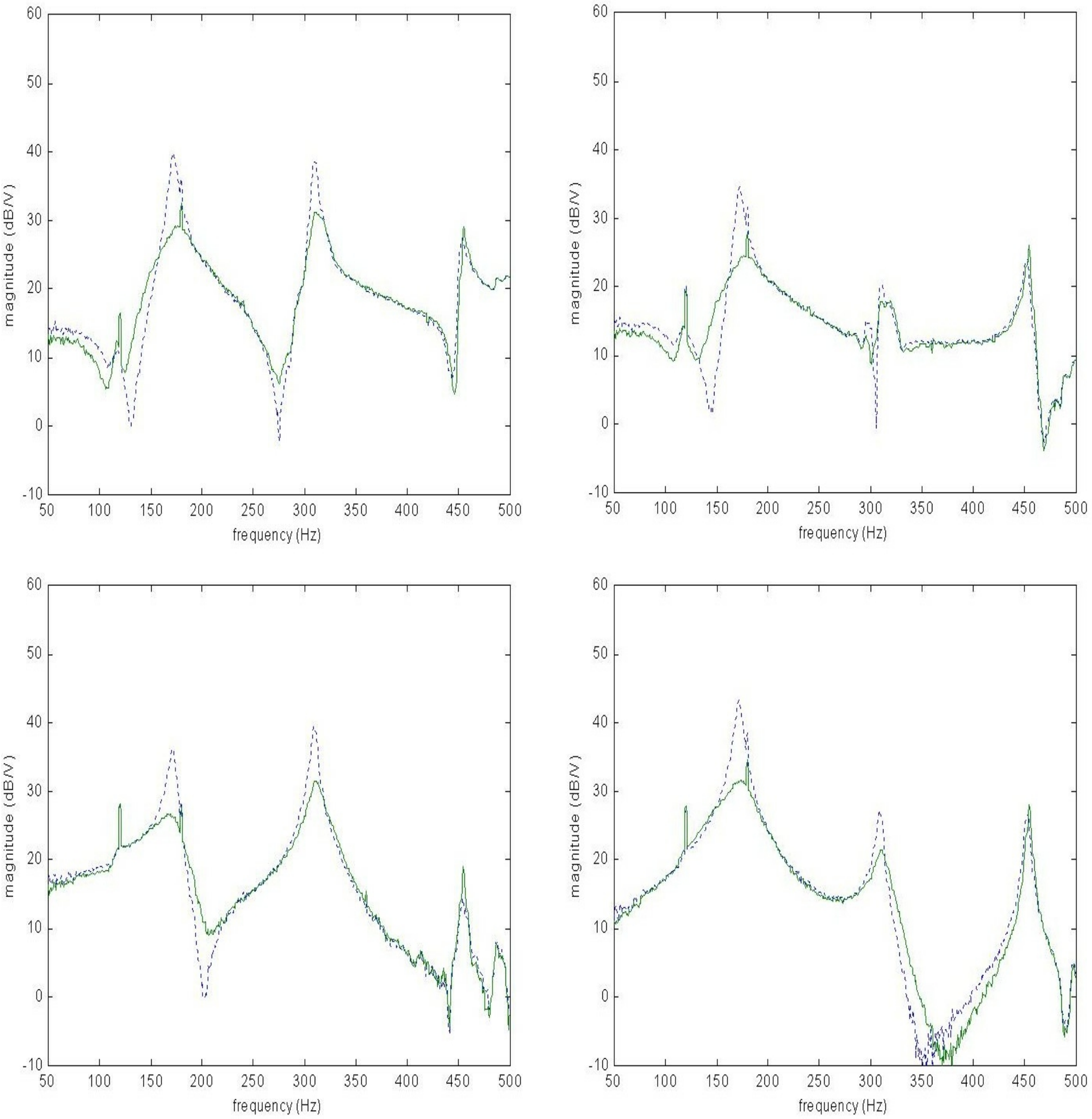

Figure 5.10: Global comparison of open (dashed) and closed (solid) loop performance with gain PPF parameters of Table 5.4. Frequency response throughout the conical bore relating pressure to disturbance: microphone at $\frac{(r_2-r_1)}{4}$ (top-left), microphone at $\frac{(r_2-r_1)}{2}$ (top-right), microphone at $\frac{3(r_2-r_1)}{4}$ (bottom-left) and microphone at r_2 (bottom-right).

Table 5.5: Pressure reductions in the conical bore test stand.

Microphone	Pressure reduction in %	Pressure reduction in dB
mic_1	39.1	4.31
mic_2	38.7	4.25
mic_3	32.1	3.37
mic_4	35.1	3.76
mic_5	47.2	5.55

$$P_{rms} = \sqrt{\frac{1}{f_h - f_l} \int_{f_l}^{f_h} P^2 df}. \tag{5.1}$$

Evaluating this for both open and closed loops, overall reduction was determined to be a ratio of the closed-loop to open-loop RMS pressures. With overall reductions of 38% it was of interest to see if the results could be extended to larger volumes constrained by different geometries. The next section presents our investigation into the application of PPF control on a more complex geometry that models a fairing of the Minotaur class.

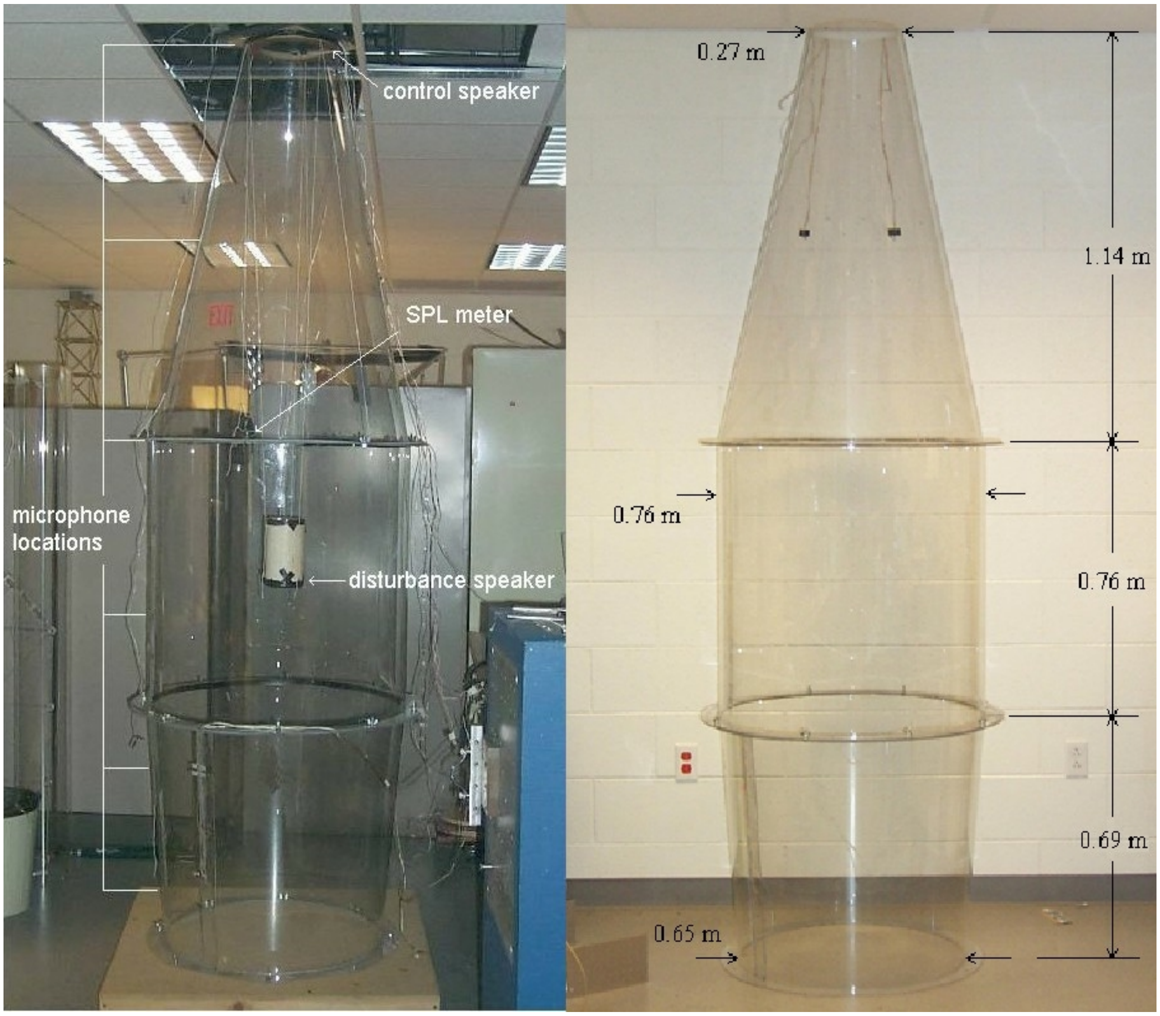

Figure 5.11: Geometric parameters of the Lexan payload fairing.

5.4 PPF Control Applied to the Full Fairing Geometry

With the favorable results of section 5.3, it was felt that the compensator design could be further extended to more complex geometries. Choosing a geometry more representative of a Minotaur class fairing, tests were conducted on the Lexan shroud of Figure 5.11. Constructed in three separate sections from 1.5875 mm Lexan sheeting, each section was bolted together and the joints were sealed using electrical tape. Using the conical bore of Figure 5.1 to construct the top section of the fairing, a cylindrical tube of diameter 0.76 m and length 0.76 m was used to comprise the middle section. The lower portion of the fairing was constructed from another conical shell with length 0.69 m and minor diameter 0.65 m. Within the shroud six different microphones were installed to monitor pressure

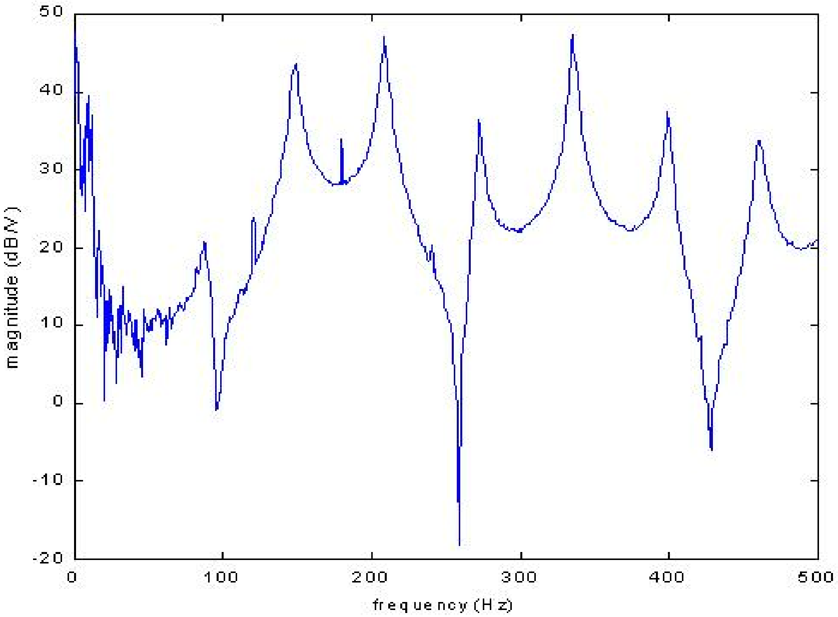

Figure 5.12: Open-loop transfer function of the Lexan fairing.

levels throughout the fairing. The disturbance speaker was positioned about mid-length within the shroud. The control actuator was mounted to the top of the fairing, again with a collocated sensor attached near the speaker face. Overall sound pressure levels are monitored and maintained using a SPL meter (Radio Shack model 33-2055) to ensure overall excitation of 100 dB.

With the conical bore of the previous section, the system dynamics were modeled and pole locations were known. However, that model does not extend fully to the geometry of Figure 5.11. By expanding to the full fairing geometry, the eigenvalues of the system are no longer known. Therefore, the first step in our design process was to compensate for this by determining the pole-zero locations within the shroud. Performing a frequency response on the system the resonance and antiresonance frequencies of the fairing were obtained. Shown in Figure 5.12, it can be seen that there are a greater number of low frequency resonances than were present with the conical bore.

Basing our design upon these experimentally obtained results, we first decided which frequencies we would target with the PPF filter. Designing around the resonance peaks at 149 Hz and 209 Hz, damping ratios of 20% were again applied. Following the same procedure for determining the filter frequencies, an overestimation factor of $\sqrt{2}$ was again

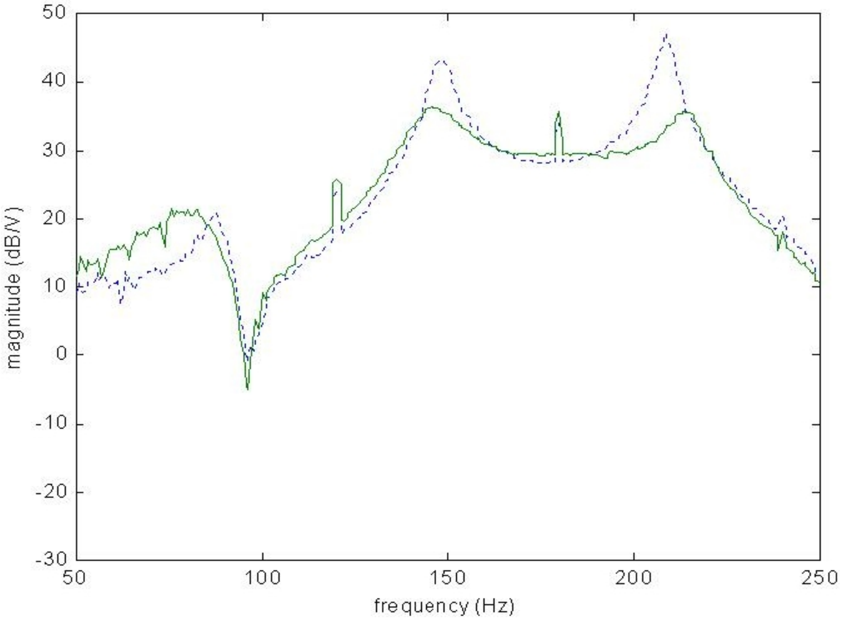

Figure 5.13: Open versus closed loop performance within the fairing for collocated microphone. This frequency response relates output pressure to disturbance signal.

used. Using the same SIMULINK program as Figure 5.5, only one modification was made which limited the number of applied filters from three to two compensators. With gain variation incorporated within the dSPACE program, real-time adjustments in gain were used to tune the closed loop performance. Implementing this approach on the actual fairing setup, frequency response data for both open and closed loop configurations were captured. Figure 5.13 presents this comparison for the collocated sensor-actuator pair. Again considering the global performance of this actuator, Figure 5.14 presents a comparison of open and closed loop frequency responses at specific locations within the shroud.

Examining the system quantitatively, the total amount of reduction within the system can be determined, Table 5.6. Limiting the frequency band of interest to a region from 50 Hz to 250 Hz, the mean squared pressure for both open and closed loop were calculated at each microphone location. The lower limit on this bandwidth was chosen to eliminate noise associated with the sensors, while the higher limit was selected as passive solutions become viable beyond these frequencies. Calculating the pressure reductions over this frequency range, overall reductions of 38.5% were seen. Table 5.6 presents the specific reduction levels associated with each microphone. Considering the overall control voltage

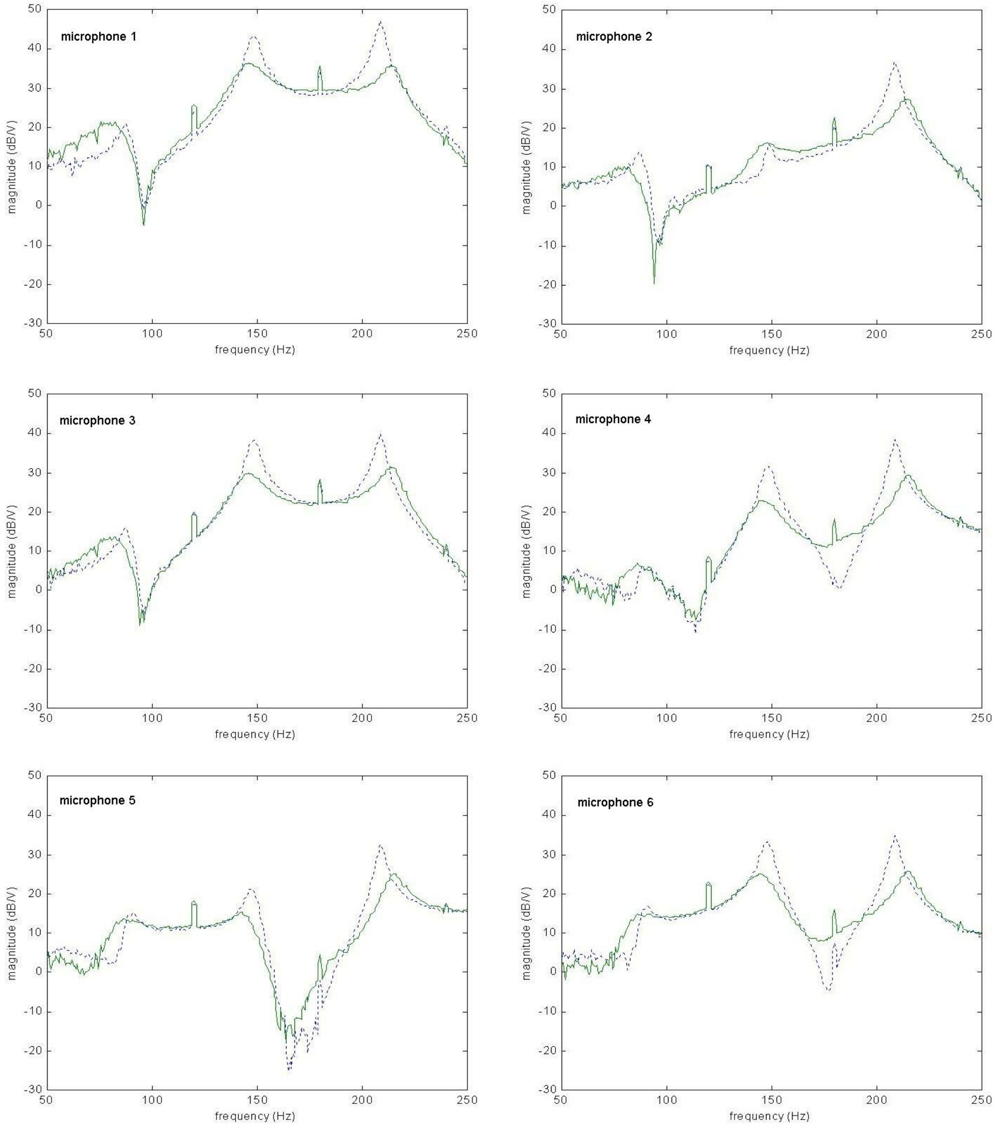

Figure 5.14: Global comparison of open (dashed) and closed (solid) loop performance within the fairing model. Each frequency response relates output pressure to disturbance signal.

Table 5.6: Pressure reductions in the full fairing geometry

Microphone	Pressure reduction in %	Pressure reduction in dB
mic_1	40.3	4.48
mic_2	40.2	4.47
mic_3	38.5	4.22
mic_4	43.1	4.90
mic_5	29.9	3.08
mic_6	39.1	4.30

required to implement this compensator (Fig. 5.15), maximum levels of 306 mV were seen during experiments. Corresponding to disturbance levels of 100 dB (C-weight,) power requirements are on the order of 1.52 mW. Considering that power levels increase on the order of 10 times per decade, the estimated power requirements given 140 dB disturbance levels would be on the order of 15.2 W. Comparing these results with those of the conical bore, it is seen that similar reductions in overall pressure can be obtained for varying volumes and geometries.

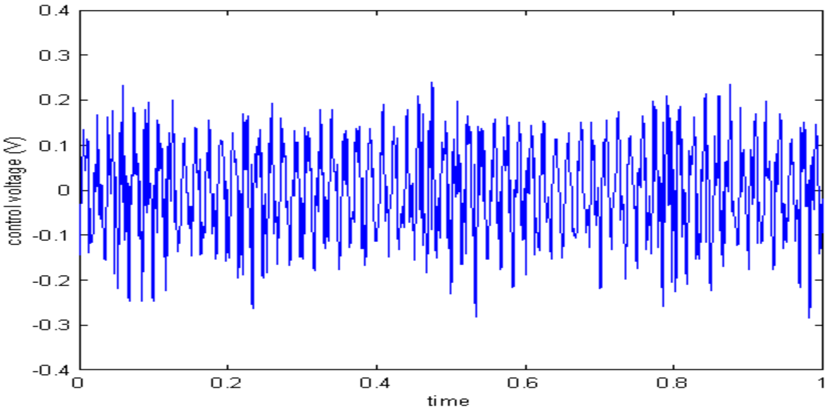

Figure 5.15: Required control voltage for PPF compensator of Table 5.6.

5.5 Chapter Summary

In this chapter the results of our experimental study have been presented. Using a test stand constructed from Lexan sheeting, both validation of our physical models and implementation of control were conducted. From the characterization experiments of section 5.2 the accuracy of both the modal and impedance based models was obtained. Upon these models PPF control was developed and simulated. Section 5.3 presents the results of implementing such control, with overall pressure reductions of 38% observed. Expansion to the full fairing geometry also revealed high levels of attenuation when PPF control is applied. Decreasing pressure levels by 40% within the fairing, this study provides an example of how applicable PPF techniques are to unmodeled systems. From the results of this chapter, physical data has been obtained from which conclusions can be drawn concerning the validity and use of the modeling processes presented in earlier chapters. A discussion of these conclusions can be found in more detail in the following chapter.

Chapter 6

Conclusions

Throughout the duration of this research the primary objective has been the control and attenuation of sound levels within payload fairings. Focusing much of our study on investigating conical geometries representative of fairings used in sounding rockets, accurate models of the coupled actuator-cavity system have been developed using modal and impedance techniques. This chapter presents the contributions of this research along with the conclusions that were drawn from our study. Finally, Section 6.3 presents a series of recommendation for future work which could be conducted in this area.

6.1 Contribution

The purpose of the research presented in this thesis is the attenuation of noise levels within launch vehicle payload fairings through the use of feedback control. Focusing on geometries similar to those found on typical sounding rockets, we have developed analytical models which predict resonance and modal properties of the acoustic environment. Having developed two separate models using modal approximation and impedance based techniques, a full characterization of the longitudinal waves within a conical bore having actuating and rigid boundary conditions has been accomplished. Allowing full variation in the mass, damping and stiffness properties of a control actuator, first-order representation of the conical fairing have been generated. Analytical and experimental comparison was used to validate the model for multiple actuator parameters. Upon this model, investigations of Linear Quadratic Regulator and Positive Position Feedback techniques have been presented and discussed. Due to very small variations in open-loop and closed-loop pole locations for the

LQR compensated system, PPF design was chosen and applied for simulation and experimental application. Implementing these controllers has shown that significant reductions in sound levels can be obtained using low authority control based on PPF design techniques. With RMS pressure reductions of 38.2% within the test-stand, power requirements were held to levels of 0.92 mW. Our study also worked to expand the control design to larger volumes with varying geometries. Selecting a fairing geometry of the Minotaur class, a half-scale model was constructed and PPF control was designed and applied. From this portion of our study the abilities of low authority control was again demonstrated as 38.5% reductions in RMS pressure were achieved. In this application power requirements were measured to be below 1.52 mW. Obtained for systems with disturbance levels of 100 dB (C-weight), the results of our study were extended to sound levels of 140 dB, correlating to those measured during actual launch conditions. Estimating power levels of 15.2 W for the half-scale model, the anticipated power requirements necessary to apply such control on a full scale fairing are on the order of 65 W, considering volumetric increases. In its entirety, the research that we have conducted has addressed the modeling and control of the fairings with conical geometries, finding that control using single actuator-sensor pairing is both possible and effective in lowering noise levels within a sealed environment.

6.2 Conclusions of our Investigation

Modeling through modal approximation provides accurate predictions of the coupling characteristics for the unforced system.

Through the modal approximation methods presented in Chapter 2, application of actuating-rigid boundary conditions produces a model of the passive system which accurately represents the system dynamics. Analytical and experimental comparison indicate that the method provides the defining characteristics of the system necessary to understand wave motion and resonance within the cavity. Considering that an understanding of the system dynamics are all that are needed for implementing many control techniques such as PPF, this model provides a suitable foundation upon which control can be developed. However, for implementation of more complex controllers modeling of the generalized force must be included. Appendix B presents a preliminary derivation of this forcing function. By including this function in the matrix equations of Chapter 2, a full model of the system can be obtained. However, the fact that modal approximation requires integration to develop each term of the mass and stiffness matrix, this method is computationally much slower than impedance methods in identifying system properties.

Impedance modeling provides accurate predictions of the coupled system for both the unforced and forced response.

As a more concise derivation, impedance models rely on the assumption that all waveforms have reached steady-state. Again considering the analytical and experimental comparisons of this model, the impedance based derivation yields nearly identical results with those of the modal approximation method. Control design, simulation and implementation have shown that the impedance model provides a suitable testbed upon which compensators can be developed. While this system neglects the transient response of the system, our analysis has shown that this oversight has little impact on the accuracy of the model. The primary drawback associated with this model is the fact that the characterization and prediction of pressure levels at specific locations within the enclosure must be solved through the development of specific impedances corresponding to the locations of interest. However, for use with collocated sensor-actuator pairing the model developed in Chapter 3 performs well with the conical bore, both in theory and in experimental application.

Single-channel, low authority controllers produce appreciable reductions in pressure within conical geometries.

Design and implementation of low authority controllers using PPF techniques are highly applicable to the sealed enclosures of our study. Providing a more straightforward design process, these controllers allow design from either simulation or experimental results. When applied to our study overall pressure reductions of 38.2% were obtained within the conical bore. Maintaining control voltages below 200 mV, this method not only performs effectively, but also efficiently.

The design process used for control design on conical systems can be expanded to larger, more complex geometries with similar levels of pressure reduction

As most of this research was intended for application in actual payload fairings, the expansion of our control methodology to larger, more complex geometries was also investigated. Using exclusively experimentally obtained results, Positive Position Feedback was applied to a half-scale model of a Minotaur class fairing. Using exactly the same implementation procedure for this larger fairing as for the conical enclosure, appreciable reductions in sound pressure levels were again obtained. Due to the relative dimensions of the system, our assumption of primarily longitudinal waves remains valid, with control performance similar to that of the conical geometry of our first model. Achieving attenuation levels of 38.5% in mean squared pressure, control voltages are kept below 306 mV. Corresponding to disturbance levels of 100 dB (C-weight,) power requirements are on the order of 1.52 mW. Considering that power levels increase on the order of 10 times per decade, the estimated power requirements given 140 dB disturbance levels would be on the order of 15.2 W.

6.3 Recommendations for Future Work

While the focus and results of this research have addressed all of the issues which motivated the study, there are several issues which could be investigated further in future work. The first of these issues is the generalized forcing function associated with the modal model. Initial work was conducted into the form of this function and are presented in Appendix B. Along with further investigation of the generalized force, additional study could be done into maximizing the coupling that exists between actuator and acoustic cavity. The LQR study presented in this thesis provides an analytical investigation into this topic, however experimental testing was not conducted due to limitations in both time and resources. Further investigation into this coupling should allow for more efficient operation of the controller.

Additional studies into application of PPF control within larger scaled fairings should also be conducted. Any changes in the geometric and volumetric parameters will alter the dynamics of the system, thereby varying the level to which the noise can be reduced as well as the power requirements necessary to accomplish this attenuation. While such a study could be conducted directly from experimental results, finite element models of the system would be advantageous in modeling the system prior to actual application. Along with application to larger geometries, the integration of our active absorber with passive approaches would provide a realistic study into the overall reductions that could be obtained within the payload fairing.

Bibliography

Agulló, J., Barjau, A., Martinez, J. "On the Time-Domain Description of Conical Bores", *Journal of the Acoustical Society of America*, Vol 91, No. 2, 1992, pp 1099-1105

AFRL Space Vehicle Directorate, "Advanced Grid Stiffened Composite Payload Shroud," Air Force Research Laboratory, http://www.vs.afrl.af.mil/Factsheets/shroud.html, Jan. 1998

Ayers, R.D., Eliason, L.J., Mahgerefteh, D., "The conical bore in musical acoustics", *American Journal of Physics*, Vol. 53, No. 6, June 1985, pp. 529-537

Bauman, P.D., Adamson, A.B., Geddes, E.R., "Acoustic Waveguides - In Practice", *Journal of the Audio Engineering Society*, Vol. 41, No. 6, June 1993, pp. 462-470

Benade, A.H., "Equivalent Circuits for Conical Waveguides", *Journal of the Acoustical Society of America*, Vol 83, No. 5, 1988, pp 1764-1769

Bies, D.A., Hansen, C.H., *Engineering Noise Control Theory and Principle*, New York, NY, E & FN Spon, 2nd ed., 1996

Boyd, S.P., Barratt, C.H., *Linear Controller Design: Limits of Performance*, Englewood Cliffs, N.J.,Prentice-Hall, 1991

DeGuilio, A.P., *A Comprehensive Experimental Evaluation of Actively Controlled Piezoceramics with Positive Position Feedback for Structural Damping*, Masters Thesis, Virginia Polytechnic Institute & State University, April 2000

Federation of American Scientists, *EELV - McDonnell-Douglas*, http://www.fas.org/spp/military/program/launch/eelv_m.htms, 1998

Franklin, G., Powell, J., Workman, M., *Digital Control of Dynamic Systems*, Menlo Park, CA, Addison-Wesley, 3rd ed., 1998

Friedland, B., *Control System Design An Introduction to State-Space Methods*, Boston, MA, McGraw-Hill, 1986

Geddes, E.R., "Acoustic Waveguide Theory", *Journal of the Audio Engineering Society*, Vol. 37, No. 7, August 1989

Geddes, E.R., "Acoustic Waveguide Theory Revisited", *Journal of the Audio Engineering Society*, Vol. 41, No. 6, June 1993, pp. 452-461

Gilbert, J., Kergomard, J., Polack, J.D., "On the Reflection Functions Associated with Discontinuities in Conical Bores", *Journal of the Acoustical Society of America*, Vol. 87, No. 4, 1990, pp 1773-1780

Glaese, R.M., Anderson, E.H., "Active Structural-Acoustic Control for Composite Payload Fairings" *SPIE Proceedings*, Vol. 3668, No. 43, pp. 450-461

Green, K.W, *Piezoceramic Actuated Transducers for Interior Acoustic Noise Control*, Masters Thesis, Virginia Polytechnic Institute & State University, 2000

Henderson, B.K., Lane, S.A., Gussy, J., Griffin, S., Farinholt, K.M., "Development of an Acoustic Actuator for Launch Vehicle Noise Reduction", *Journal of the Acoustical Society of America*, accepted July 2001

Himelblau, H., Kern, D.L., Davis, G.L., "Development of Cassini Acoustic Criteria Using Titan IV Flight Data", *Proceedings - Institute of Environmental Sciences*, Vol. 39, 1992, pp. 307-

Inman, D.J., *Engineering Vibration*, Upper Saddle River, NJ, Prentice Hall, 2nd ed., 2001

Inman, D.J., *Vibration with Control, Measurement and Stability*, Englewood Cliffs, NJ, Prentice Hall, 1989

Kinsler, L., Frey, A., Coppens, A., Sanders, J., *Fundamentals of Acoustics*, New York, NY, John Wiley and Sons, 3rd ed., 1997

Lane, S.A., Clark, R.L., Southward, S.C., “Active control of Low Frequency Modes in an Aircraft Fuselage Using Spatially Weighted Arrays”, *Transactions of the ASME - Journal of Vibrations and Acoustics*, Vol. 122, 2000, pp. 227-234

Leo, D.J., *Convex Controller Design for Linear Mechanical Systems.* PhD Dissertation, University at Buffalo, 1995

Leo, D.J., Anderson, E.H., 1998, “Vibroacoustic modeling of a launch vehicle payload fairing for active acoustic control”, *Proceedings of the 39th Structures, Structural Dynamics, and Materials Conference*, pp. 3212-3222

Leo, D.J., Limpert, D., “Letters to the Editor, A Self-Sensing Technique for Active Acoustic Attenuation”, *Journal of Sound and Vibration*, Vol. 235, No. 5, 2000, pp. 863-873

Martinez, J., Agulló, J., “Conical Bores. Part I: Reflection Functions Associated with Discontinuities”, *Journal of the Acoustical Society of America*, Vol 84, No. 5, November 1988, pp 1613-1619

Martinez, J., Agulló, J., Cardona, S. “Conical Bores. Part II: Multiconvolution”, *Journal of the Acoustical Society of America*, Vol 84, No. 5, November 1988, pp 1620-1627

McEver, M.A., *Optimal Vibration Suppression Using On-line Pole/Zero Identifcation*, Masters Thesis, Virginia Polytechnic Institute & State University, 1999

Meirovitch, L., *Computational Methods in Structural Dynamics*, Rockville, MD, Sijthoff & Noordhoff, 1980

Meirovitch, L., *Principles and Techniques of Vibrations*, Upper Saddle River, NJ, Prentice-Hall, Inc., 1997

Morse, P.M., Ingard, K.U., *Theoretical Acoustics*, New York, NY, McGraw-Hill Book Company, 1968

Nelson, P.A., Elliott, S.J., *Active Control of Sound*, San Diego, CA, Academic Press, Inc., 1995

Olson, H.F., *Music, Physics and Engineering*, Second Edition, New York, NY, Dover Publications, 1967

Pierce, A.D., *Acoustics: An Introduction to its Physical Principles and Applications*, Woodbury, NY, Acoustical Society of America, 1991

Rayleigh, J.W. Strutt, *The Theory of Sound*, New York, NY, Dover Publications, 1945

Rigden, J.S., *Physics and the Sound of Music*, New York, NY, John Wiley & Sons, 1977

Saunders, W.R., Robertshaw, H.H., Burdisso, R.A., "An evaluation of feedback, adaptive feedforward and hybrid controller designs for active structural control of lightly-damped structure." *Proceedings of the 2nd Conference on Recent Advances in Active Control of Sound and Vibration*, PA, Technomic Press, 1993, pp. 339-354

Taylor, C., *Exploring Music, The Science and Technology of Tones and Tunes*, Bristol, TN, IOP Publishing INC, 1992

Appendix A

Non-orthogonality and its Impact on Self-Adjointness and the Symmetry of State Matrix

The application of an actuating boundary condition in the modal approximation of Chapter 2 results in several interesting characteristics developing due to the particular nature this resistive boundary. In Figure A.1 the first three mode shapes have been generated for the geometric parameters of our experimental testbed. From this figure it can be seen that none of the acoustic modes of the cavity are periodic over the spatial limits r_1 to r_2. At r_1 there exists a nonzero pressure and pressure derivative, while at r_2 the pressure is maximized and the slope is driven to zero. As the waveform is assumed to be harmonic the absence of a periodicity in the standing wave over the spatial limits yields a set of mode shapes for which orthogonality does not hold.

One result of this lack of orthogonality is that it can mathematically be shown that self-adjointness also fails when applied to the system. Considering the general form of the wave equation

$$\nabla^2 p = \frac{1}{r^2}\frac{\partial}{\partial r}(r^2\frac{\partial p}{\partial r}) = \frac{1}{r}\frac{\partial^2 (rp)}{\partial r^2}, \tag{A.1}$$

analysis shows that the operator behaves symmetrically, but fails to provide self-adjointness. Following the discussion by Inman (1989), an operator is seen to be adjoint if

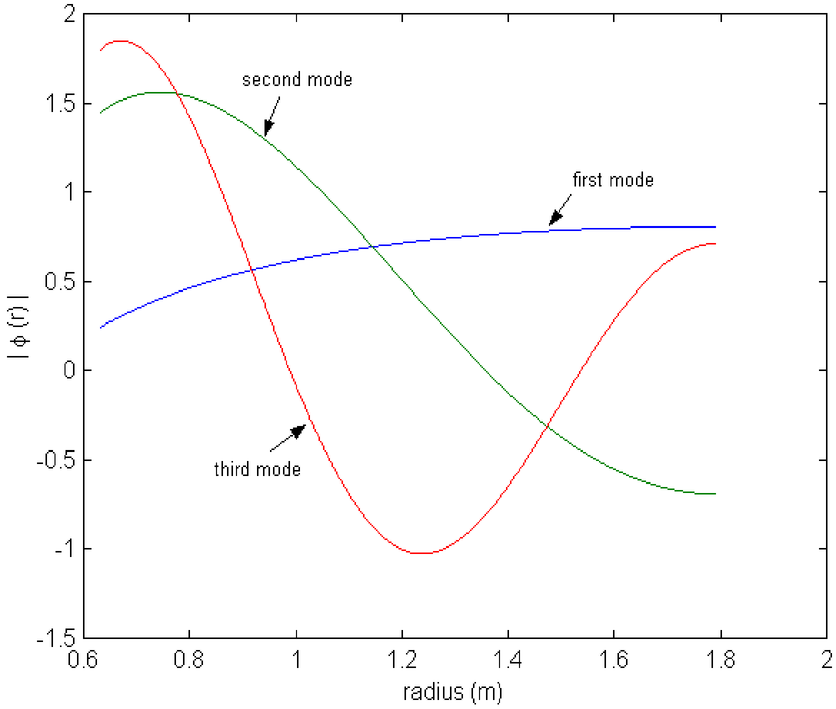

Figure A.1: First three acoustic modes for actuating-closed conical bore.

for

$$(Lu, v) = (u, L^*v)$$

$$u \in D(L), v \in D(L^*) \tag{A.2}$$

the operators L and L^* are related such that

$$Lu = L^*u, for u \in D(L)$$

and

$$D(L) = D(L^*) \tag{A.3}$$

Applying the operator of Equation (A.1), to Equation (A.2), the first condition of Equation (A.3) is satisfied, indicating that the operator is symmetric. However, the operator fails to satisfy the requirement of $D(L) = D(L^*)$, such that self-adjointness is not applicable in this system.

Due to the lack of self-adjointness, several methods for developing the mass and stiffness components are not valid. Reverting to the Galerkin method, the mass and stiffness matrices of equations 2.57 and 2.58 can still be developed. Due to the presence of the Laplacian operator in the stiffness formulation, the absence of a self-adjoint system results in an asymmetric stiffness matrix. While this asymmetry does not impact the usefulness of this model in control design and simulation, it does complicate investigations of modal controllability.

Appendix B

Development of a Generalized Forcing Function

In the modal derivation, the first step was applying laws of conservation of mass and momentum in order to develop the general wave equation and Euler's relationship. In its homogeneous form, no externally applied load were considered in the conservation of mass equation. Relaxing this requirement, it is possible to develop a form of the wave equation that incorporates a generalized forcing component within its derivation. As in the homogeneous case, the nonhomogeneous form of the wave equation is developed from the two conservation laws concerning mass and momentum. For the case at hand, the presence of an external forcing function should be introduced into equation 2.6, accomplished through the summation of externally applied loads, as in equation 2.4. Including a pressure per unit length in the summation of pressures, the following equation is developed,

$$p_{tot}S(r) - \left[p_{tot} + \frac{\partial p_{tot}}{\partial r}dr\right]S(r) + \frac{p_{ext}}{\Delta r}S(r)dr = -S(r)\frac{\partial p_{tot}}{\partial r}dr + \frac{p_{ext}}{\Delta r}S(r)dr. \tag{B.1}$$

Following the same logic used in the derivation of the momentum equation, the summation of applied loads must equal the mass times acceleration of the sample fluid particle. This consideration leads to the momentum equation with an externally applied load,

$$\left[\rho_o S(r)\frac{\partial u}{\partial t} + S(r)\frac{\partial p}{\partial r}\right] = \frac{p_{ext}}{\Delta r}S(r). \tag{B.2}$$

The initial form adopted for the externally applied load is a pressure operating over a differential length Δr. As this equation is multiplied by the cross sectional area at that specific location, this load can also be interpreted as a force operating over the same differential length Δr. Making the substitution $f_e(r,t) = \frac{p_{ext}}{\Delta r}S(r)$, the momentum equation becomes

$$\left[\rho_o S(r)\frac{\partial u}{\partial t} + S(r)\frac{\partial p}{\partial r}\right] = f_e(r,t). \tag{B.3}$$

As in our analysis of the homogeneous case, the $-\frac{\partial}{\partial t}$ of equation 2.3 and the $\frac{\partial}{\partial r}$ of equation B.2 are taken. Summing these two equations, the forced form of the wave equation is developed,

$$\frac{\partial^2\left[\rho S(r)\right]}{\partial t^2} + \rho_o\frac{\partial^2\left[uS(r)\right]}{\partial r\partial t} = \rho_o\frac{\partial^2\left[uS(r)\right]}{\partial r\partial t} + \frac{\partial}{\partial r}\left[S(r)\frac{\partial p}{\partial r}\right] - \frac{\partial f_e(r,t)}{\partial r}. \tag{B.4}$$

Simplifying, and rearranging terms, this equation yields a form similar to that of equation 2.17, with the presence of a generalized forcing term.

$$\frac{\partial}{\partial r}\left[S(r)\frac{\partial p}{\partial r}\right] - \frac{1}{c_o^2}S(r)\frac{\partial^2 p}{\partial t^2} = \frac{\partial f(r,t)}{\partial r}. \tag{B.5}$$

Now, the form of the applied force must be taken into consideration. As this external load is applied at one position only, the spatial Dirac delta is introduced to serve as a spatial qualifier, limiting the application of this force to one location, in this case to r_1. Setting the spatial component of the forcing function to be $\delta(r - r_1)$, equation B.6 takes the form

$$\frac{\partial}{\partial r}\left[S(r)\frac{\partial p}{\partial r}\right] - \frac{1}{c_o^2}S(r)\frac{\partial^2 p}{\partial t^2} = \frac{\partial \delta(r-r_1)f(t)}{\partial r}. \tag{B.6}$$

Dividing through by the cross-sectional area $S(r)$ and $\frac{1}{c_o^2}$, we obtain a from of the wave equation,

$$\frac{c_o^2}{S(r)}\frac{\partial}{\partial r}\left[S(r)\frac{\partial p}{\partial r}\right] - \frac{\partial^2 p}{\partial t^2} = \frac{c_o^2}{S(r)}\frac{\partial \delta(r-r_1)f(t)}{\partial r}. \tag{B.7}$$

As this cross-sectional area possesses a spherical contour, $S(r)$ is found to be

$$S(r) = (2\pi - 2\pi cos(\theta))\, r^2 \tag{B.8}$$

where θ is the angle of divergence associated with the conical bore. Substituting this expression into equation B.7, it is possible to apply the relationship of equation 2.16 to produce the following

$$c_o^2\frac{1}{r}\frac{\partial^2 rp}{\partial r^2} - \frac{\partial^2 p}{\partial t^2} = \frac{c_o^2}{(2\pi - 2\pi cos(\theta))\, r^2}\frac{\partial \delta(r-r_1)f(r,t)}{\partial r}. \tag{B.9}$$

Multiplying through by $-r$, a form of the wave equation is now developed which resembles a conventional force balance in the presence of an externally applied load.

$$\frac{\partial^2 rp}{\partial t^2} - c_o^2 \frac{\partial^2 rp}{\partial r^2} = \frac{-c_o^2}{\left(2\pi - 2\pi cos(\theta)\right) r} \frac{\partial \delta(r - r_1) f(r,t)}{\partial r}. \tag{B.10}$$

Now that the wave equation has been arranged such that the externally applied force has been implemented, a modal approximation of the system can be developed. It is desired that the system be represented as a set of matrix equations,

$$M \frac{\partial^2 \ddot{\beta}(t)}{\partial t^2} + K \ddot{\beta}(t) = Q f(t) \tag{B.11}$$

In order to develop this type of representation of the system, the first step is to multiply equation B.10 by the spatial solution of the homogeneous wave equation. Multiplying through by $r\varphi(r)$ and integrating over the length of the enclosure, the matrix components M, K, and Q become

$$M_{i,j} = \int_{r_1}^{r_2} \left[r\varphi_i(r)\right] \left[r\varphi_j(r)\right] dr \tag{B.12}$$

$$K_{i,j} = -c_o^2 \int_{r_1}^{r_2} \left[r\varphi_i(r)\right] \frac{\partial^2 \left[r\varphi_j(r)\right]}{\partial r^2} dr \tag{B.13}$$

$$Q_i = \frac{-c_o^2}{2\pi - 2\pi cos(\theta)} \int_{r_1}^{r_2} \varphi_i(r) \frac{\partial \delta(r - r_1)}{\partial r} dr \tag{B.14}$$

Solving for both the mass and stiffness matrices is done by relatively straightforward methods. However, integration by parts must be performed on equation B.15 in order to properly deal with this term. Following the methods of integration by parts, the integral is separated into the following components,

$$\begin{aligned} u &= \varphi(r) & dv &= \tfrac{\partial \delta(r - r_1)}{\partial r} dr \\ du &= \varphi'(r) dr & v &= \delta(r - r_1) \end{aligned} \tag{B.15}$$

Substituting these values into the definition of this integration method

$$\int_a^b u dv = uv|_a^b - \int_a^b v du, \tag{B.16}$$

the matrix form of the applied load becomes

$$Q_i = \frac{-c_o^2}{2\pi - 2\pi cos(\theta)} \left[\varphi_i(r)\delta(r-r_1)|_{r_1}^{r_2} - \int_{r_1}^{r_2} \delta(r-r_1)\varphi_i'(r)dr \right] \tag{B.17}$$

Considering the properties of the Dirac delta function this equation can be further simplified. The first term of equation B.17, $\varphi_i(r)\delta(r-r_1)|_{r_1}^{r_2}$ can be simplified through the property

$$\delta(x-a) = \begin{cases} \delta(0) & x = 0 \\ \\ 0 & x \neq 0 \end{cases} \tag{B.18}$$

Considering the properties of the Dirac delta function two simplifications can be performed on equation B.17. Applying integration properties of the Dirac delta function, $\int_{-\infty}^{\infty} \delta(x-a)g(x)dx = g(a)$, provided a falls within the limits of integration. Implementing these two properties, equation B.17 simplifies to

$$Q_i = \frac{-c_o^2}{2\pi - 2\pi cos(\theta)} \left[\varphi_i(r_1)\delta(0) - \varphi_i'(r_1) \right]. \tag{B.19}$$

Now, the presence of this $\delta(0)$ introduces some complexity as this term is not guaranteed to be finite if evaluated at zero. In Meirovitch (1980) the author evaluates a system similar to the one shown in equation B.19. Addressing a beam vibration problem Meirovitch states that the term can be neglected when applied at the boundary condition. This statement reflects the fact that $\delta(0)$ represents a sudden change in the shape of the function. Thus, if applied at a boundary, this discontinuity in the derivative considers the function shape on both sides of the boundary. However, if we are only interested in the dynamics of one side of the boundary, then this term should logically be neglected. Applying this assumption to equation B.19 reduces the generalized force to

$$Q_i = \frac{c_o^2}{2\pi - 2\pi cos(\theta)} \varphi_i'(r_1). \tag{B.20}$$

Including this term in the general form of matrix equation B.11 a first order form of the system can be developed. The primary difference in this method and that assumed with the impedance form is that no assumption of steady state has been made in the modal derivation. This fact introduces an additional set of states associated with particle velocity necessary in order to couple the electrical and acoustic systems. Constructing the corresponding state system from these equations generates an unstable velocity state. Corresponding to the coupled mechano-acoustic resonance of the piston, the pole associated with this resonances appears in the right half plane of the s-domain. However, considering that the full system is constructed from two passive components, their coupling should result in a purely stable system. The fact that this does not occur in this analysis indicates that there is a fault in the simplifications applied to the general forcing term Q_i. The fault lies in this term as opposed to the other parts of our derivation due to the fact that the passive or homogeneous form has been validated both analytically and experimentally. Further investigation of the forcing derivation indicates that the most likely place for an error in Q_i lies in the simplification applied to equation B.19. For this research however, the ability to model the system through impedance methods precluded the further investigation into this forcing term. With experimental results indicating that impedance based representations provide accurate characterizations of the system, this method was adopted for control design and simulation. It is our recommendation that further study be given to this forced form of the wave equation for analysis. The inclusion of such a generalized force would avoid the common steady-state assumption, allowing analysis of both transient and steady-state responses of the system. Applied to control, this additional understanding could provide the additional characterizations necessary to improve overall reductions in unwanted noise levels.

Appendix C

Mathematica Code Using Modal Approximation Methods

```
SetDirectory@"C:\USERS\KEVIN\RESEARCH\REDERIVATION"D;
<< LinearAlgebra`Cholesky`
```

Definition of Constants

```
factor = 1;
```

```
sys = low;
```

```
modes = 4;
```

Initialization of the physical parameters of the conic section in question.

Original Stiffness = 851.789 N/m

```
                                      7
mincir = 34.0;       maxcir = 95 + iiii ;       len = 45.75;
                                      8

         i mincir      1   y
minrad = j iiiiiiiiiii - iiiii z * 0.0254;
         k   2 p      16   {

         i maxcir      1   y
maxrad = j iiiiiiiiiii - iiiii z * 0.0254;  len = len * 0.0254;
         k   2 p      16   {

                maxrad - minrad             minrad
q = ArcSinA iiiiiiiiiiiiiiiiiiiiiiiiiiii E;  Lo = iiiiiiiiiiii ;
                     len                    Sin@qD

       maxrad
Lf = iiiiiiiiiii ;
       Sin@qD
```

Enclosure parameters.

```
boxlen = 23.5 - 18;
boxwidth = 12.5;
thk = 0.75;
foamdia = 8;
foamheight = 3;
spkrheight = 1.875;
heightsubtr = spkrheight - 1.25;
rtop = 1;
rbottom = 3.5;

boxlen = 0.0254 * boxlen;  boxwidth = 0.0254 * boxwidth;  thk = 0.0254 * thk;
foamdia = 0.0254 * foamdia;  foamheight = 0.0254 * foamheight;
spkrheight = 0.0254 * spkrheight;  heightsubtr = 0.0254 * heightsubtr;
rtop = 0.0254 * rtop;  rbottom = 0.0254 * rbottom;
inlen = boxlen - 3 * thk;  inwidth = boxwidth - 2 * thk;
                              2                p            2
foamvol = foamheight * inwidth  - foamheight * ¡¡¡ * foamdia ;
                                               4
                     2                          2
          p * rbottom  * spkrheight    p * rtop  * heightsubtr
spkrvol = ¡¡¡¡¡¡¡¡¡¡¡¡¡¡¡¡¡¡¡¡¡¡¡¡¡¡ - ¡¡¡¡¡¡¡¡¡¡¡¡¡¡¡¡¡¡¡¡¡¡¡¡¡ ;
                     3                           3
                     2
vol = inlen * inwidth  - foamvol - spkrvol;
```

Speaker parameters

```
stiff = 851.789;
mass = 0.01838;
area = 0.0214;
                  3
Po = 102.65624 * 10 ;
g = 1.402;
```

Calculation of natural frequency with enclosure included

```
                 gPo      2
            stiff + ¡¡¡ area                          1
natfreqW = $ ¡¡¡¡¡¡¡¡¡¡¡¡¡¡¡¡¡¡¡ ; natfreqf = natfreqW * ¡¡¡¡
                  mass                                2 p
```

System model using experimentally determined speaker resonance

```
measurednatfreq = 197.5;
natfreqW = 2 p measurednatfreq
                                                 2
If @sys « high, 8stiffness = mass * natfreqW <D
If @sys « low, 8stiffness = stiff<D

stiffness
```

```
S@rD = 2 p H1 - Cos@qDL r2;
```

ÿ Begin with the assumed solution to the wave equation

```
            A                B
f@r, tD = J iiii Ąąkr + iiii Ą-ąkrN Ąąwt;
            r                r
          A               B
y@rD =  iiii Ąąkr + iiii Ą-ąkr;
          r               r

y '@rD = ×r y@rD;
ry '@rD = ×r HExpand@r y@rDDL;
```

Instead of defining the form of the temporal solution of the potential function, leave this component generalized as   [t]

```
fs@r, tD = y@rD h@tD;
```

Now, using the relationships of Bies and Hanson, particle velocity and pressure can be defined as follows

ÿ

Now consider the boundary conditions associated with a closed conical bore.

At r_2 the boundary condition is such that the spatial derivative of pressure is zero

```
BC2 = ×r p@r, tD ±.  bÃÃ@tD Ï 1 ±. r Ï r2

j    B Ą-ąkr2        A Ąąkr2        ą B Ą-ąkr2 k      ą A Ąąkr2 k  y
j- iiiiiiiiiiiiii - iiiiiiiiiiiii - iiiiiiiiiiiiiiiiii + iiiiiiiiiiiiiiiiii z r
k     r22              r22              r2                r2        {

BC2rule = HSolve@HBC2L « 0, ADL ±± Chop

       B Ą-2 ąkr2 H-ą + k r2L
99A Ï  iiiiiiiiiiiiiiiiiiiiiiiii ==
            ą + k r2
```

At ***r****$_1$, the boundary condition is defined through a force summation at the speaker face*

```
BC1eqn = ms a@r, tD + cs u@r, tD + ks x@r, tD + As p@r, tD - F@tD;
```

```
BC1full = BC1eqn ±. 8bÅÅ@tD Ï -w2 b@tD, b'@tD Ï ą w b@tD<
```

```
          j   B Ą-ąkr     A Ąąkr     ą B Ą-ąkr k     ą A Ąąkr k y
-F@tD - ks | - iiiiiiiiiii - iiiiiiiiii - iiiiiiiiiiiiiii + iiiiiiiiiiiiiii z b@tD -
          k     r2          r2            r               r       {
      j   B Ą-ąkr     A Ąąkr     ą B Ą-ąkr k     ą A Ąąkr k y
 ą cs | - iiiiiiiiiii - iiiiiiiiii - iiiiiiiiiiiiiii + iiiiiiiiiiiiiii z w b@tD +
      k     r2          r2            r               r       {
    j   B Ą-ąkr     A Ąąkr     ą B Ą-ąkr k     ą A Ąąkr k y
 ms | - iiiiiiiiiii - iiiiiiiiii - iiiiiiiiiiiiiii + iiiiiiiiiiiiiii z w2 b@tD -
    k     r2          r2            r               r       {
    j B Ą-ąkr     A Ąąkr  y
 As | iiiiiiiiiii + iiiiiiiiii z r w2 b@tD
    k   r          r      {
```

Considering the homogeneous solution to this equation, we must consider the case in which F[t] goes to zero, thus the boundary condition simplifies to

```
BC1 = BC1full ±. F@tD Ï 0;
```

```
        HHBC1 ±. BC2ruleL ±. 8k Ï w , B Ï 1, r Ï r1<L
                                  c
eqn = iiiiiiiiiiiiiiiiiiiiiiiiiiiiiiiiiiiiiiiiiiiiiiiiiiiiii ±± ExpToTrig ±± Simplify
                          b@tD
```

```
           1
9 iiiiiiiiiiiiiiiiiiiiiiiiiii
  c r12 Hą c + r2 wL
   JJc w Hks Hr1 - r2L + w Hą cs Hr1 - r2L + H-ms r1 + ms r2 + As r1 r2 rL wLL
          Hr1 - r2L w
      CosA iiiiiiiiiiiiiii E +
               c
     Hr1 r2 w2 H-ks + w H-ą cs + ms wLL + c2 H-ks + w H-ą cs + ms w + As r1 r wLLL
          Hr1 - r2L w                    r2 w                r2 w
      SinA iiiiiiiiiiiiiii EN J-2 CosA iiiiii E + 2 ą SinA iiiiii ENN=
               c                        c                     c
```

Extract the numerator and denominator of the governing equation in order to develop a transcendental equation which defines the natural frequencies of the system

```
Num = Numerator@eqnD;
Den = Denominator@eqnD
```

Develop the transcendental equation, separating the real and imaginary components from one another

The real and imaginary components of the transcendental equations, will be used to develop an objective function to solve for the natural frequencies of the system

$$\begin{aligned}
&\text{REALeqn} = -\text{H}c^2 + \text{r2}^2\ \text{w}^2\text{L Hcs r1 w}^2 + \text{c H-ks + Hms + As r1 rL w}^2\text{LL CosA}\frac{\text{r1 w}}{\text{c}}\text{E} + \\
&\quad \text{H-c}^2\ \text{cs Hr1 - 2 r2L w}^2 + \text{cs r1 r2}^2\ \text{w}^4 + \text{c}^3\ \text{H-ks + Hms + As r1 rL w}^2\text{L} - \\
&\qquad \text{c r2 w}^2\ \text{Hks H2 r1 - r2L + H-2 ms r1 + ms r2 + As r1 r2 rL w}^2\text{LL CosA}\frac{\text{Hr1 - 2 r2L w}}{\text{c}}\text{E} + \\
&\quad \text{w}\underset{\text{k}}{\text{j}}\text{Hc}^2 + \text{r2}^2\ \text{w}^2\text{L Hc cs + r1 Hks - ms w}^2\text{LL SinA}\frac{\text{r1 w}}{\text{c}}\text{E} + \\
&\qquad \text{Hc}^3\ \text{cs + c cs H2 r1 - r2L r2 w}^2 + \text{r1 r2}^2\ \text{w}^2\ \text{Hks - ms w}^2\text{L} + \\
&\qquad\quad \text{c}^2\ \text{H-ks Hr1 - 2 r2L + Hms r1 - 2 ms r2 - 2 As r1 r2 rL w}^2\text{LL SinA}\frac{\text{Hr1 - 2 r2L w}}{\text{c}}\text{E}\underset{\{}{\text{y}};
\end{aligned}$$

$$\begin{aligned}
&\text{IMAGeqn} = \text{w Hc cs + ks r1 - ms r1 w}^2\text{L Hc}^2 + \text{r2}^2\ \text{w}^2\text{L CosA}\frac{\text{r1 w}}{\text{c}}\text{E} + \\
&\quad \text{w H-c}^3\ \text{cs + c cs r2 H-2 r1 + r2L w}^2 + \text{r1 r2}^2\ \text{w}^2\ \text{H-ks + ms w}^2\text{L} + \\
&\qquad \text{c}^2\ \text{Hks Hr1 - 2 r2L + H-ms r1 + 2 ms r2 + 2 As r1 r2 rL w}^2\text{LL CosA}\frac{\text{Hr1 - 2 r2L w}}{\text{c}}\text{E} - \\
&\quad \text{c}^3\ \text{ks SinA}\frac{\text{r1 w}}{\text{c}}\text{E} + \text{c}^3\ \text{ms w}^2\ \text{SinA}\frac{\text{r1 w}}{\text{c}}\text{E} + \text{c}^2\ \text{cs r1 w}^2\ \text{SinA}\frac{\text{r1 w}}{\text{c}}\text{E} - \\
&\quad \text{c ks r2}^2\ \text{w}^2\ \text{SinA}\frac{\text{r1 w}}{\text{c}}\text{E} + \text{As c}^3\ \text{r1 r w}^2\ \text{SinA}\frac{\text{r1 w}}{\text{c}}\text{E} + \text{c ms r2}^2\ \text{w}^4\ \text{SinA}\frac{\text{r1 w}}{\text{c}}\text{E} + \\
&\quad \text{cs r1 r2}^2\ \text{w}^4\ \text{SinA}\frac{\text{r1 w}}{\text{c}}\text{E} + \text{As c r1 r2}^2\ \text{r w}^4\ \text{SinA}\frac{\text{r1 w}}{\text{c}}\text{E} - \text{c}^3\ \text{ks SinA}\frac{\text{Hr1 - 2 r2L w}}{\text{c}}\text{E} + \\
&\quad \text{c}^3\ \text{ms w}^2\ \text{SinA}\frac{\text{Hr1 - 2 r2L w}}{\text{c}}\text{E} - \text{c}^2\ \text{cs r1 w}^2\ \text{SinA}\frac{\text{Hr1 - 2 r2L w}}{\text{c}}\text{E} + \\
&\quad \text{2 c}^2\ \text{cs r2 w}^2\ \text{SinA}\frac{\text{Hr1 - 2 r2L w}}{\text{c}}\text{E} - \text{2 c ks r1 r2 w}^2\ \text{SinA}\frac{\text{Hr1 - 2 r2L w}}{\text{c}}\text{E} + \\
&\quad \text{c ks r2}^2\ \text{w}^2\ \text{SinA}\frac{\text{Hr1 - 2 r2L w}}{\text{c}}\text{E} + \text{As c}^3\ \text{r1 r w}^2\ \text{SinA}\frac{\text{Hr1 - 2 r2L w}}{\text{c}}\text{E} + \\
&\quad \text{2 c ms r1 r2 w}^4\ \text{SinA}\frac{\text{Hr1 - 2 r2L w}}{\text{c}}\text{E} - \text{c ms r2}^2\ \text{w}^4\ \text{SinA}\frac{\text{Hr1 - 2 r2L w}}{\text{c}}\text{E} + \\
&\quad \text{cs r1 r2}^2\ \text{w}^4\ \text{SinA}\frac{\text{Hr1 - 2 r2L w}}{\text{c}}\text{E} - \text{As c r1 r2}^2\ \text{r w}^4\ \text{SinA}\frac{\text{Hr1 - 2 r2L w}}{\text{c}}\text{E};
\end{aligned}$$

Development of an objective function from which to extract the natural frequencies of the system

$$\text{OBJFUN} = \text{Sqrt@REALeqn}^2 + \text{IMAGeqn}^2\text{D};$$

$$\begin{aligned}
&\text{objf} = 10\,\hat{}\,\text{-17 OBJFUN ±. 8As Ï area, ms Ï 1*mass, ks Ï stiffness, r1 Ï Lo,} \\
&\qquad \text{r2 Ï Lf, k Ï f*2p±c, w Ï f*2*p, r Ï 1.206, F Ï 0, cs Ï 0, B Ï 1< ±. c Ï 343;}
\end{aligned}$$

```
Plot@objf, 8f, 0, 1200<D
```

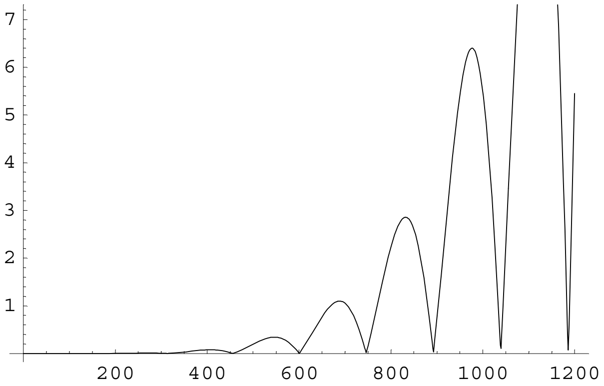

```
¦ Graphics ¦
```

Using a FIND MINIMUM command, locate the minima points of the objective function, these define the natural frequencies of the system

```
If@sys « low, 8f1i = 40<D;
If@sys « high, 8f1i = 150<D;

frequency = 8f ±. Part@Part@FindMinimum@objf, 8f, f1i, 10, 220<D, 2D, 1D,
   f ±. Part@Part@FindMinimum@objf, 8f, 240, 160, 320<D, 2D, 1D,
   f ±. Part@Part@FindMinimum@objf, 8f, 369, 290, 450<D, 2D, 1D,
   f ±. Part@Part@FindMinimum@objf, 8f, 481, 430, 630<D, 2D, 1D,
   f ±. Part@Part@FindMinimum@objf, 8f, 605, 575, 635<D, 2D, 1D,
   f ±. Part@Part@FindMinimum@objf, 8f, 747, 740, 755<D, 2D, 1D,
   f ±. Part@Part@FindMinimum@objf, 8f, 893, 890, 895<D, 2D, 1D,
   f ±. Part@Part@FindMinimum@objf, 8f, 1039, 1035, 1045<D, 2D, 1D,
   f ±. Part@Part@FindMinimum@objf, 8f, 1186, 1180, 1190<D, 2D, 1D<;
```

The values of the system's natural frequencies are as follows

```
frequency
```

ÿ

Now consider the development of the system mode shapes

First, define the wave number associated with the solution to the modeshape

```
        2 * p * frequency
kmat = ¡¡¡¡¡¡¡¡¡¡¡¡¡¡¡¡¡¡¡¡¡¡¡¡¡¡¡¡¡¡¡¡¡¡¡ ±. c Ï 343
                c
k1 = kmat@@1DD; k2 = kmat@@2DD; k3 = kmat@@3DD; k4 = kmat@@4DD;
k5 = kmat@@5DD; k6 = kmat@@6DD; k7 = kmat@@7DD; k8 = kmat@@8DD; k9 = kmat@@9DD;
```

First consider the modeshapes of the acoustic potential and pressure

```
y@rD ±. BC2rule
```

```
  B Ą-ą k r     B Ąą k r-2 ą k r2 H-ą + k r2L
9 ¡¡¡¡¡¡¡¡¡¡¡ + ¡¡¡¡¡¡¡¡¡¡¡¡¡¡¡¡¡¡¡¡¡¡¡¡¡¡¡¡¡¡¡¡¡ =
      r                r Hą + k r2L
```

```
ymode@rD = y@rD ±. BC2rule ±. r2 Ï Lf
ymode '@rD = y '@rD ±. BC2rule ±. r2 Ï Lf;
rymode '@rD = ry '@rD ±. BC2rule ±. r2 Ï Lf;
```

```
  B Ą-ą k r     B Ą-3.58643 ą k+ą k r H-ą + 1.79322 kL
9 ¡¡¡¡¡¡¡¡¡¡¡ + ¡¡¡¡¡¡¡¡¡¡¡¡¡¡¡¡¡¡¡¡¡¡¡¡¡¡¡¡¡¡¡¡¡¡¡¡¡¡¡¡¡¡¡¡¡¡ =
      r                Hą + 1.79322 kL r
```

Normalize the system such that the diagonals of the mass matrix go to unity

```
coeffy =
          Lf
  - j j ā    HHr ymode@rDL * Hr ymode@rDLL ăr ±. 8k Ï kmat, r1 Ï Lo, r2 Ï Lf, c Ï 343<y ´
    k k   Lo                                                                         z
                                                                                     {
     y
    B2z;
     {
By = 1 ± 88-coeffy@@1, 1DD, -coeffy@@1, 2DD,
      -coeffy@@1, 3DD, coeffy@@1, 4DD, coeffy@@1, 5DD, -coeffy@@1, 6DD,
      -coeffy@@1, 7DD, coeffy@@1, 8DD, coeffy@@1, 9DD<<;

ymode@rD;
```

Apply the normalization coefficients and the corresponding wave number to generate a vector of mode shapes. These constitute the first nine modes of the acoustic cavity.

```
ytrans = Hymode@rD ±. B Ï By@@1DDL;
```

```
ymat = 8ytrans@@1, 1DD ±. k Ï kmat@@1DD,
    ytrans@@1, 2DD ±. k Ï kmat@@2DD, ytrans@@1, 3DD ±. k Ï kmat@@3DD,
    ytrans@@1, 4DD ±. k Ï kmat@@4DD, ytrans@@1, 5DD ±. k Ï kmat@@5DD,
    ytrans@@1, 6DD ±. k Ï kmat@@6DD, ytrans@@1, 7DD ±. k Ï kmat@@7DD,
    ytrans@@1, 8DD ±. k Ï kmat@@8DD, ytrans@@1, 9DD ±. k Ï kmat@@9DD< ±± Chop;
```

```
ymat ±± ExpToTrig ±± Simplify ±± Chop
```

```
If@modes « 1, 8Plot@8ymat@@1DD<, 8r, Lo, Lf<D<D
If@modes « 2, 8Plot@8ymat@@1DD, ymat@@2DD<, 8r, Lo, Lf<D<D
If@modes « 4,
 8Plot@8ymat@@1DD, ymat@@2DD, ymat@@3DD, ymat@@4DD<, 8r, Lo, Lf<D<D
If@modes « 9, 8Plot@8ymat@@1DD, ymat@@2DD, ymat@@3DD, ymat@@4DD,
    ymat@@5DD, ymat@@6DD, ymat@@7DD, ymat@@8DD, ymat@@9DD<, 8r, Lo, Lf<D<D
```

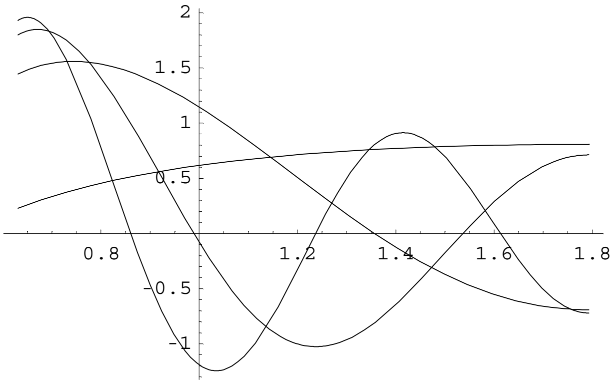

```
8¦ Graphics ¦<
```

Determine the number of modeshapes desired for the modal approximation

```
If@modes « 1, 8ymat = ymat@@1DD<D;
If@modes « 2, 8ymat = 8ymat@@1DD, ymat@@2DD<<D;
If@modes « 4, 8ymat = 8ymat@@1DD, ymat@@2DD, ymat@@3DD, ymat@@4DD<<D;
If@modes « 9, 8ymat = 8ymat@@1DD, ymat@@2DD, ymat@@3DD, ymat@@4DD,
     ymat@@5DD, ymat@@6DD, ymat@@7DD, ymat@@8DD, ymat@@9DD<<D;
```

Using the mode shapes developed for the acoustic potential and pressure, those associated with displacement, velocity and acceleration will now be generated.

```
umat = -×r ymat ±± Chop;
Chop@Simplify@ExpToTrig@umatDD, 10-9D;
```

```
Transpose@8umat<D;
```

```
If@modes « 1, 8Plot@8umat<, 8r, Lo, Lf<D<D
If@modes « 2, 8Plot@8umat@@1DD, umat@@2DD<, 8r, Lo, Lf<D<D
If@modes « 4,
 8Plot@8umat@@1DD, umat@@2DD, umat@@3DD, umat@@4DD<, 8r, Lo, Lf<D<D
If@modes « 9, 8Plot@8umat@@1DD, umat@@2DD, umat@@3DD, umat@@4DD,
    umat@@5DD, umat@@6DD, umat@@7DD, umat@@8DD, umat@@9DD<, 8r, Lo, Lf<D<D
```

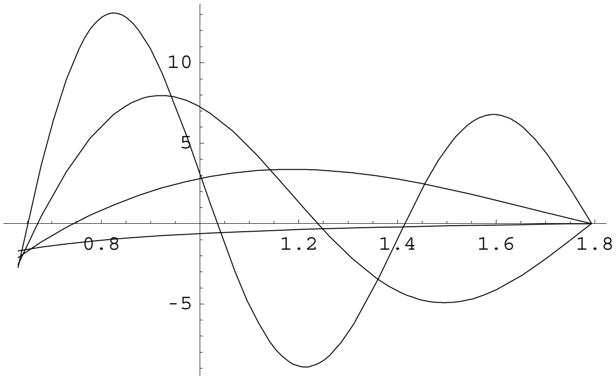

```
8¦ Graphics ¦<
```

ÿ Now consider the force balance equation at the speaker face.

```
M =
  i   r2                                       y
  jā    ms * Transpose@8r4 umat<D.8umat< ărz ±. 8r1 Ï Lo, r2 Ï Lf, ms Ï mass< ±± Chop;
  k   r1                                       {

    i   r2                                       y
K = jā    ks * Transpose@8r4 umat<D.8umat< ărz ±.
    k   r1                                       {
   8r1 Ï Lo, r2 Ï Lf, ks Ï stiffness< ±± Chop

      i   r2                                         y
Q = - jā    S@rD * Transpose@8r4 umat<D.8ymat< ărz ±.
      k   r1                                         {
   8r1 Ï Lo, r2 Ï Lf, ms Ï mass< ±± Chop
```

Appendix D

Mathematica Code Using Impedance Methods

```
SetDirectory@"C:\USERS\KEVIN\RESEARCH\REDERIVATION"D;
<< LinearAlgebra`Cholesky`
```

Definition of Constants

```
factor = 1;
```

```
sys = low;
```

```
modes = 4;
```

Initialization of the physical parameters of the conic section in question.

Original Stiffness = 851.789 N/m

```
                                  7
mincir = 34.0;      maxcir = 95 + iiii ;      len = 45.75;
                                  8
         i mincir         1   y                  i maxcir         1   y
minrad = j iiiiiiiiiiii - iiiii z * 0.0254; maxrad = j iiiiiiiiiiii - iiiii z * 0.0254;  len = len * 0.0254;
         k   2 p         16   {                  k   2 p         16   {
           maxrad - minrad                 minrad
 q = ArcSinA iiiiiiiiiiiiiiiiiiiiiiiiiiiiiiiiii E;  Lo = iiiiiiiiiiiii ;
                 len                       Sin@qD
      maxrad
 Lf = iiiiiiiiiiiii ;
      Sin@qD
```

Enclosure parameters.

```
boxlen = 23.5 - 18;
boxwidth = 12.5;
thk = 0.75;
foamdia = 8;
foamheight = 3;
spkrheight = 1.875;
heightsubtr = spkrheight - 1.25;
rtop = 1;
rbottom = 3.5;

boxlen = 0.0254 * boxlen;  boxwidth = 0.0254 * boxwidth;  thk = 0.0254 * thk;
foamdia = 0.0254 * foamdia;  foamheight = 0.0254 * foamheight;
spkrheight = 0.0254 * spkrheight;  heightsubtr = 0.0254 * heightsubtr;
rtop = 0.0254 * rtop;  rbottom = 0.0254 * rbottom;
inlen = boxlen - 3 * thk;  inwidth = boxwidth - 2 * thk;
                                                    p
foamvol = foamheight * inwidth^2 - foamheight * iiii * foamdia^2;
                                                    4
           p * rbottom^2 * spkrheight    p * rtop^2 * heightsubtr
spkrvol = iiiiiiiiiiiiiiiiiiiiiiiiiiiii - iiiiiiiiiiiiiiiiiiiiiiiiiii ;
                      3                             3
vol = inlen * inwidth^2 - foamvol - spkrvol;
```

Speaker parameters

```
stiff = 851.789;
mass = 0.01838;
area = 0.0214;
Po = 102.65624 * 10^3;
g = 1.402;
```

Calculation of natural frequency with enclosure included

```
                      g Po
               stiff + iiii area^2
                       vol                                  1
natfreqW = & iiiiiiiiiiiiiiiiiiiiiiii ; natfreqf = natfreqW * iiiiii
                    mass                                   2 p
```

System model using experimentally determined speaker resonance

```
measurednatfreq = 197.5;
natfreqW = 2 p measurednatfreq

If @sys « high, 8stiffness = mass * natfreqW^2<D
If @sys « low, 8stiffness = stiff<D

stiffness
```

Surface area of speaker face

ÿ Begin with the assumed solution to the wave equation

```
             A          B
f@r, tD = J iiii Ąą k r + iiii Ą-ą k rN Ąą w t;
             r          r

        A          B
y@rD = iiii Ąą k r + iiii Ą-ą k r;
        r          r

y '@rD = ×r y@rD;
ry '@rD = ×r HExpand@r y@rDDL;
```

Instead of defining the form of the temporal solution of the potential function, leave this component generalized as   [t]

```
fs@r, tD = y@rD h@tD;
```

Now, using the relationships of Bies and Hanson, particle velocity and pressure can be defined as follows

ÿ

ÿ Now consider the development of the system mode shapes

First, define the wave number associated with the solution to the modeshape

First consider the modeshapes of the acoustic potential and pressure

```
phi = f@r, tD;

Pimp = r ×t phi;
```

Using the mode shapes developed for the acoustic potential and pressure, those associated with displacement, velocity and acceleration will now be generated.

```
Uimp = -×r phi;
```

Now develop the impedance of the system. Defining $\frac{p}{u}$ as Z_{acoustic}

Acoustic impedance is defined as $\frac{\text{pressure}}{\text{volume velocity}}$.

```
            Pimp
Zacoustic = ¡¡¡¡¡¡¡¡¡ ±± Simplify
            Uimp
```

```
        HB + A A2ąkrL r r w
¡¡¡¡¡¡¡¡¡¡¡¡¡¡¡¡¡¡¡¡¡¡¡¡¡¡¡¡¡¡¡¡¡¡¡¡¡¡¡¡¡¡¡¡
B H-ą + k r L - A A2ąkr Hą + k r L
```

Impedance at r1

```
                                                                      2 p fimp
Zmr1 = area * Zacoustic ±. 9r Ï Lo, r2 Ï Lf, w Ï 2 p fimp, k Ï ¡¡¡¡¡¡¡¡¡¡¡¡¡¡ , r Ï 1.206= ±. c Ï 343 ±±
                                                                         c
   Simplify;
```

Solve for coefficient A thru application of an infinite impedance at r2

```
Arule =
                                                                                   2 p fimp
  SolveAZmr2 « jarea * Zacoustic ±. 9r Ï Lf, r2 Ï Lf, w Ï 2 p fimp, k Ï ¡¡¡¡¡¡¡¡¡¡¡¡¡¡ , r Ï 1.206= ±.
               k                                                                      c
       c Ï 343 ±± Simplifyy
                          z, AE;
                          {
```

Apply this substitution for A, and take the limit of the impedance at r1 as the impedance at r2 goes to infinite

```
Zmr1final = Limit@Zmr1 ±. Arule, Zmr2 Ï ÆD;
```

Compare this impedance with that obtained through the use of the A substitution developed in the boundary condition analysis.

```
Zmr1temp =
                                                                     2 p fimp
  Zmr1 ±. BC2rule ±. 9r Ï Lo, r2 Ï Lf, w Ï 2 p fimp, k Ï ¡¡¡¡¡¡¡¡¡¡¡¡¡¡ , r Ï 1.206= ±. c Ï 343 ±±
                                                                        c
   Simplify;
```

Include the mechanical impedance of the speaker

```
Zmd = ą Hw ms - ks ± wL ±. 8w Ï 2 p fimp, ms Ï mass, ks Ï stiffness<;
```

The total impedance is the sum of the acoustic and the mechanical impedances

```
Ztotal = Zmr1final + Zmd ±± Simplify;
Ztotal ±± InputForm;
```

```
      135.566
9ą J- ¡¡¡¡¡¡¡¡¡¡¡¡¡¡¡¡ + 0.115485 fimpN +
       fimp
  H8.85228 fimp HH0. - 30.4426 ąL + 1. fimp + Ą0.0425736 ą fimp HH0. + 30.4426 ąL + 1. fimpLLL ±
   H1. Ą0.0425736 ą fimp HH0. + 30.4426 ąL + fimpL HH0. - 86.491 ąL + fimpL -
     1. HH0. - 30.4426 ąL + fimpL HH0. + 86.491 ąL + fimpLL=
```

```
HZtotal ±± ExpToTrig ±± Simplify ±± ChopL;
```

```
   135.566 ą
9- ¡¡¡¡¡¡¡¡¡¡¡¡¡¡¡¡¡ + 0.115485 ą fimp +
     fimp
  H8.85228 fimp H-30.4426 ą + 1. fimp + H30.4426 ą + 1. fimpL Cos@0.0425736 fimpD +
       H-30.4426 + 1. ą fimpL Sin@0.0425736 fimpDLL ± H-2633.01 - 56.0484 ą fimp - 1. fimp^2 +
     1. H30.4426 ą + fimpL H-86.491 ą + fimpL HCos@0.0425736 fimpD + ą Sin@0.0425736 fimpDLL=
```

The reactance of this system is defined as the imaginary component of the impedance.

```
react = Chop@Table@Ztotal, 8fimp, .2, 350, .1<D, 10^-7D;

ListPlot@Transpose@reactD@@1DD * ąD
```

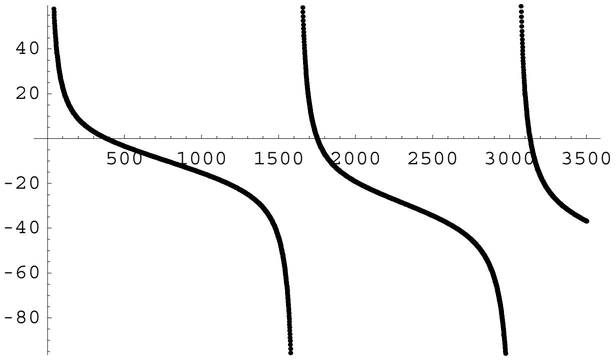

```
¦ Graphics ¦
```

```
ListPlot@Abs@Transpose@reactD@@1DD * ąDD
```

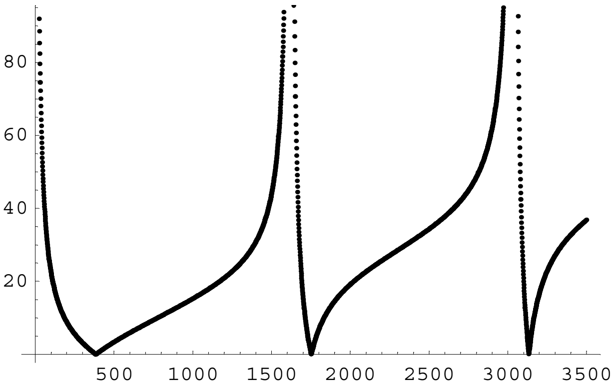

```
¦Graphics¦
```

Appendix E

MATLAB Program Used to Generate LQR Curves

```
clear all;
close all;

spkrtype=0;

impulse_mag=0.5e4;
varlength=1;

%_____________________________________________________________
% Physical parameters of the system

theta=0.216948;
area=.0214; % meters^2
mass_air= 0;  % kilograms
ms= 0.01838; % kilograms
flux= 6.77; % Flux(Tesla-N/A)
resistance= 6.6; % ohms
inductance= .93E-3; % Henries
r1=0.631165; % meters
r2=1.79322;
density=1.206;
P0=101.3E3;
gamma=1.4;
c=343;


%_____________________________________________________________
% Define frequency vectors
```

```
f=0.01:0.1:1200;
w=2*pi*f;
k=w/c;

%__________________________________________________________
% Frequency domain transfer functions between pressure
% and voltage, and pressure and current

Za=impedance_calc(0,r1,r2,k,w,area,density);


%__________________________________________________________
% Generate a s-plane transfer function of the system impedance

if spkrtype==0;
zetanum=0.0005; % Define damping coefficient for numerator
zetaden=0.000003; % Define a damping coefficient for denominator
end

if spkrtype==1;
zetanum=0.0005; % Define damping coefficient for numerator
zetaden=0.00005; % Define a damping coefficient for denominator
end


sys=series(transfer_function_5mode(Za,zetanum,zetaden,f),tf(1,[1,0.0]));

%___________________________________________________________
% There exists a gain which must be accounted for.

frfini=reshape(freqresp(sys,f*2*pi),length(f),1);

index=0;
for count=1:1:30;
gain(count)=(abs(Za(count)))/(abs(frfini(count)));
end

gainave=sum(gain)/length(gain);


%___________________________________________________________
% Including this average gain, the system becomes

sys = gainave*sys;

%___________________________________________________________
% Use a modal canonical transformation to place system into state space form
```

```
sys_ss=canon(sys,'modal');

%___________________________________________________________
% Extract the frf information of the transfer function

[mag,phase,freq,frf_model,ind_model]=freq_data(sys,1200);

%___________________________________________________________
% Extract the system information from this canonical system

[mag_ss,phase_ss,freq_ss,frf_model_ss,ind_model_ss]=freq_data(sys_ss,1200);

%___________________________________________________________
%___________________________________________________________

save_count=53;

for ks=13251.789:1000:29251.789

clear  r RANGE rval last_pressure last_voltage rms_pressure rms_voltage mult

[Atot,Btot,Ctot,Dtot,sys_tot]=coupled_system(sys_ss,ks,ms,flux,...
resistance,inductance,area);

[mag_tot,phase_tot,freq_tot,frf_model_tot,ind_model_tot]=...
freq_data(sys_tot,800);


%%%%%%%%%%%%%%%%%%%%%%%%%%%%%%%%%%%%%%%%%%%%%%%%%%%%%%%%%%%%%%%%%%%%%%%%%%%

% With the system development from above, move into the development of
% LQR control

%%%%%%%%%%%%%%%%%%%%%%%%%%%%%%%%%%%%%%%%%%%%%%%%%%%%%%%%%%%%%%%%%%%%%%%%%%%

% Consider the system controllability

sizeA=length(Atot);
    A_Q_N=Atot;
A_Q_N(2:sizeA,:)=10^-4.1*A_Q_N(2:sizeA,:);
    Q=zeros(sizeA);
N=zeros(sizeA);
for count=linspace(1,sizeA,sizeA);
   Q(:,count)=A_Q_N^(count-1)*Btot;
    N(:,count)=(A_Q_N)^(count-1)*Ctot';
end
rank_Q = rank(Q);
```

```
rank_N = rank(N);

%_____________________________________________
%
% Now introduce the disturbance matrices E and F

F=zeros(sizeA,1);
for count= 5:2:sizeA;
   F(count)=1;
end

%_____________________________________________

% PART 7.

% Now consider the application of LQR control
       % Will weight according to the output matrix,
       % as well as the control effort

G=ones(1,length(Btot));
cl_eig=eig(Atot);

additional=1;

vect1=0:0.5:100;
vect2=95:5:500;
vect3=500:100:10000;
vect4=10000:1000:1000000;

RANGE=[vect1,vect2,vect3,vect4];

counter = 1;
mult=1;

for rval= RANGE;
      Q=10*Ctot'*Ctot;

      R=rval;
      r(mult)=rval;

try
   [G,S,cl_eig]=lqr(Atot,Btot,Q,R);
catch

   err_R(mult,1)=R;

   try
      rval=rval+(RANGE(mult+1)-RANGE(mult));
```

```
   catch
   end

end

%_____________________________________________
% Define systems using lqr gains

sys_lqr=ss(Atot-Btot*G,Btot,Ctot,Dtot);

%_____________________________________________
% Solve for the disturbance gains

%_____________________________________________

% PART 8.


% NOW MOVING ON TO OBSERVER DESIGN

x0=zeros(1,sizeA);  %INITIAL CONDITIONS
x0_est=ones(1,sizeA);

% Define new pole locations, will make 5 times faster than CL poles

real_LQR=real(cl_eig);
imag_LQR=imag(cl_eig);

poles_obs=sort(5*real_LQR+imag_LQR*i);

% Determine observer gain matrix K and develop equivalent State rep.

K_obs = place(Atot',Ctot',poles_obs)';

%______________________________________________
% Now develop the closed loop transfer function

[A_cl,B_cl,C_cl,D_cl,sys_cl]=closed_loop_collocated(Atot,Btot,Ctot,G,K_obs,F);
[mag_cl,phase_cl,freq_cl,frf_model_cl,ind_model_cl]=freq_data(sys_cl,1200);

sys_k = ss(Atot-Btot*G-K_obs*Ctot,K_obs,-G,0);      % COMPENSATOR system


Ts=1/8000;

sys_k_z=c2d(sys_k,Ts,'tustin');
[Phi,Gamma,H,J]=ssdata(sys_k_z);
```

```
%_____________________________________________
%

t=0:.0001:2;

[y_cl,t_cl,x_cl]=impulse(sys_cl,t);
V=-G*x_cl(:,sizeA+1:2*sizeA)';

P1=y_cl;

last_pressure(mult)=P1(length(P1));
last_voltage(mult)=V(length(V));

%_________________________________

Total_voltage=V.^2;
int_voltage=(trapz(Total_voltage)-(last_voltage(mult)...
*(t_cl(length(t_cl)))))/(t_cl(length(t_cl)));
rms_voltage(mult)=sqrt(int_voltage);

%_________________________________
% Pressure integrals
Total_pressure=(P1-last_pressure(mult)).^2;
int_pressure=(trapz(Total_pressure))/(t_cl(length(t_cl)));
rms_pressure(mult)= sqrt(int_pressure);

mult=mult+1;

end

l=length(rms_voltage);
m(1)=0;
m(counter+1)=l+m(counter);
data(m(counter)+1:m(counter)+l,:)=[r(1:l)' rms_voltage' rms_pressure'];

additional=additional+1;

eval(['save M' num2str(save_count) ' data -ascii']);

save_count = save_count + 1;

end
```

Appendix F

MATLAB Program to generate LQR and PPF controllers

```
clear all;
close all;

spkrtype=0;
impulse_mag=0.5e4;
varlength=1;

if spkrtype==0;
   R=3500;
end


if spkrtype==1;
   R=11;
end


%___________________________________________________________
% Physical parameters of the system

theta=0.216948;
area=.0214; % meters^2
mass_air= 0;  % kilograms
ms= 0.01838; % kilograms

if spkrtype==0;
   ks= 851.789;    % Newtons/ meter
end
if spkrtype==1;
   wn=1240.930098015615;
   ks=130000;
   ms=ks/wn^2;
end

flux= 6.77; % Flux(Tesla-N/A)
```

```
resistance= 6.6; % ohms
inductance= .93E-3; % Henries
r1=0.631165; % meters
r2=1.79322;
density=1.206;
P0=101.3E3;
gamma=1.4;
c=343;



%___________________________________________________________
% Define frequency vectors


f=0.01:0.1:1200;
w=2*pi*f;
k=w/c;



%___________________________________________________________
% Frequency domain transfer functions between pressure and voltage,
%and pressure and current


Za=impedance_calc(0,r1,r2,k,w,area,density);


%__________________________________________________________
% Generate a s-plane transfer function of the system impedance

if spkrtype==0;
zetanum=0.0005; % Define damping coefficient for numerator
zetaden=0.000005; % Define a damping coefficient for denominator
end

if spkrtype==1;
zetanum=0.0005; % Define damping coefficient for numerator
zetaden=0.00002; % Define a damping coefficient for denominator
end


sys=series(transfer_function_5mode(Za,zetanum,zetaden,f),tf(1,[1,0.0]));


%____________________________________________________________
% There exists a gain which must be accounted for.


frfini=reshape(freqresp(sys,f*2*pi),length(f),1);
index=0;
for count=1:1:30;
gain(count)=(abs(Za(count)))/(abs(frfini(count)));
```

```
end

gainave=sum(gain)/length(gain);


%___________________________________________________________
% Including this average gain, the system becomes

sys = gainave*sys;

%___________________________________________________________
% Use a modal canonical transformation to place system into state space form

sys_ss=canon(sys,'modal');

%___________________________________________________________
% Extract the frf information of the transfer function

[mag,phase,freq,frf_model,ind_model]=freq_data(sys,1200);

%___________________________________________________________
% Extract the system information from this canonical system

[mag_ss,phase_ss,freq_ss,frf_model_ss,ind_model_ss]=freq_data(sys_ss,1200);

%___________________________________________________________
%___________________________________________________________


[Atot,Btot,Ctot,Dtot,sys_tot]=
coupled_system(sys_ss,ks,ms,flux,resistance,inductance,area);
[mag_tot,phase_tot,freq_tot,frf_model_tot,ind_model_tot]=freq_data(sys_tot,500);

%%%%%%%%%%%%%%%%%%%%%%%%%%%%%%%%%%%%%%%%%%%%%%%%%%%%%%%%%%%%%%%%%%%%%%%%%%%%%%%%%

% With the system development from above, move into the development of LQR control

%%%%%%%%%%%%%%%%%%%%%%%%%%%%%%%%%%%%%%%%%%%%%%%%%%%%%%%%%%%%%%%%%%%%%%%%%%%%%%%%%

% Consider the system controllability

sizeA=length(Atot);
    A_Q_N=Atot;
A_Q_N(2:sizeA,:)=10^-4.1*A_Q_N(2:sizeA,:);
    Q=zeros(sizeA);
N=zeros(sizeA);
for count=linspace(1,sizeA,sizeA);
   Q(:,count)=A_Q_N^(count-1)*Btot;
    N(:,count)=(A_Q_N)^(count-1)*Ctot';
end
rank_Q = rank(Q);
rank_N = rank(N);

%_____________________________________________
```

```
%
% Now introduce the disturbance matrices E and F

F=zeros(sizeA,1);
for count= 5:2:sizeA;
   F(count)=1;
end

%_____________________________________________
%
% With the input disturbance matrix F, define a system to simulate
% the plant given a disturbance input through F.

sys_impulse=ss(Atot,F,Ctot,Dtot);

%_____________________________________________

% PART 7.

% Now consider the application of LQR control
       % Will weight according to the output matrix,
       % as well as the control effort


%_____________________________________________
%_____________________________________________
% Now define the weighting matrices Q and R


Q=Ctot'*Ctot;
Q=Q*10;


%_____________________________________________
%_____________________________________________


[G,S,cl_eig]=lqr(Atot,Btot,Q,R);


%_____________________________________________
% Define systems using lqr gains


sys_lqr=ss(Atot-Btot*G,Btot,Ctot,Dtot);

%_____________________________________________
% NOW MOVING ON TO OBSERVER DESIGN

% Define new pole locations, will make 5 times faster than CL poles

real_LQR=real(cl_eig);
imag_LQR=imag(cl_eig);
```

```
poles_obs=sort(5*real_LQR+imag_LQR*i);


% Determine observer gain matrix K and develop equivalent State rep.


L_p = place(Atot',Ctot',poles_obs)';


%______________________________________________
% Now develop the closed loop transfer function


[A_cl,B_cl,C_cl,D_cl,sys_cl]=closed_loop_collocated(Atot,Btot,Ctot,G,L_p,F);
[mag_cl,phase_cl,freq_cl,frf_model_cl,ind_model_cl]=freq_data(sys_cl,1200);

sys_comp = ss(Atot-Btot*G-L_p*Ctot,L_p,-G,0);      % COMPENSATOR system

%____________________________________________
%

t=0:.00008:0.2;

[y_cl,t_cl,x_cl]=impulse(sys_cl,t);



%%%%%%%%%%%%%%%%%%%%%%%%%%%%%%%%%%%%%%%%%%%%%%%%%%%%%%%%%%%%%%%%%%%%%%%%%
%%%%%%%%%%%%%%%%%%%%%%%%%%%%%%%%%%%%%%%%%%%%%%%%%%%%%%%%%%%%%%%%%%%%%%%%%

%_____________________________________________________
% Begin by discretizing the coupled state-space representation of the
% coupled system.


Ts=1/8000;

sys_plant_z=c2d(sys_tot,Ts,'zoh');
sys_impulse_z=c2d(sys_impulse,Ts,'zoh');
sys_comp_z=c2d(sys_comp,Ts,'tustin');

sys_ol=series(sys_impulse_z,sys_comp_z);

%%%%%%%%%%%%%%%%%%%%%%%%%%%%%%%%%%%%%%%%%%%%%%%%
%%%%%%%%%%%%%%%%%%%%%%%%%%%%%%%%%%%%%%%%%%%%%%%%

% Place compensator in canonical form


csys_comp_z=canon(sys_comp_z,'modal');

%%%%%%%%%%%%%%%%%%%%%%%%%%%%%%%%%%%%%%%%%%%%%%%%
%%%%%%%%%%%%%%%%%%%%%%%%%%%%%%%%%%%%%%%%%%%%%%%%
```

```
% Extract the state components of the compensator
[Phi,Gamma,H,J,ts]=ssdata(sys_comp_z);

% Look at the open loop system, plant and compensator
sys_z=series(sys_impulse_z,sys_comp_z);

% Look at the closed loop system in discrete form
sys_z_fb=feedback(sys_z,1,+1);

%_______________________________________________________
% Impulse of plant and closed loop systems

[y_ol,t_ol,x_ol]=impulse(sys_ol,varlength);
[y_comp,t_comp,x_comp]=impulse(sys_comp_z,varlength);
[y_fb,t_fb,x_fb]=impulse(sys_z_fb,varlength);
[y_plant,t_plant,x_plant]=impulse(sys_tot,0:0.001:varlength);
[y_impulse,t_impulse,x_impulse]=impulse(sys_impulse,0:Ts*2:varlength);

V_cont=-G*x_fb(:,length(Atot)+1:2*length(Atot))';

%_______________________________________________________
% Simulate the system through the simulink file LQR_SIMULATION_COMP.mdl

sim('LQR_simulation_comp');



%%%%%%%%%%%%%%%%%%%%%%%%%%%%%%%%%%%%%%%%%%%%%%%%%%%%%%%%%%%%%%
%%%%%%%%%%%%%%%%%%%%%%%%%%%%%%%%%%%%%%%%%%%%%%%%%%%%%%%%%%%%%%
%%%%%%%%%%%%%%%%%%%%%%%%%%%%%%%%%%%%%%%%%%%%%%%%%%%%%%%%%%%%%%



%_____________________________________________
%_____________________________________________
%
% Now consider a PPF filter design, targeting the first 4 modes

eigs=sort(abs(pole(sys_tot))/(2*pi));

if spkrtype==0;
   ppf_f=sqrt(2)*[eigs(1),  eigs(2),  eigs(4),  eigs(6),eigs(8)];
   ppf_d=10*[0.02,0.02,0.03,0.03,0.02];
end


if spkrtype==1;
   ppf_f=1*[eigs(1),  eigs(2),  eigs(4),  eigs(6), eigs(8)];
   ppf_d=.75*[0.02,0.02,0.02,0.02,0.02];
end

A1=[0 1; -(2*pi*ppf_f(1))^2  -4*pi*ppf_f(1)*ppf_d(1)];
A2=[0 1; -(2*pi*ppf_f(2))^2  -4*pi*ppf_f(2)*ppf_d(2)];
A3=[0 1; -(2*pi*ppf_f(3))^2  -4*pi*ppf_f(3)*ppf_d(3)];
```

```
A4=[0 1; -(2*pi*ppf_f(4))^2  -4*pi*ppf_f(4)*ppf_d(4)];
A5=[0 1; -(2*pi*ppf_f(5))^2  -4*pi*ppf_f(5)*ppf_d(5)];

B=[0; 1];
C=[1  0];
D=0;

ppf1=ss(A1,B,C,D); ppf2=ss(A2,B,C,D); ppf3=ss(A3,B,C,D);
ppf4=ss(A4,B,C,D); ppf5=ss(A5,B,C,D);



%______________________________________________________
%______________________________________________________
%
% Now the continuous form of the compensators are known
% move on to the discrete form for implementation

Ts=1/8000;

ppf1_z=c2d(ppf1,Ts); ppf2_z=c2d(ppf2,Ts); ppf3_z=c2d(ppf3,Ts);
ppf4_z=c2d(ppf4,Ts); ppf5_z=c2d(ppf5,Ts);


if spkrtype==0;
   g2=1000;
   g3=20000;
   g4=60000;
end

if spkrtype==1;
   g2=100;
g3=6000;
g4=40000;
end


sys_comp=parallel(parallel(g2*ppf2_z,g3*ppf3_z),g4*ppf4_z);

% In state-space form
[num_c,den_c]=tfdata(sys_comp,'v');
[Ac,Bc,Cc,Dc]=tf2ss(num_c,den_c);


% Now consider the discrete form of the plant.
sys_plant_z=c2d(sys_tot,Ts,'zoh');


% With a disturbance input, this becomes,
sys_dist_input_z=c2d(sys_dist_input,Ts,'zoh');
[Ap,Bp,Cp,Dp]=ssdata(sys_dist_input_z(1));


% Form the closed loop system (pressure-output, disturbance-input);
```

```
Acl=[Ap+Bp*Cp*Dc Bp*Cc
   Bc*Cp Ac];
Bcl=[F ; zeros(length(Bc),1)];
Ccl=[Cp ,zeros(1,length(Cc))];
Dcl=0;

sys_cl_D=ss(Acl,Bcl,Ccl,Dcl);


% Considering the openloop transfer function between actuator input
%and controller output

sys_ol_V=series(sys_dist_input_z(1),sys_comp);
[mag_ol_V,phase_ol_V,freq_ol_V,frf_model_ol_V,ind_model_ol_V]=freq_data(sys_ol_V,500);


% Considering the openloop transfer function between disturbance input
%and controller output

sys_ol_D=series(sys_dist_input_z(2),sys_comp);
[mag_ol_D,phase_ol_D,freq_ol_D,frf_model_ol_D,ind_model_ol_D]=freq_data(sys_ol_D,500);

% Consider the closed loop forms of these systems

sys_cl_V=feedback(sys_ol_V,1);
[mag_cl_V,phase_cl_V,freq_cl_V,frf_model_cl_V,ind_model_cl_V]=freq_data(sys_cl_V,500);
[mag_cl_D,phase_cl_D,freq_cl_D,frf_model_cl_D,ind_model_cl_D]=freq_data(sys_cl_D,500);


figure,bode(sys_comp)
figure,bode(sys_ol_V)

%%%%%%%%%%%%%%%%%%%%%%%%%%%%%%%%%%%%%%%%%%%%%%%%
%%%%%%%%%%%%%%%%%%%%%%%%%%%%%%%%%%%%%%%%%%%%%%%%

% Place compensator in canonical form



%%%%%%%%%%%%%%%%%%%%%%%%%%%%%%%%%%%%%%%%%%%%%%%%
%%%%%%%%%%%%%%%%%%%%%%%%%%%%%%%%%%%%%%%%%%%%%%%%


[y_plant,t_plant,x_plant]=impulse(sys_tot,0:0.001:varlength);
[y_impulse,t_impulse,x_impulse]=impulse(sys_dist_input,0:Ts*2:varlength);


sim('PPF_simulation_discrete');
```

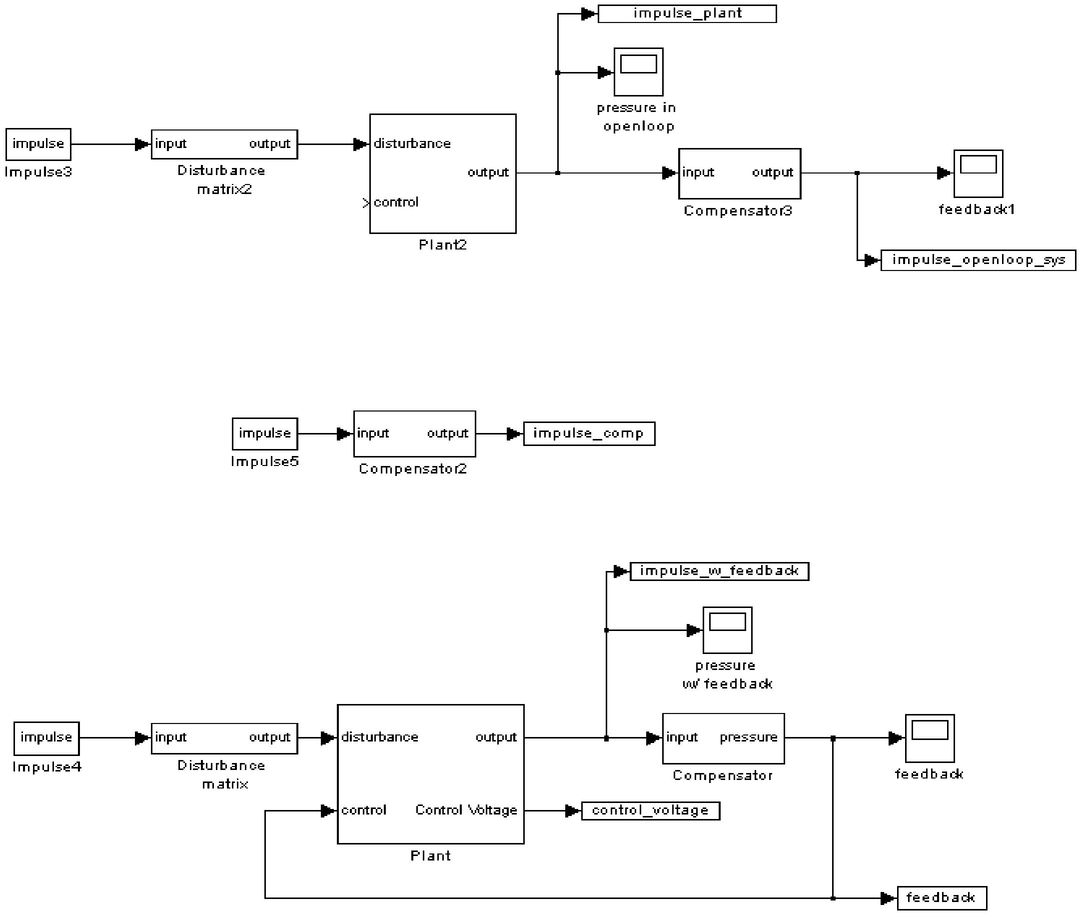

Figure F.1: Simulinkdiagram of the system using LQR compensation

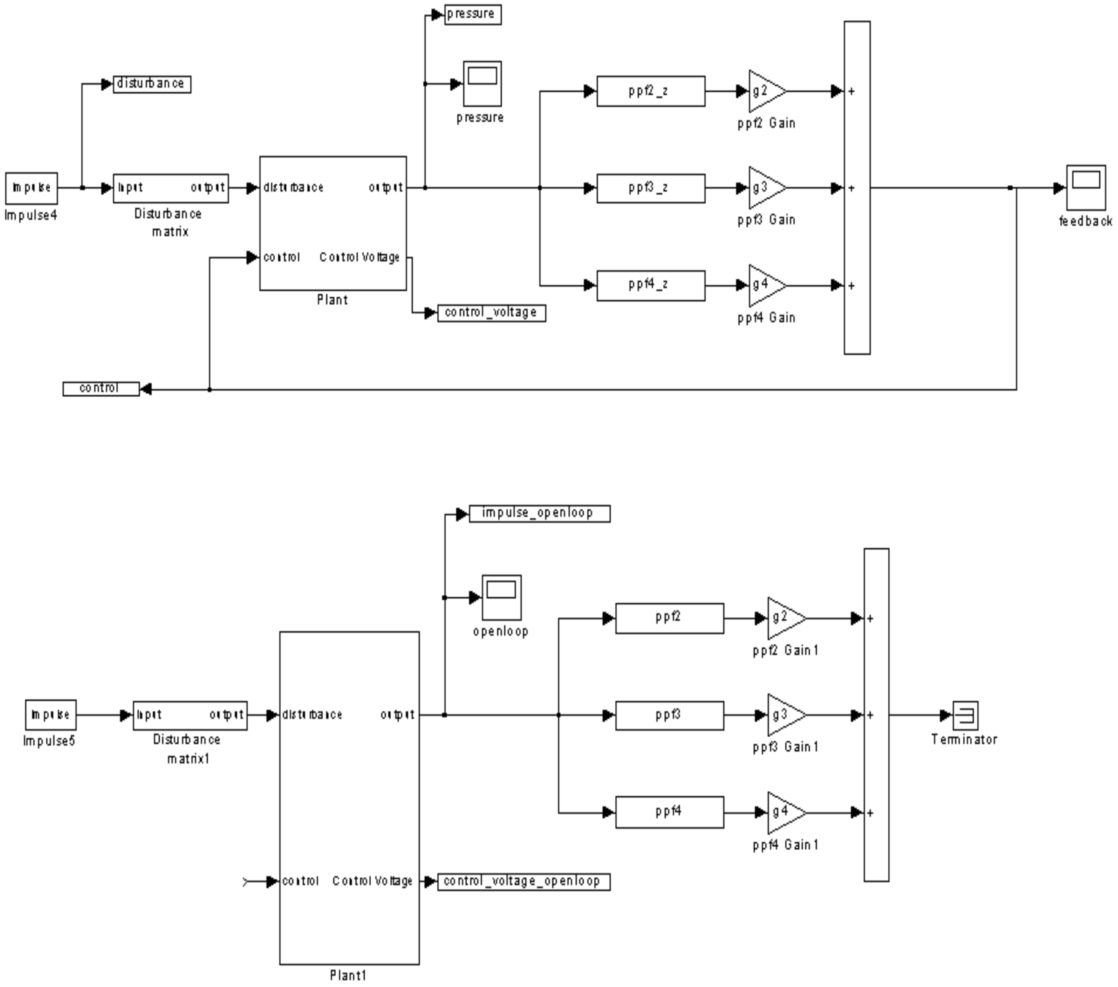

Figure F.2: Simulinkdiagram of the system using PPF compensation

FUNCTION FILES

```
function imp=impedance_calc(loc,r1,r2,k,w,area,density)

if loc==0;
   imp=((r1*(exp(2*i*k*r1).*(-i + k*r2) + exp(2*i*k*r2).*(i + k*r2))*density.*w)./...
    ((-(exp(2*i*k*r1).*(i + k*r1).*(-i + k*r2)) + exp(2*i*k*r2).*(-i + k*r1).*...
    (i + k*r2))*area));
end
if loc==0.25;
imp=(4*exp(i/4*k*(r1 - r2))*r1^2.*(exp(i/2*k*(3*r1 + r2)).*(-i + k*r2) +...
    exp(2*i*k*r2).*(i + k*r2))*density.*w)./((3*r1 + r2).*(-(exp(2*i*k*r1).*...
    (i + k*r1).*(-i + k*r2)) + exp(2*i*k*r2).*(-i + k*r1).*(i + k*r2))*area);
end
if loc==0.5;
   imp=(2*exp(i/2*k*(r1 - r2))*r1^2.*(exp(i*k*(r1 + r2)).*(-i + k*r2) +...
    exp(2*i*k*r2).*(i + k*r2))*density.*w)./((r1 + r2).*(-(exp(2*i*k*r1).*...
    (i + k*r1).*(-i + k*r2)) + exp(2*i*k*r2).*(-i + k*r1).*(i + k*r2))*area);
end
if loc==0.75;
   imp=(4*exp((3*i)/4*k*(r1 - r2))*r1^2.*(exp(i/2*k*(r1 + 3*r2)).*...
    (-i + k*r2) + exp(2*i*k*r2).*(i + k*r2))*density.*w)./((r1 + 3*r2).*...
    (-(exp(2*i*k*r1).*(i + k*r1).*(-i + k*r2)) + exp(2*i*k*r2).*(-i + k*r1).*...
    (i + k*r2))*area);
end
if loc==1.0;
   imp=(2*exp(i*k*(r1 + r2)).*k*r1^2*density.*w)./((-(exp(2*i*k*r1).*...
      (i + k*r1).*(-i + k*r2)) + exp(2*i*k*r2).*(-i + k*r1).*(i + k*r2))*area);
end


%___________________________________________________________
function sys=transfer_function(Za,zetanum,zetaden,f)

mag_Za=abs(Za);
phase_Za=180/pi*(atan2(imag(Za),real(Za)));

incrlow=round(length(f)/8);
incrhi=round(length(f)/9)-1;

for count=1:1:5;
   ind_l_Za=find(mag_Za((count-1)*incrlow+1:count*incrlow-1)==
min(mag_Za((count-1)*incrlow+1:count*incrlow-1)));
z(count)=f((count-1)*incrlow+1+ind_l_Za);
end

for count=1:1:6;
   ind_h_Za=find(mag_Za((count-1)*incrhi+1:count*incrhi-1)==
max(mag_Za((count-1)*incrhi+1:count*incrhi-1)));
p(count)=f((count-1)*incrhi+1+ind_h_Za);
end

z=z*(2*pi);
```

```
p=p*(2*pi);

for count=1:1:5;
    num_za(count,:)=[1/z(count)^2 2*zetanum/(z(count)) 1];
    den_za(count,:)=[1/p(count+1)^2 count*2*zetaden/(p(count)) 1];
end

num_z=conv(conv(conv(num_za(1,:),num_za(2,:)),conv(num_za(3,:),num_za(4,:)))
,num_za(5,:));
den_z=conv(conv(conv(den_za(1,:),den_za(2,:)),conv(den_za(3,:),den_za(4,:)))
,den_za(5,:));

sys=tf(num_z,den_z);

%____________________________________________________________
function [system_mag,system_phase,system_freq,system_frf_model,system_ind_model]=
freq_data(system,freqrange)

[numsys,densys]=tfdata(system,'v');
[system_mag,system_phase,system_ws]=bode(system);
system_mag=reshape(system_mag,length(system_ws),1);
system_phase=reshape(system_phase,length(system_ws),1);
system_freq=reshape(system_ws,length(system_ws),1)/(2*pi);
system_frf_model=reshape(freqresp(system,system_freq*2*pi),length(system_ws),1);
system_ind_model=find(system_freq<=freqrange);

%____________________________________________________________
function [A,B,C,D,totalsystem]=
coupled_system(system,ks,ms,flux,resistance,inductance,area)

% Define the speaker dynamics of the system
As=[0  1   0;
   -ks/ms  0  flux/ms;
   0  -flux/inductance  -resistance/inductance];
Bs1=[0 0 1/inductance]';
Bs2=[0 -area/ms 0]';
Cs=[0 1 0];
Ds=[0];

% Extract the state components of the system

[Aa,Ba,Ca,Da]=ssdata(system);

% Form the state matrices of the coupled system

A=[ As Bs2*Ca
   Ba*area*Cs Aa ];
B=[Bs1; zeros(length(Ba),1)];
C=[zeros(1,length(Cs)),Ca];
D=[0];

% Form the total system

totalsystem=-1/10000*ss(A,B,C,D);
```

Vita

Kevin Farinholt was born on March 16, 1976 to Joseph and Linda Farinholt of Charlottesville Virginia. He graduated from Albemarle High School in May 1994 and began his college education at Piedmont Virginia Community College in August of that year. Completing an Associates in Science in 1997, he transfered to Virginia Tech and began courses in the Summer of 1997. Completing a year of co-op experience with AlliedSignal, Kevin was accepted into the 5 year MS/BS program at Virginia Tech in the fall of 1999. Graduating Summa Cum Laude in Mechanical Engineering in May of 2000, Kevin began his Master's research under Dr. Donald Leo with the Center for Intelligent Material Systems and Structures (CIMSS) in the area of acoustic control of launch vehicle payload fairings.

Address: Center for Intelligent Material Systems and Structures
310 Durham Hall
Blacksburg, VA 24061

This thesis was typeset with LaTeX 2ε[1] by the author.

---

[1] LaTeX 2ε is an extension of LaTeX. LaTeX is a collection of macros for TeX. TeX is a trademark of the American Mathematical Society. The macros used in formatting this thesis were written by Greg Walker, Department of Mechanical Engineering, Virginia Tech.